



Ph. D.

HARRY JOSEPH TRODAHL

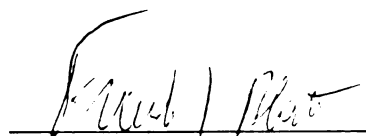
THE
NATIONAL ACADEMY
OF SCIENCES
OF THE UNITED STATES OF AMERICA
PUBLISHED BY THE NATIONAL ACADEMY PRESS
WASHINGTON, D. C. 20540



This is to certify that the
thesis entitled
QUANTUM OSCILLATIONS IN THE PELTIER
EFFECT IN ZINC

presented by
Harry Joseph Trodahl

has been accepted towards fulfillment
of the requirements for
Ph.D. degree in Physics


Major professor

Date May 14, 1968

ABSTRACT

QUANTUM OSCILLATIONS IN THE PELTIER EFFECT IN ZINC

by Harry Joseph Trodahl

Peltier measurements have been employed to study quantum oscillations in the thermoelectric power of zinc single crystals. The three lowest frequencies, due to the α , β and γ orbits, were observed at temperatures ranging from 1°K and 4.5°K and in fields to 22 kilogauss. The amplitudes found were between .01 and $1\ \mu\text{v/K}^{\circ}$.

An attempt has been made to correlate the results of these measurements with an expression derived by Horton. As his calculation is valid only for the case of a free electron sphere we have heuristically extended his results to include metals with complex Fermi surfaces. The theory and measurements agree only on the form of the temperature dependence; neither the absolute amplitude nor the field dependence is correctly predicted by the theory. It is suggested that the primary source of the disagreement may be found in the rather simplified scattering potential assumed by Horton.

QUANTUM OSCILLATIONS IN THE PELTIER
EFFECT IN ZINC

By

Harry Joseph Trodahl

A THESIS

Submitted to
Michigan State University
in partial fulfillment of the requirements
for the degree of

DOCTOR OF PHILOSOPHY

Department of Physics

1968

G51543
10/8/68

Acknowledgments

I would like to express my thanks to Dr. F. J. Blatt for his interest and guidance throughout this work and to Dr. P. A. Schroeder for many helpful discussions. I am very grateful to my wife, Judy, for her assistance in proofreading and typing the thesis.

The financial support of the National Science Foundation is gratefully acknowledged.

Table of Contents

	p.
I. Introduction	1
II. General Theory	5
III. Quantum Oscillations-general theory	10
IV. Quantum Oscillations in the Thermoelectric Power	
A. Introduction	17
B. Horton Theory	17
C. Extension to a Complicated Fermi Surface	21
V. Nonoscillatory Magnetothermoelectricity	32
VI. Experimental Approach	
A. Seebeck Measurements at Low Temperatures	33
B. Peltier Measurements, general	33
C. Thermal Contact Considerations	40
D. Double Junction Technique	42
VII. Experimental Apparatus	
A. Cryostat	46
B. Pumping System	48
C. Measuring Electronics	49
D. Magnetic Field Electronics	60
E. Temperature Control and Measurement	63
VIII. Operation, Data Reduction	
A. Introduction	64
B. Point by Point Methods	64
C. Continuous Detection	66
IX. Samples	
A. Zn 1	69
B. Zn 2	69
X. Results	
A. Zinc Fermi Surface	70

	p.
B. Data Interpretation	70
C. Zn 1	72
D. Zn 2	75
1. The α Oscillations	81
2. Monster Neck (β) Oscillations	81
3. Monster Arm (γ) Oscillations	87
XI. Conclusions	
A. Modified Horton Theory in Zinc	96
B. Auxiliary Data	97
C. The α Oscillations	102
D. The β and γ Oscillations	
1. Absolute Amplitude	103
2. Field Dependence, Apparent Dingle Factor	104
3. Temperature Dependence	107
E. General Conclusions	108
F. Nonoscillatory Seebeck Coefficient	108

Figures

	p.
1. Thermocouple circuits	2
2. Simple Peltier junction	4
3. Peltier junction between anisotropic metals	8
4. Landau levels in a free electron gas	11
5. Two dimensional one OPW Fermi surfaces	14
6. Curvature of a one OPW Fermi surface	26
7. $A_3(\lambda)$ vs. λ	31
8. Experimental Peltier junction	34
9. Thermal Contact diagrams	41
10. Double Peltier junction	43
11. Cryostat	47
12. Measuring electronics	50
13. Thermometer bridge	52
14. Bridge to cryostat leads	53
15. Circuit diagram of control electronics	54
16. Control circuit switch positions	55
17. Current control sections	56
18. Mode 1 control logic	58
19. Mode 2 control logic	59
21. Magnetic field electronics	61
22. Field sweep control	62
23. Typical recorder trace, mode 1	65
24. Typical recorder trace, mode 2	67
25. The zinc Fermi surface	71
26. β oscillations in Zn 1	73
27. $ \tilde{S}_\beta $ vs. T, Zn 1	74
28. Thermal damping of the β oscillations	76
29. $ \tilde{S}_\beta $ vs. H, Zn 1	77
30. \tilde{S} vs. θ , Zn 1	78
31. \tilde{S} vs. T, Zn 1	79

32. Field rotation, Zn 2	80
33. α oscillations, Zn 2	82
34. $ \mathcal{S}_\alpha $ vs. θ , Zn 2	83
35. $ \mathcal{S}_\alpha $ vs. T, Zn 2	84
36. f_β vs. θ , Zn 2	85
37. $ \mathcal{S}_\beta $ vs. θ , Zn 2	86
38. $ \mathcal{S}_\beta $ vs. H, Zn 2	88
39. $ \mathcal{S}_\beta $ vs. T, Zn 2	89
40. f_γ vs. θ , Zn 2	90
41. $ \mathcal{S}_\gamma $ vs. θ , Zn 2	91
42. Typical γ oscillations	92
43. $ \mathcal{S}_\gamma $ vs. H, Zn 2	93
44. $ \mathcal{S}_\gamma $ vs. T, Zn 2, 32° from $\langle 0001 \rangle$	94
45. $ \mathcal{S}_\gamma $ vs. T, Zn 2, 35° from $\langle 0001 \rangle$	95
46. \underline{a} vs. θ , Zn 2	100
47. f_δ vs. θ , Sn	114
48. $ \mathcal{S}_\delta $ vs. θ , Sn	115
49. $ \mathcal{S}_\delta $ vs. H, Sn	116
50. Seebeck coefficient of Pb	118
51. Seebeck coefficient of Ni	119
52. Pb vs. Ni in a magnetic field	120
53. Seebeck coefficient of Fe	121
54. Seebeck coefficient of W, low temperature	122
55. Seebeck coefficient of W, intermediate temperature	123
56. Thompson heat correction	127
57. Wheatstone bridge	132
58. Low temperature resistance of a carbon resistor	133
59. Magnetoresistance of Manganin	136
60. Sample alignment	139

Tables

	p.
1. Fermi surface curvature	102
2. Comparison of theoretical and experimental amplitudes	104
3. Apparent Dingle relaxation times	104
4. Revised amplitude estimates	105

Appendices

	p.
I. Sn Measurements	113
II. Measurements on Polycrystalline Materials	117
III. Thompson Heat Correction	126
IV. Thermometer Linearity	131
V. Manganin Resistance	135
VI. Kelvin-Onsager Relations in a Magnetic Field	137
VII. Effects of Sample Misalignment	138

I. Introduction

If one constructs a closed loop of two dissimilar conductors and heats one of the junctions a current is generated which can be detected with a compass. This was the first experiment, performed by J. Seebeck in 1821, in which the presence of thermoelectricity was indicated.¹ His experiments were followed in 1843 by Peltier's discovery that a current flowing through a biconductor junction could produce or absorb heat.² These effects are appropriately known as the Seebeck and Peltier effects.

The Seebeck effect is more easily treated if one considers the voltage causing the current to flow. This is measured by breaking the circuit as shown in figure 1a or b and measuring the potential difference across the break. It is possible to define a function $S_{AB}(T)$ for which

$$V = - \int_{T_1}^{T_2} S_{AB}(T) dT \quad (1)$$

$$S_{AB}(T) = - \partial V / \partial T. \quad (2)$$

Here V is the measured voltage when no current is flowing through the loop and T_1 and T_2 are the junction temperatures. Furthermore, it is possible to define a coefficient $S(T)$ for each conductor if the coefficient used in equations 1 and 2 is defined to be

$$S_{AB}(T) = S_A(T) - S_B(T) . \quad (3)$$

$S(T)$ is called the absolute Seebeck coefficient or the thermoelectric power of the material.

At the junction between two conductors the Peltier heat is proportional to the current flowing through the junction, and the Peltier coefficient Π is defined as the proportionality constant,

(2)

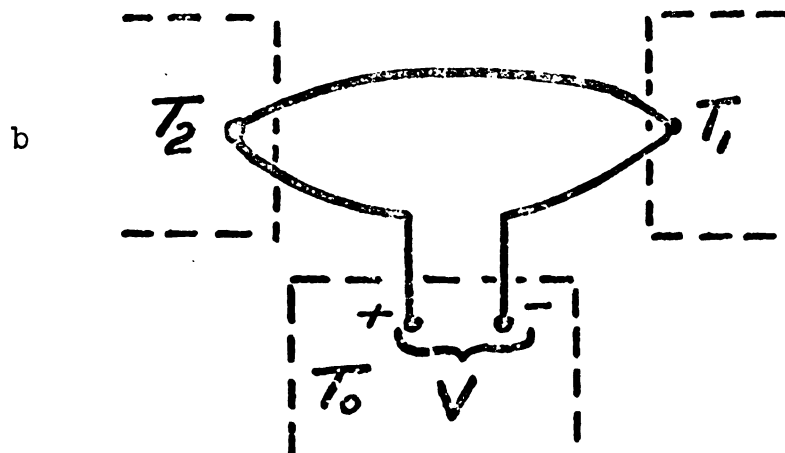
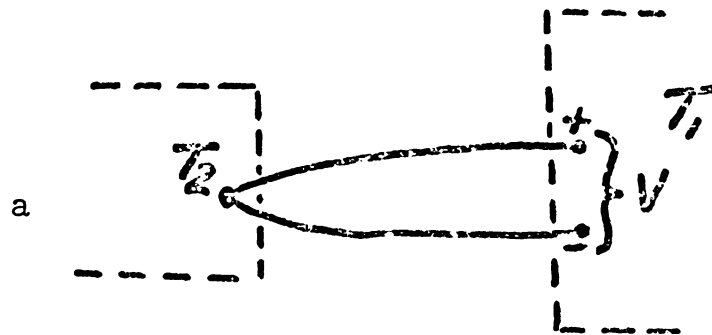


Figure 1. Thermocouple circuits

(3)

$$\dot{Q} = \Pi_{AB} I . \quad (4)$$

The sign convention used is that the Peltier coefficient is positive if the Peltier heat is evolved when the current is in the positive direction, from conductor A to conductor B in figure 2. As for the Seebeck coefficient, one may define a Peltier coefficient for an individual material. The coefficient in equation 4 is then given by

$$\Pi_{AB}(T) = \Pi_A(T) - \Pi_B(T) . \quad (5)$$

There is a third thermoelectric effect, the Thompson effect, first predicted by William Thompson in 1882. Along the length of a conductor which is both supporting a temperature gradient dT/dx and carrying an electrical current I a reversible heat is evolved per unit length given by

$$d\dot{Q}/dx = \mu(T)I(dT/dx) . \quad (6)$$

μ is the Thompson coefficient of the metal. It is interesting to note that this is the only thermoelectric effect which can be observed in a single conductor.

That the three thermoelectric effects are closely related has been known for a long time and the derivation of these relations has been one of the primary tests applied to the various treatments of non-equilibrium statistical mechanics.^{3,4} Called the Kelvin-Thompson relations after William Thompson (Lord Kelvin) who was the first to suggest them, these relations are

$$\Pi = TS \quad (7)$$

$$\mu = T(\partial S/\partial T) \quad (8)$$

in which T is the absolute temperature. The most elegant derivation of these equations is based on the Onsager reciprocal relations which demonstrate that the Kelvin relations are a direct consequence of microscopic reversibility.⁴⁻⁷

(4)

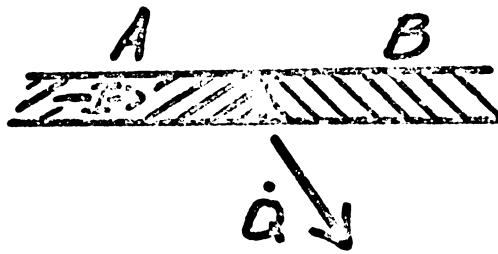


Figure 2. Simple Peltier junction

II. General theory

The results we can obtain from transport effect calculations are equations expressing currents as functions of appropriate driving forces. In a conductor we are concerned with both electrical and thermal currents.

$$\vec{J} = L_{EE}\vec{\nabla}\varphi + L_{ET}\vec{\nabla}T \quad (9)$$

$$\vec{U} = L_{TE}\vec{\nabla}\varphi + L_{TT}\vec{\nabla}T \quad (10)$$

\vec{J} = electrical current density

\vec{U} = thermal current density

T = temperature field

$\varphi = \mu - eV$ = electrochemical potential

μ = chemical potential

V = electrical potential

The quantities L_{ij} in general are nondiagonal tensors in an anisotropic material. The use of $\vec{\nabla}\varphi$ rather than $-e\vec{\nabla}V$ as a driving force permits us to apply the Onsager reciprocal relations,^{4,5}

$$L_{TE} = TL_{ET}. \quad (11)$$

However, due to the temperature dependent term in the electrochemical potential, the identification of the various measurable quantities is difficult. The only easy one to identify is the electrical resistance, measured under the condition that $\nabla T = 0$,

$$\rho = L_{EE}(-1/e). \quad (12)$$

The Seebeck and Peltier tensors are simply defined by

$$S = \rho \cdot L_{ET} \quad (13)$$

$$\Pi = L_{TE} \cdot \rho \quad (14)$$

The combination of equations 11, 13 and 14 results in the first Kelvin relation,

$$\Pi = TS \quad . \quad (15)$$

It remains to be shown that, at least in isotropic materials, equations 13 and 14 lead to the quantities defined in the introduction. Because of the terms $L_{EE}\vec{\nabla}\mu$ and $L_{TE}\vec{\nabla}\mu$ in equations 9 and 10 this is not a trivial problem, but the proper identification can be made.⁴ In anisotropic materials a measurement of the "Seebeck coefficient" involves a rather complicated combination of the elements of the Seebeck tensor as well as the elements of most of the other tensors, L_{ij} . However, we are here concerned only with the Peltier effect, i.e. the reversible heat produced at a junction between two conductors.

We extract from the paper by Domenicali⁴ the following four equations which represent the total of all heat production per unit volume in a conducting region.

$$\text{Joule} \quad \dot{q}_J = \sum_{i,j} \rho_{ij} J_i J_j \quad (16)$$

$$\text{Peltier} \quad \dot{q}_P = \sum_{i,j} (\partial \Pi_{ij} / \partial x_i) J_j \quad (17)$$

$$\text{Thompson} \quad \dot{q}_T = \sum_{i,j} \mu_{ij} J_j \partial T / \partial x_i \quad (18)$$

$$\text{Bridgeman} \quad \dot{q}_B = \sum_{i,j} \Pi_{ij} \partial J_j / \partial x_i \quad (19)$$

The Thompson tensor, μ , is given by

$$\mu = T \partial (\Pi/T) / \partial T \quad . \quad (20)$$

In Peltier measurements we are concerned only with reversible heat production, i.e., the heat production that is reversed by a reversal of the current direction, so that we may neglect the Joule heat term. We shall also neglect the Thompson heat term by requiring that temperature grad-

(7)

ients be small; more will be said about this later. Only the Peltier and Bridgeman terms remain and it is quite simple to show that

$$\dot{q}_B + \dot{q}_P = \vec{\nabla} \cdot (\Pi \vec{J}) \quad (21)$$

The total reversible heat production from these two terms inside a volume, V , bounded by the surface, s , is given by

$$\dot{Q}_{P+B} = \int_V \vec{\nabla} \cdot (\Pi \vec{J}) d\tau = \int_s (\Pi \vec{J}) \cdot \hat{n} ds, \quad (22)$$

by the divergence theorem.

The experimental arrangement is reasonably well approximated by figure 3. The junction between conductors A and B is in general a complex structure consisting of solder, crystallites of A and B, and impurities. We would like to calculate the reversible heat in the region of the junction, inside the dotted surface in figure 3. If we assume that this surface crosses the conductors sufficiently far from the junction that the currents are only along the lengths of the samples, equation 22 results in

$$\dot{Q}_{P+B} = (\hat{l}_A \cdot \Pi_A \cdot \hat{l}_A - \hat{l}_B \cdot \Pi_B \cdot \hat{l}_B) I \quad (23)$$

Thus it is the difference in the appropriate diagonal terms which is measured.

Perhaps the most common method used in transport calculations is through the Boltzmann equation, which can be solved to obtain the electron distribution function $f(k)$. One may then apply the equations

$$\vec{J} = e \int \vec{v}(k) f(k) d^3k \quad (26)$$

$$\vec{U} = \int \epsilon(k) \vec{v}(k) f(k) d^3k \quad (27)$$

and identify the tensors L_{ij} by comparing equations 26 and 27 with 9 and 10. In equations 26 and 27

(8)

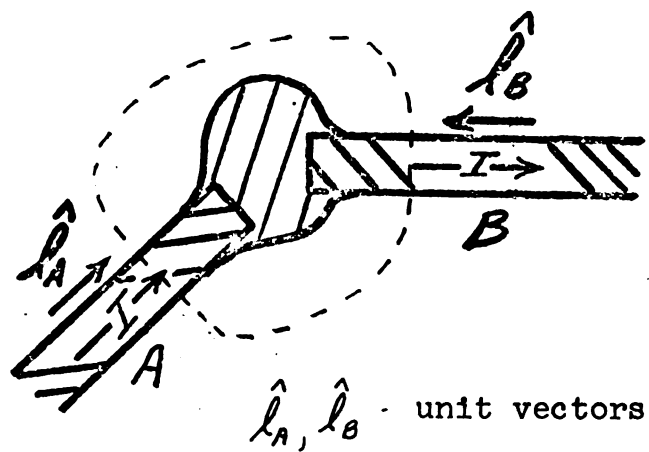


Figure 3 . Peltier junction between anisotropic metals

(9)

\vec{k} =wave vector

$\vec{v}(\vec{k})$ =velocity= $\vec{\nabla}_k \epsilon(\vec{k})$

$\epsilon(\vec{k})$ =electron energy

The combination of the Boltzmann equation with an assumption that there exists a unique relaxation time $\tau(\vec{k})$ at each point in momentum space leads to the familiar logarithmic derivative formula for the thermoelectric power.⁸

$$S = (\pi^2/3)(k^2T/e) \left\{ \partial [\log \sigma(\epsilon)] / \partial \epsilon \right\}_{\epsilon=\epsilon_F}, \quad (28)$$

in which $\sigma(\epsilon)$ is the electrical conductivity as a function of energy ϵ , T the absolute temperature and k the Boltzmann constant.

III. Quantum Oscillations - general theory*

The state of a free noninteracting electron gas contained in a three dimensional square well can be described by a sphere in single particle momentum (k) space the interior of which has an electron in every state while the exterior is empty. The boundary between the filled and empty regions, called the Fermi Surface, is not infinitely sharp; there is a region that is a few (kT) of energy thick in which the available electron states are only partly filled or empty.

In the absence of a magnetic field these states are distributed throughout k space with a constant density. The application^{of} a field redistributes them, with the same average density, onto the surfaces of cylinders aligned parallel to the magnetic field (see figure 4). It should be noted that an electron in an energy eigenstate does not remain stationary on one of these cylinders. It will orbit in a circle about the circumference with a frequency given by

$$\omega_c = eH/mc \quad . \quad (29)$$

The radii of these cylinders increases with magnetic field and as the outer one passes through the Fermi surface the electrons in those states fall into lower levels. This process repeats as each Landau cylinder passes through the Fermi surface, giving rise to an oscillatory magnetic field dependence of the internal energy and the density of states at the Fermi level. Similar oscillatory dependence could

* The material in this entire section is covered more completely in many solid state physics texts, for example see Kittel¹⁰. See also Pippard.¹¹

(11)

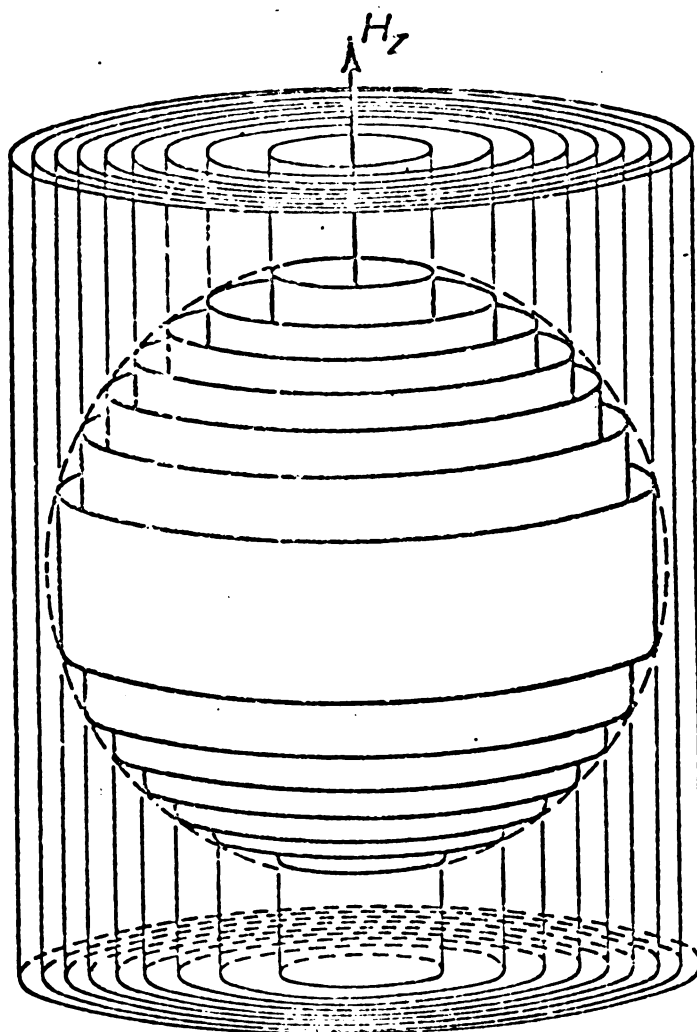


Figure 4. (after Rosenberg⁹) Landau levels in a free electron gas.

in principle be found in any electron related measurement and has been observed in the magnetization (de Haas-van Alphen), the electronic free energy (magnetothermal oscillations), the resistivity (de Haas-Shubnikov) and in an impressive list of more exotic effects including most of the transport coefficients.

The exact solution of the problem of a free electron gas in a magnetic field is not difficult. One finds that the oscillations are periodic in the inverse of the magnetic field with a period of

$$\Delta(1/H) = eh/\epsilon_f mc \quad (30)$$

where ϵ_f is the electron energy at the Fermi level, m and e the electronic mass and charge respectively.

Electronic states in real metals are affected to varying degrees by the periodic potential of the crystal lattice. The free electron states of energy ϵ and momentum k are mixed with states of (nearly) the same energy and with momentum differing by one reciprocal lattice vector G , defined by

$$\vec{G} = n_1 \vec{b}_1 + n_2 \vec{b}_2 + n_3 \vec{b}_3 \quad (31)$$

$n_i = \text{integers}$

$\vec{b}_1 = \vec{a}_2 \times \vec{a}_3 / (2\pi(\vec{a}_2 \times \vec{a}_3) \cdot \vec{a}_1)$ and cyclic permutations

$\vec{a}_i = \text{the basis vectors for the periodic lattice.}$

In the free electron approximation the energy is proportional to \vec{k}^2 so that mixing can occur only between states for which

$$\vec{k}^2 \approx (\vec{k} + \vec{G})^2. \quad (32)$$

The energy of states near the plane given by equation 32 is shifted in such a way that an energy gap appears between adjacent states on opposite sides of the plane. More impor-

tant here is the fact that an electron executing an orbit in the presence of a magnetic field will be reflected from \vec{k} to $\vec{k} + \vec{G}$ upon reaching the Bragg plane (given by equation 32). This can give rise to several orbits which may differ significantly from the free electron orbit; several possibilities in a two dimensional lattice are shown in figure 5. Obviously if the various sections of \vec{k} space defined by the Bragg planes are moved by the appropriate reciprocal lattice vectors \vec{G} , $\vec{k} + \vec{G}$ is adjacent to \vec{k} and a diagram representing the orbit in \vec{k} space appears.

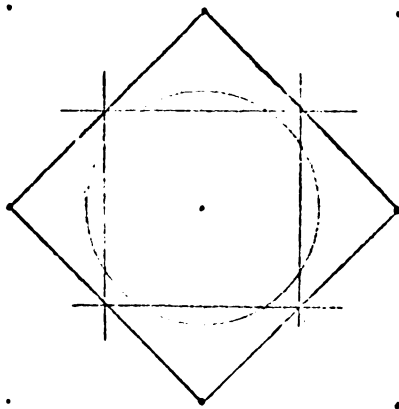
This method of obtaining the perturbed Fermi surface is commonly called the one O. P. W. (orthogonalized plane wave) scheme. The logical extension would be the use of some form of perturbation theory to calculate the energy shifts near the zone boundary, which approach is the basis of orthogonalized plane wave calculations.¹² For sufficiently small perturbations the effect of such a calculation is a simple rounding of the sharp edges of the Fermi surface.

In a magnetic field the orbits of electrons in \vec{k} space are altered by the Bragg reflections; they are no longer circular. However, the orbits are quantized and quantum oscillations, periodic in the inverse of the magnetic field strength, do occur with a period given by¹³

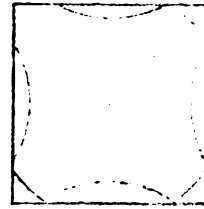
$$\Delta(1/H) = 2e/\hbar c A_0 . \quad (33)$$

In this expression A_0 is the extremal cross sectional area of the Fermi surface in the plane perpendicular to the magnetic field. The periods given by equations 30 and 33 are equivalent only for the case of a free electron gas.

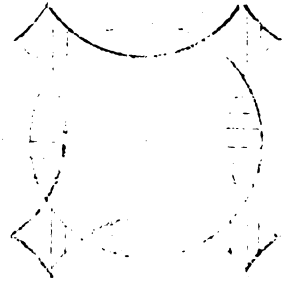
Quantum oscillation amplitudes are affected by the detailed form of the dispersion relation $\epsilon(\vec{k})$ near the orbits involved as well as thermal and collision broadening of the Landau levels. Brailsford¹⁴ gives the following expression for the oscillatory term in the free energy.



a



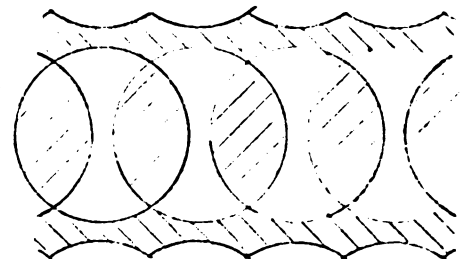
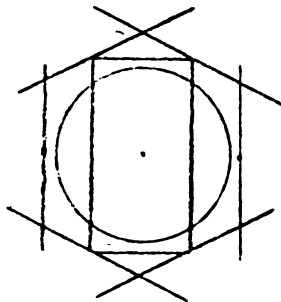
b



c

Two dimensional one O.P.W. Fermi surfaces for

- a) square lattice, extended zone scheme
- b) square lattice, reduced zone scheme
- c) square lattice, repeated zone scheme



- d) rectangular lattice, extended zone scheme
- e) repeated zone scheme; note the open orbits

Figure 5

(15)

$$F_{osc} = \frac{2kT(eH/2\pi\hbar c)^{3/2}}{\sqrt{(\partial^2 A / \partial k_z^2)_{k_0}}} \frac{\cos[(v\hbar c/eH)A_0 - 2\pi v\gamma - \pi/4]}{v^{3/2} \sinh(2\pi^2 v kT / \hbar \omega_c)} \quad \times \quad \exp\left(\frac{-\pi v}{\omega_c \tau_0}\right) \quad (34)$$

$H = H_z$ = magnetic field strength

k_z = quantum momentum along the magnetic field

$A = A(k_z)$ = cross sectional area of the Fermi surface in the plane perpendicular to H

$k_0 = k_z$ at the point at which $(\partial A / \partial k_z) = 0$

ω_c = cyclotron frequency = eH/m^*c

m^* = cyclotron effective mass = $(\hbar^2/2\pi)[\partial A / \partial \epsilon]_{k_z = \text{const} = k_0}$

τ_0 = oscillation relaxation time

γ = phase factor depending upon the electron dispersion law

The shift of the Landau energies due to impurity scattering has been omitted from equation 34, although Brailsford includes it. The collision broadening factor $\exp(-\pi v / \omega_c \tau_0)$ was first derived by Dingle¹⁵ for a free electron gas. For uncharged impurity scattering (δ function scattering centers) the relaxation time appearing here is just that which appears in the resistivity formula

$$\tau_0 = \tau_R \quad . \quad (35)$$

(16)

If a sufficiently large magnetic field is applied to a metal an electron may simply ignore a Bragg reflection plane and continue along the free electron Fermi sphere. This requires a discontinuous jump in \hat{k} at the plane, but of course the energy remains the same. The probability of such a process occurring is¹⁶

$$p = e^{-H_0/H} \quad (36)$$

$$H_0 \approx mc^2 \epsilon_g^2 / \hbar e \epsilon_f \quad (37)$$

ϵ_g = the energy gap between adjacent points on
opposite sides of the Bragg plane

ϵ_f = free electron Fermi energy

m = free electron mass

Magnetic breakdown, as this is called, can obviously give rise to an incredible number of new orbits.

IV. Quantum Oscillations in the Thermoelectric Power

A. Introduction

Theoretical expressions for equilibrium properties such as the magnetization or entropy of a free electron gas are relatively easily obtained from the expression for the free energy (equation 34) through the application of appropriate thermodynamic derivatives. This is impossible for the non-equilibrium transport phenomena. Another difficulty is encountered if one attempts to use the Boltzmann equation to calculate the transport tensors; the transverse diagonal terms of the velocity matrix are zero in the Landau representation.

There have been a number of attempts to calculate the oscillatory terms in the transport effects¹⁷⁻²³ using either the density matrix formalism or a modified form of the Boltzmann equation. These calculations have been made under a variety of assumptions about scattering mechanisms and dispersion laws, though none are directly applicable to the thermoelectric power oscillations in a complex metal. The only results presented in a form which can be easily extended are those obtained by Horton.²³

B. The Horton Theory

The approach used by Horton is to solve the quantum mechanical equation of motion for the density matrix ρ

$$\dot{\rho} = -\frac{1}{\hbar} [\mathcal{H}, \rho] \quad (38)$$

in which \mathcal{H} is the system hamiltonian and $[\]$ indicates the commutator. Neglecting electron-electron interactions he writes the hamiltonian \mathcal{H} as the sum of single particle hamiltonians, which in turn are written as the sum of a perturbed

(18)

and an unperturbed term. The former contains only the electron scattering terms while the latter contains all terms involving the magnetic and electric fields and can be used to obtain eigenfunctions and energy eigenvalues in the free electron approximation. Using these as the basis, Horton calculates the matrix elements of the scattering hamiltonian assuming a sparse and random distribution of delta function scattering centers. The entire hamiltonian matrix is then used in equation 38 along with an assumed initial density matrix and the resulting equation solved for time infinity. The expectation values of the electrical and thermal current densities are then obtained from the equation

$$\langle Q \rangle = \text{Tr}(Q \rho). \quad (39)$$

There are a number of further ingredients in the calculation. Fermi-Dirac statistics are used, the energy shifts and line broadening due to collisions are neglected, and it is assumed that an electron is allowed many orbits between collisions, i. e.,

$$\omega_c \tau \gg 1. \quad (40)$$

The calculation is made only for a free electron gas.

The results of this calculation are presented in terms of the elements L_{ij} of a 6 x 6 tensor which can be related to the tensors of equations 9 and 10 as follows;

$$L = \begin{pmatrix} eL_{EE} & TL_{ET} \\ eL_{TE} & TL_{TT} \end{pmatrix}. \quad (41)$$

The magnetic field is restricted to the z direction and with the help of symmetry arguments and the Onsager relations the thirty-six elements are reduced to nine.

(19)

$$L = \begin{pmatrix} L_{22}(H) & L_{12}(H) & 0 & L_{25}(H) & L_{15}(H) & 0 \\ -L_{12}(H) & L_{22}(H) & 0 & -L_{15}(H) & L_{25}(H) & 0 \\ 0 & 0 & L_{33}(H) & 0 & 0 & L_{36}(H) \\ L_{25}(H) & -L_{15}(H) & 0 & L_{55}(H) & L_{45}(H) & 0 \\ L_{15}(H) & L_{25}(H) & 0 & -L_{45}(H) & L_{55}(H) & 0 \\ 0 & 0 & L_{36}(H) & 0 & 0 & L_{66}(H) \end{pmatrix} \quad (42)$$

The only elements needed here are L_{22} , L_{12} , L_{25} , and L_{15} .

$$L_{12} = \frac{n e^2}{H} \left\{ 1 - \frac{\Gamma^2}{\Gamma^2 + \omega_c^2} \left[1 + \frac{7\sqrt{2}}{8} \sqrt{\frac{\hbar\omega_c}{\epsilon_f}} \sum_{\nu} \left(\frac{-1}{\sqrt{\nu}} \right)^{\nu} A_2(\lambda) \cos b \right. \right. \\ \left. \left. - \frac{7\sqrt{2}}{2} \frac{kT}{\epsilon_f} \sqrt{\frac{\hbar\omega_c}{\epsilon_f}} \sum_{\nu} \left(\frac{-1}{\sqrt{\nu}} \right)^{\nu} A_3(\lambda) \sin b \right] \right\} \quad (43)$$

$$L_{15} = - \frac{5\pi^2 e (kT)^2 n \Gamma^2}{6 H \epsilon_f (\Gamma^2 + \omega_c^2)} \left[1 - \frac{21\sqrt{2}}{10\pi^2} \sqrt{\frac{\hbar\omega_c}{kT}} \sqrt{\epsilon_f} \sum_{\nu} \left(\frac{-1}{\sqrt{\nu}} \right)^{\nu} A_3(\lambda) \sin b \right. \\ \left. + \frac{42\sqrt{2}}{5\pi^2} \sqrt{\frac{\hbar\omega_c}{\epsilon_f}} \sum_{\nu} \left(\frac{-1}{\sqrt{\nu}} \right)^{\nu} A_4(\lambda) \cos b \right] \quad (44)$$

$$L_{22} = \frac{n e^2}{m} \frac{\Gamma}{\Gamma^2 + \omega_c^2} \left[1 + \frac{5\sqrt{2}}{8} \sqrt{\frac{\hbar\omega_c}{\epsilon_f}} \sum_{\nu} \left(\frac{-1}{\sqrt{\nu}} \right)^{\nu} A_2(\lambda) \cos b \right. \\ \left. - \frac{15\sqrt{2}}{8} \frac{kT}{\epsilon_f} \sqrt{\frac{\hbar\omega_c}{\epsilon_f}} \sum_{\nu} \left(\frac{-1}{\sqrt{\nu}} \right)^{\nu} A_3(\lambda) \sin b \right] \quad (45)$$

$$L_{25} = \frac{2\pi^2}{3} \frac{n e}{m} \frac{(kT)^2}{\epsilon_f} \frac{\Gamma}{(\Gamma^2 + \omega_c^2)} \left[1 - \frac{15\sqrt{2}}{8\pi^2} \sqrt{\frac{\hbar\omega_c}{kT}} \sqrt{\epsilon_f} \sum_{\nu} \left(\frac{-1}{\sqrt{\nu}} \right)^{\nu} A_4(\lambda) \sin b \right. \\ \left. + \frac{45\sqrt{2}}{8\pi^2} \sqrt{\frac{\hbar\omega_c}{\epsilon_f}} \sum_{\nu} \left(\frac{-1}{\sqrt{\nu}} \right)^{\nu} A_4(\lambda) \cos b \right] \quad (46)$$

(20)

n = number of carriers in the (spherical) band

$$\lambda = v \left(\frac{2\pi^2 kT}{\hbar \omega_c} \right) \quad (47)$$

$$b = v \left(\frac{2\pi \epsilon_f}{\hbar \omega_c} \right) - \frac{\pi}{4} \quad (48)$$

$$A_2(x) = 2x \operatorname{csch} x \quad (49)$$

$$A_3(x) = -\pi \operatorname{csch}(x) [1 - x \operatorname{ctnh} x] \quad (50)$$

$$A_4(x) = \frac{\pi^2}{2} \operatorname{csch}(x) [2 \operatorname{ctnh} x - 2x \operatorname{ctnh}^2 x + x] \quad (51)$$

$$\Gamma = \frac{1}{\tau} = \text{scattering probability per unit time} \quad (52)$$

Since the calculations are restricted to a free electron gas the results are not suitable for comparison to experimental results. To illustrate this one may look at the resistivity tensor L_{EE}^{-1}/e . Neglecting the relatively small oscillatory terms one obtains the classical result

$$\rho = \begin{pmatrix} \rho_0 & R_H H & 0 \\ -R_H H & \rho_0 & 0 \\ 0 & 0 & \rho_0 \end{pmatrix} \quad (53)$$

$$\rho_0 = \frac{m\Gamma}{e^2 n} = \frac{m}{e^2 n \tau} \quad (54)$$

$$R_H = \frac{1}{nec} \quad . \quad (55)$$

The transverse resistance (ρ_{11} or ρ_{22}) is independent of

field in this model, dramatically untrue in real metals. We cannot expect meaningful results by simply applying equations 13 or 14 to equations 43 through 52.

However, it is instructive to look at the zero field limits of the transport coefficients and compare them with Boltzmann equation calculations for free electrons. This limit for the resistivity (equation 55) is quite familiar. In this limit equation 13 results in

$$S = \frac{\pi^2 k^2 T}{3e\epsilon_f} \quad (56)$$

which is a standard result for impurity scattering in a free electron gas.

C. Extension to a Complicated Fermi Surface

In the absence of a rigorous treatment of oscillatory transport phenomena in complex metals an attempt has been made to extend Horton's results. Although the methods used in this extension are by no means rigorous they do appear reasonable. By equations 13 and A-26,

$$S_{11} = \rho_{11}(L_{ET})_{11} + \rho_{12}(L_{ET})_{21} + \rho_{13}(L_{ET})_{31} \quad (57)$$

$$\Pi_{11}(H) = TS_{11}(-H) . \quad (58)$$

The coefficients $(L_{ET})_{11}$ and $(L_{ET})_{21}$ are to be identified with L_{25}/T and L_{15}/T from equations 46 and 44. In doing so we find that for a free electron gas the former is larger than the latter by a factor of order $\omega_c \tau$ for a free electron gas and that the relative magnitudes of the oscillatory terms are almost the same. If ρ_{11} and ρ_{21} were equal, then, the oscillatory contribution to S_{11} from the second term would be much smaller than that from the first. Al-

(22)

though for a free electron gas $\rho_{12} \sim \omega_c \tau \rho_{11}$, giving almost equal contribution from the two terms, we may find a more favorable situation in real metals. This must of course be justified in some way for any particular case (see section IX). For the present, however, the last two terms will be neglected.

If we restrict our attention to the oscillatory terms in S_{11} , we may write

$$\mathfrak{S}_{11} = \rho_{11} \tilde{L}_{25} / T \quad (59)$$

in which the oscillatory terms in ρ_{11} are to be neglected, a very good approximation in most cases, although again in need of justification under any given conditions. We shall regard ρ_{11} as an experimentally determined function of magnetic field while an expression for \tilde{L}_{25} will be obtained from an extension of equation 46.

In a real metal the electronic states from which a given set of oscillations arise are those near the periphery of an extremal cross section of the Fermi surface. With these orbits is associated a cyclotron effective mass m^* and a de Haas-van Alphen frequency f given by the inverse of equation 33. Here we shall assume that these are the important parameters, and shall rewrite equation 46 in terms of these. In so doing we have treated the small section of the Fermi surface as a "free quasi-electron" sphere which is uniquely determined by m^* and f .

The cosine term in equation 46 can be neglected to order kT/ϵ_f , an excellent approximation in metals. In the high field limit ($\omega_c \tau \gg 1$) the remaining oscillatory term is

$$\tau_{25} = \frac{5\sqrt{2}}{4} \frac{kT\epsilon}{m} \frac{n}{\tau \omega_c^2} \sqrt{\frac{\hbar \omega_c}{\epsilon_f}} \sum_v \frac{(-1)^v}{\sqrt{v}} A_3(\lambda) \sin b. \quad (60)$$

In order to alter this as suggested in the preceeding paragraph we require the following substitutions;

(23)

$$m \rightarrow m^* \quad (61)$$

$$n \rightarrow \frac{1}{6\pi^2} \left(\frac{2m^*}{h^2} \epsilon_f \right)^{3/2} \quad (62)$$

$$\omega_c \rightarrow eH/m^*c \quad (63)$$

$$\epsilon_f \rightarrow \frac{\hbar\omega_c f}{H} \quad (64)$$

Upon performing these,

$$\mathcal{L}_{25} = \frac{5}{6\pi^2} \left(\frac{ce}{h^3} \right)^{1/2} \frac{kTm^*f}{\tau H^{3/2}} \sum_{\nu} \frac{(-1)^{\nu}}{\sqrt{\nu}} A_3(\lambda) \sin b \quad (65)$$

in which b is now defined by

$$b = (2\pi f \nu / H) - \pi/4 \quad (66)$$

In fact, the oscillations do not come from a spherical surface, and an amplitude correction is required. We might expect that the electrical current caused by a temperature gradient is proportional to the number of effective carriers involved. This is equivalent to assuming that the tensor elements L_{ij} from different bands or parts of bands simply add to produce the resultant L_{ij} . Applying this idea to the oscillatory portions only suggests that the oscillation amplitude should be proportional to that range of k_z values, dk_z , for which the cross sectional area of the Fermi surface is within some small limit, $(\Delta A)_0$, of the extremal area. We therefore expand ΔA in a Taylors series,

(24)

$$(\Delta A_f)_o = \left(\frac{\partial A}{\partial k_z}\right)_{k_o} dk_z + \frac{1}{2} \left(\frac{\partial^2 A}{\partial k_z^2}\right)_{k_o} dk_z^2 + \dots \quad (67)$$

The first term is zero at an extremum.

$$dk_z \cong \left[2(\Delta A)_o / \left(\frac{\partial^2 A}{\partial k_z^2}\right)_{k_o} \right]^{1/2} \quad (68)$$

This is to be compared with the same parameter for the sphere used to derive equation 65, which must now be multiplied by

$$\left[\frac{(\partial^2 A / \partial k_z^2)_{f_{qefs}}}{(\partial^2 A / \partial k_z^2)_{k_o}} \right]^{1/2}$$

in which f_{qefs} = free quasi electron Fermi sphere, for which the appropriate derivative is easily shown to be given by 2π .

An estimate of the value of the area derivative can be obtained under the proper simplifying assumptions. The most reliable method utilizes de Haas van Alphen frequency data as a function of field angle. For a perfectly cylindrical Fermi surface, the frequency as a function of angle θ measured from the cylinder axis would be given by

$$f_c(\theta) = f_c(0) \sec \theta \quad (69)$$

We define, for some real frequency f ,

$$\delta f(\theta) = f(\theta) - f(0) \sec \theta \quad (70)$$

where θ is measured from the field direction of minimum frequency, and expand assuming circular symmetry,

(25)

$$\delta f(\theta) = \alpha \theta^2 + \beta \theta^3 + \dots \quad . \quad (71)$$

The second derivative of the area is then given by

$$\left(\frac{\partial^2 A}{\partial k_z^2} \right)_{k_o, \theta=0} \approx \frac{4\pi\alpha}{f(0)} \quad (72)$$

from purely geometric arguments.

Another estimate can be obtained by assuming a one O.P.W. Fermi surface. A small neck in such a structure is drawn in figure 6. For sufficiently small pieces of the Fermi surface the cross sectional figures bounded by abc and a'b'c' will be approximately similar, allowing one to write

$$A(k_z) = A(k_o) \left(\frac{k_m^2}{k_{mo}^2} \right)^2 \quad (73)$$

where

k_m = the minimum Fermi momentum measured from the central axis as shown in figure 6

$k_{mo} = k_m$ at the point $k_z = k_o$.

The area derivative is then given by

$$\frac{\partial^2 A}{\partial k_z^2} = \frac{2A(k_o)}{(k_{mo})} \left(\frac{\partial^2 k_m}{\partial k_z^2} \right)_{k_o} \quad . \quad (74)$$

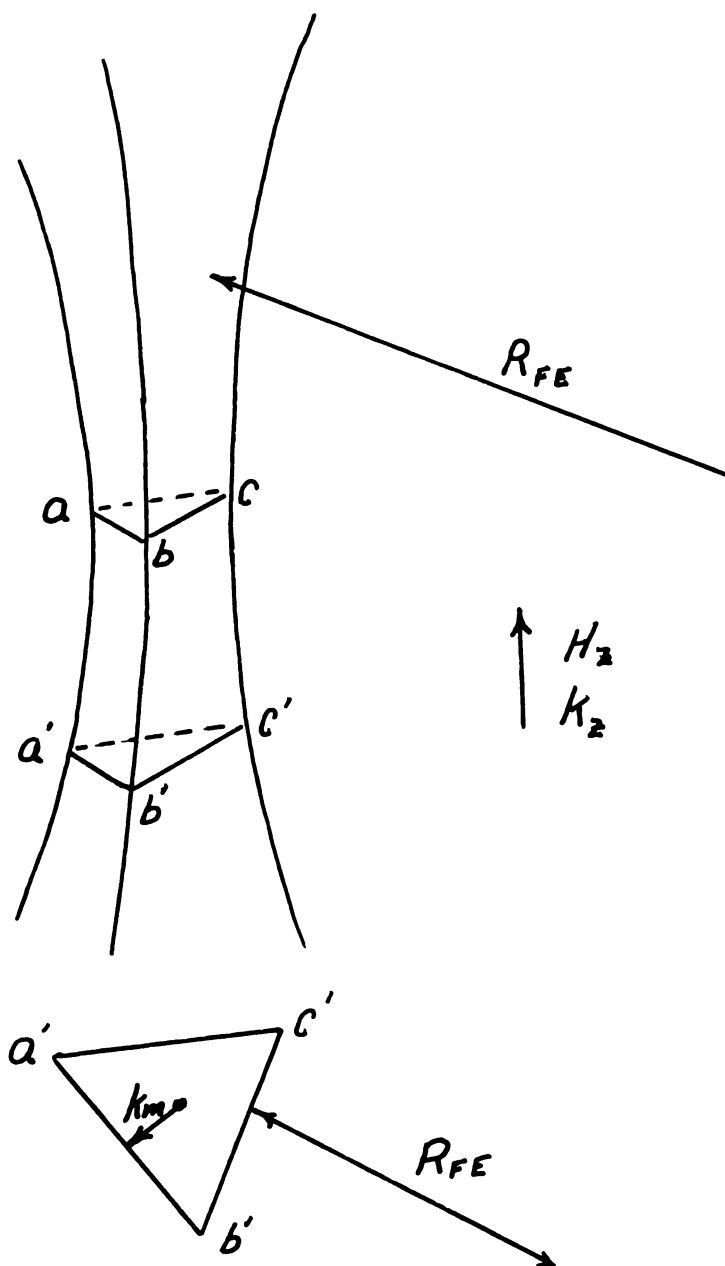


Figure 6. Curvature of a one OPW Fermi surface

(27)

The last factor in equation 74 can be estimated by recalling that the curvature of the Fermi surface is that of the free electron sphere in the one O.P.W. approximation.

$$\left| \left(\frac{\partial^2 k_m}{\partial^2 k_z} \right)_{k_o} \right| = R_{FE} \quad (75)$$

$$\left| \frac{\partial^2 A}{\partial k_z^2} \right|_{k_o, \theta=0} = 2A_o / k_{mo} R_{FE} \quad , \quad (76)$$

in which R_{FE} is the radius of the free electron sphere and is given by

$$R_{FE} = (3\pi^2 n_o)^{1/3} \quad . \quad (77)$$

Approximating the area by

$$A \approx \pi k_m^2 \quad , \quad (78)$$

which is an underestimate, we obtain

$$\left| \frac{\partial^2 A}{\partial k_z^2} \right|_{k_o, \theta=0} \approx \frac{2\sqrt{\pi A_o}}{(3\pi^2 n_o)^{1/3}} \quad , \quad (79)$$

n_o = total electron density.

Written in terms of the de Haas van Alphen frequency,

$$\left| \frac{\partial^2 A}{\partial k_z^2} \right|_{k_o, \theta=0} = \frac{2\sqrt{2} \pi \sqrt{\frac{e}{hc}} f^{1/2}}{(3\pi^2 n_o)^{1/3}} \quad . \quad (80)$$

(28)

The factor $[(\partial^2 A / \partial k_z^2)_{k_0}]^{-1/2}$ can be found in the standard expression for the free energy (equation 34). Another factor found there which will be used without justification is the Dingle factor inside the summation. Including both of these factors,

$$\tau_{25} = \frac{5\sqrt{2}}{6\sqrt{\pi}} \left(\frac{ce}{h}\right)^{1/2} \frac{kTm^* \Gamma f}{[(\partial^2 A / \partial k_z^2)_{k_0}]^{1/2} H^{3/2}} \times$$

$$\sum_{\nu} \frac{(-1)^{\nu}}{\sqrt{\nu}} A_3(\lambda) [\sin b] [\exp(\frac{\pi \nu}{\omega_c \tau})]$$

(81)

We must obtain an estimate of the relaxation time τ ; two methods of doing so are immediately apparent. The first is to use equation 54 and the zero field resistivity. Of course, since we are here using the free electron approximation and assuming that τ is independent of \vec{k} , this method may be used only in one O.P.W. like metals and in the low temperature impurity scattering regime. Furthermore m_0 and n_0 must be the free electron mass and the total number of electrons in the metal.

$$\tau_R = \frac{m_0}{e^2 n_0 \rho_0} \tag{82}$$

We might also use the value of τ_0 obtained from the Dingle scattering factor. This method has the advantage of

(29)

providing the local relaxation time on the part of the Fermi surface giving rise to the oscillations but has the disadvantage that τ_D is rather more difficult to extract from the data.

If there are N identical sections per Brillouin zone presenting a given cross sectional area we must multiply equation 69 by N.

The transverse resistivity ρ_{11} in equation 59 can take on a variety of forms. One of the most common and the only form considered here is

$$\rho_{11} = \rho_0 + \rho_2(\hat{h}, \hat{j})H^2 \quad (83)$$

$$\begin{aligned} \hat{h} &= \text{unit vector along } \vec{H} \\ \hat{j} &= \text{unit vector along } \vec{J} \end{aligned}$$

It is generally true that, when this is the behavior of ρ_{11} the second term completely dominates the first, above about ten kilogauss at liquid helium temperatures. Using only the second term,

$$\rho_{11} = \frac{5\sqrt{2}}{6\sqrt{\pi}} \left(\frac{ce}{h}\right)^{1/2} \frac{km^*fN\rho_2(\hat{h}, \hat{j})}{[(\partial^2 A / \partial k_z^2)]^{1/2} \tau} H^{1/2} \quad x$$

$$\sum_v \frac{(-1)^v}{v!} A_3(\lambda) \left[\exp\left(\frac{-\pi v}{\omega_c \tau_D}\right) \right] \sin b \quad .$$

(84)

There is a very interesting variant of equation 84. By applying Kohler's rule to equation 82 we find that

(30)

$\rho_2(\hat{h}, \hat{j})$ depends upon residual resistivity in a very special way, namely that

$$\rho_2(h, j) = \frac{a(h, j)}{\rho_0} \quad (85)$$

where $a(\hat{h}, \hat{j})$ is not a function of the zero field resistivity. Putting this into equation 84, coupled with the substitution for τ given in equation 82,

$$\begin{aligned} \mathfrak{S}_{11} = & \frac{5\sqrt{2}}{6\sqrt{\pi}} \left(\frac{ce}{h} \right)^{1/2} \frac{Nke^2 n_0}{[(\partial^2 A / \partial k_z^2)_{k_0}]^{1/2}} \left(\frac{m^*}{m_0} \right) fH^{1/2} a(\hat{h}, \hat{j}) \times \\ & \sum_{\nu} \frac{(-1)^{\nu}}{\nu} A_3(\lambda) \left[\exp\left(-\frac{\pi\nu}{\omega_c \tau_D}\right) \right] \sin b \quad (86) \end{aligned}$$

in which τ no longer appears.

The summation in equation 86 contains all of the oscillatory dependence. The relative harmonic content is a rather complicated function of temperature and magnetic field. The function $A_3(\lambda)$ is plotted in figure 7. The maximum value is very nearly unity.

(31)

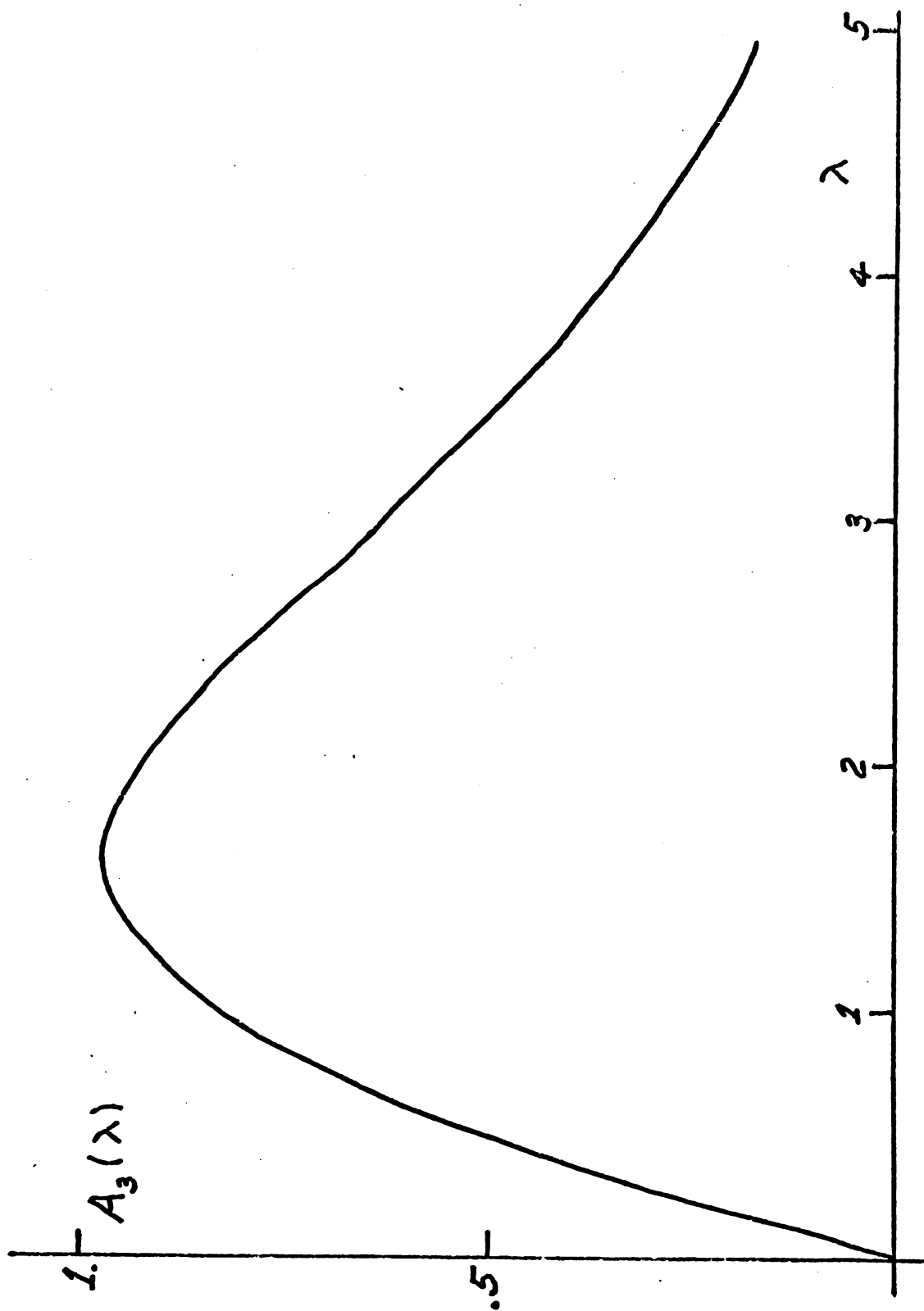


Figure 7. $A_3(\lambda)$ vs. λ

V. Nonoscillatory Magnetothermoelectricity

In view of the information concerning Fermi surface topology which is contained in the high field magnetoresistance of single crystals we might ask what effect this topology has upon the thermoelectric power. Bychkov, Gurevich and Nedlin²⁴ have made qualitative calculations; their results indicate that the diagonal terms of the Seebeck tensor should saturate at high fields except for the case of a compensated metal with no open orbits. In this case, the transverse diagonal elements should be linear in magnetic field.

VI. Experimental Approach

A. Seebeck Measurements at Low Temperatures

Typical Seebeck coefficients of metals in the liquid helium temperature range are so small that the direct measurement of a thermoelectric emf requires the measurement of a voltage as small as 10^{-11} volts. This would be difficult under any circumstances but the problems are compounded in this case by the temperature gradients supported by the measuring leads. These gradients can cause variable thermal voltages on the order of a microvolt or more. A number of devices built to cope with this problem have been reported,²⁵⁻³¹ the most sensitive of which is capable of measuring Seebeck coefficients of about $5 \times 10^{-9} \text{ v/K}^\circ$ at about 2°K .

B. Peltier Measurements, General

The sensitivity of carbon resistance thermometry at liquid helium temperatures suggests that a measurement of the Peltier effect may be more sensitive than a Seebeck measurement. The simplest experimental arrangement would be that shown in figure 8. The two samples A and B are suspended from a heat sink at temperature T_0 and a current I is passed through the junction. The temperature difference ΔT will consist of a Joule term proportional to I^2 and Peltier and Thompson terms proportional to I .

$$\Delta T = \frac{1}{K} [RI^2 + \Pi I] + gI \quad (87)$$

Here K is the thermal conductance from the junction to the bath, R is the junction resistance plus some fraction of the

(34)

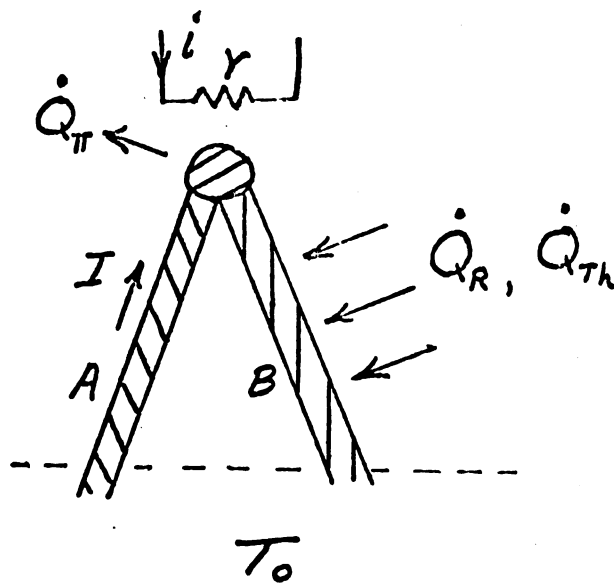


Figure 8. Experimental Peltier junction

(35)

sample resistances, and g is a constant involving the Thompson coefficient. For the present we shall neglect this term, requiring that it be small. To this order, the junction temperature change caused by a reversal of current direction is

$$\delta T = \Delta T_{+I} - \Delta T_{-I} = \frac{1}{K}(2\Pi I) \quad . \quad (88)$$

The addition of a known amount of heat, $\dot{Q}_r = ri^2$, to the junction causes a temperature change of

$$\delta T_r = \frac{1}{K}(ri^2) \quad . \quad (89)$$

Solving equations 88 and 89 for Π ,

$$\Pi = \Pi_A - \Pi_B = \frac{ri^2}{2I} \frac{\delta T}{\delta T_r} \quad . \quad (90)$$

Being a reversible effect, the Thompson heat also contributes to δT . The difficulty in the treatment of this effect is that it is distributed along the length of the samples and its effect on the junction temperature depends upon the temperature distribution along the samples. We will assume that a fraction η of this term is effective, i.e.,

$$\Delta T_{th} = \eta \dot{Q}_{th}/K \quad . \quad (91)$$

By equation 6,

$$\Delta T_{th} = \frac{\eta I(\Delta T)}{K} (\mu_A - \mu_B) \quad , \quad (92)$$

and using the Kelvin relations,

(36)

$$\Delta T_{th} = \eta T \frac{d[S_A - S_B]}{dT} \frac{I(\Delta T)}{K} . \quad (93)$$

If the Seebeck coefficients are slowly varying functions of temperature,

$$(\Delta T)_{th} \approx \frac{\eta(\Pi_A - \Pi_B)}{K} I\left(\frac{\Delta T}{T}\right) . \quad (94)$$

This must be kept small in comparison with $\Pi I/K$, resulting in the restriction that

$$\frac{\Delta T}{T} \ll 1/\eta . \quad (95)$$

It is experimentally justifiable to require that

$$\frac{\Delta T}{T} \leq .04 \quad (95a)$$

for measurements accurate to about one percent.

The ΔT referred to in equation 95, the total temperature difference across the samples, is in most cases dominated by the Joule term,

$$\Delta T_J = RI^2/K . \quad (96)$$

Combining equations 88, 95 and 96, we obtain

(37)

$$\frac{\Delta T}{T} = \frac{4\pi^2 T}{RK(\delta T_{\pi})^2} \leq .04 \quad (97)$$

which puts a lower limit on the measurable Peltier coefficient.

$$\pi^2 \geq \left(\frac{RK}{2T}\right) \left(\frac{\delta T_0}{2}\right)^2 \times 25 \quad (98)$$

Here δT_0 represents the smallest temperature change that can be measured accurately. This is, of course, a function of temperature, thermal stability, and thermometer circuitry. It is an empirical fact that we are able to measure changes of about 10^{-5} Kelvin degrees to a few percent accuracy at 2°K , so that equation 98 becomes

$$|\pi| \geq (2.5) \left(\frac{RK}{T}\right)^{1/2} \times 10^{-5} \quad (99)$$

The most favorable conditions for this measurement would include a superconducting reference metal B, so that the electrical resistivity and thermal conductivity of this arm can be neglected. If the junction resistance is small, we may write

$$R \approx \eta_0 A L / a \quad (100)$$

in which L , a are the length and cross sectional area of

(38)

the sample. If the thermal conductance is due only to the thermal path through A,

$$K = k_A a / L \quad (101)$$

where k_A is the thermal conductivity of the material. Recalling that

$$\begin{aligned} \rho k &= L_o T \\ L_o &= \text{Lorenz number,} \end{aligned} \quad (102)$$

we see that

$$\Pi \geq 2L_o^{1/2} \times 10^{-5}. \quad (103)$$

The Lorenz number for impurity scattering is just the classical value, given by

$$L_o = 2.4 \times 10^{-8} \text{ MKS units } , \quad (104)$$

$$\Pi \geq 3 \times 10^{-9} \text{ v} \quad (105)$$

which is equivalent to a Seebeck coefficient of about $1.5 \times 10^{-3} \mu\text{v/K}^\circ$ at 2°K .

It is obvious that the above calculation concerning the Thompson heat correction is by no means rigorous although

it does provide useful guidelines. It is not difficult to formulate the problem in more detail and in fact solutions can be found under certain simplifying assumptions. Some of this work has been done and is discussed in Appendix III. Very little new and useful information can be obtained beyond the fact that the Peltier coefficient measured corresponds to that at some temperature between T_0 and $T_0 + \Delta T$; the exact temperature depends very critically on the assumptions. However, even this fact is dependent upon smoothly varying Peltier coefficients and small temperature differences.

The reference material must be chosen with some care. One would expect that a superconductor would be ideal, as it possesses no electrical resistivity, high thermal resistivity and zero Peltier coefficient. In the zero field measurements a superconductor was in fact used (see Appendix II). Unfortunately in high magnetic fields one would have to use hard superconductors, which have a number of undesirable qualities. It is very difficult to obtain a good electrical contact to these materials, as no known solder will wet them. Furthermore they are all very stiff, and using them in the confined volume inside a magnet dewar presents technical difficulties. Nevertheless, these difficulties could be overcome if necessary. In the measurements made on zinc, however, the quantum oscillations were of primary concern. These are, of course, unaffected by thermoelectric heats generated by the reference. Furthermore the size of these effects are such as not to require maximum sensitivity.

The use of normal metals still requires an optimization of the measurements by adjusting the size of wire to be used. One must choose this in such a way that the electrical and thermal resistance are at least of the same order of magnitude as that of the crystalline sample in high magnetic

fields. It is also desirable that the Peltier or Seebeck coefficient of the reference is known, although this does not affect the amplitude of the single crystal quantum oscillations. Since a severely cold worked metal has a more predictable low temperature behavior in its Seebeck coefficient (see iron data in Appendix II), it may be advantageous to use such a reference material.

C. Thermal Contact Considerations

There are a number of requirements on relative thermal paths which assure that the constants K appearing in equations 88 and 89 are identical. In particular, placing the thermometer and the calibrating heater onto the same block which in turn is in contact with the junction may produce erroneous results. This situation is shown schematically in figure 9a. If the thermal resistance W_1 is not much smaller than W_2 , the measurements would be in error by the factor $(W_2 + W_1)/W_2$. However, if the situation can be represented by figure 9b, the temperature differences measured at the carbon resistor are

$$\delta T_j = q_j \left(\frac{W_3 W_1}{W_1 + W_2} \right) \left\{ \frac{W_5 + W_6}{\frac{W_3(W_1 + W_2)}{W_1 + W_2 + W_3} + W_4 + W_5 + W_6} \right\} \quad (106)$$

for heat q_j produced at the junction, and

$$\delta T_h = q_h \left(\frac{W_3 W_1}{W_1 + W_2} \right) \left\{ \frac{W_6}{\frac{W_3(W_1 + W_2)}{W_1 + W_2 + W_3} + W_4 + W_5 + W_6} \right\} \quad (107)$$

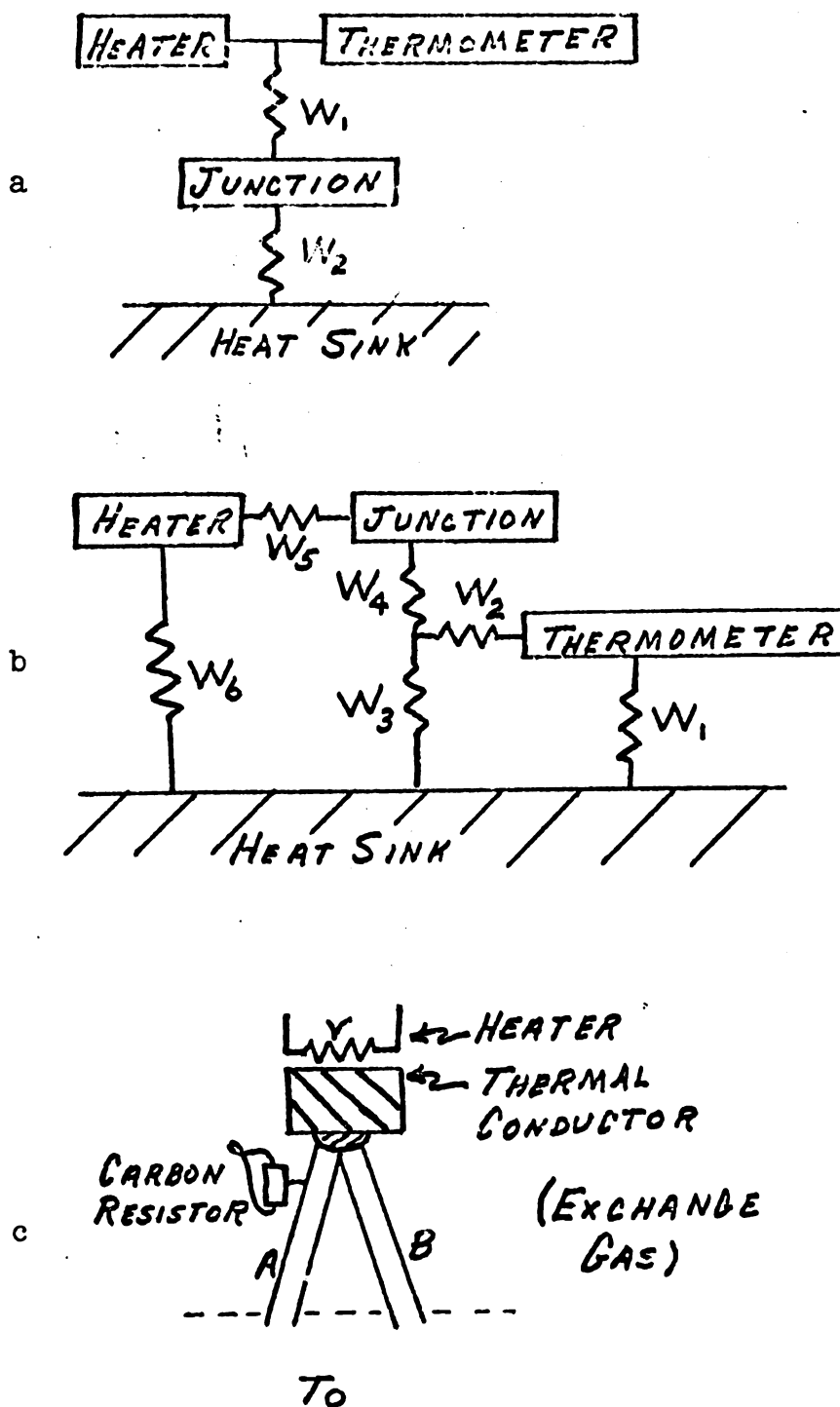
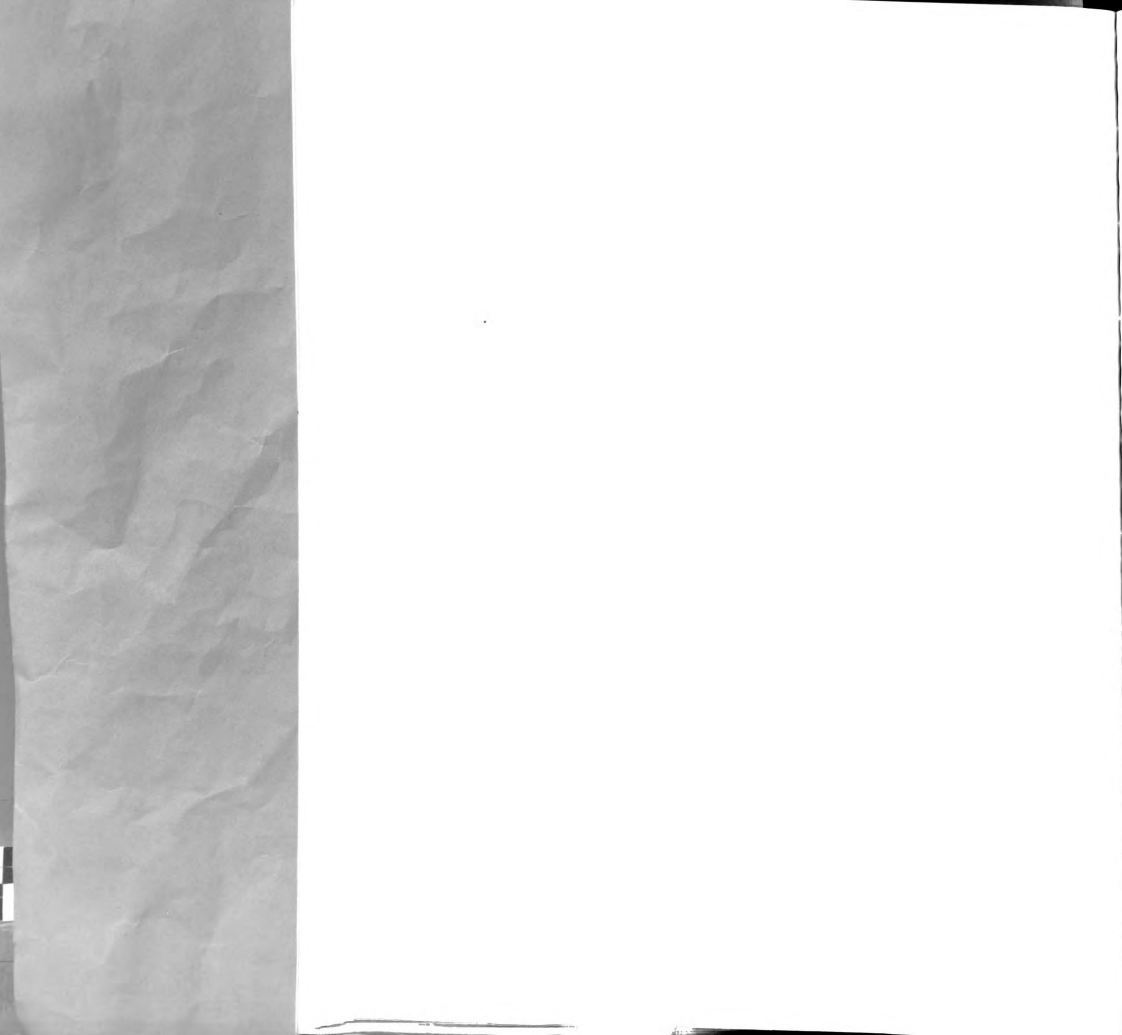


Figure 9. Thermal contact diagrams



(42)

for a heat \dot{q}_h produced by the heater. These differ only to order W_5/W_6 .

Figure 9c shows an experimental arrangement that can be represented by 9b. In this case, W_5 is the thermal resistance through the thermal conductor between the junction and the heating resistor r , W_6 consists of the high resistance leads to the heater as well as any exchange gas in the system; W_5 can be much smaller than W_6 with little difficulty. In practice it is found that exchange gas pressures up to 50 microns do not affect the measurements.

D. Double Junction Technique

There are a number of advantages to the double junction system shown in figure 10. The center of sample A is anchored at temperature T_o , as are the lead wires B. The carbon resistors C_1 and C_2 constitute two arms of a Wheatstone bridge, and if the response of this thermometry system is linear (see Appendix IV), the bridge output v is given by

$$v = G_1(\Delta T_1 - \Delta T_2) + G_2 \quad (108)$$

in which G_1 represents the bridge sensitivity, G_2 an adjustable bridge offset, and ΔT_1 , ΔT_2 are defined as in figure 10. Neglecting the Thompson heat,

$$v = G_1 \left\{ \left(\frac{R_1}{K_1} - \frac{R_2}{K_2} \right) I^2 + II \left(\frac{1}{K_1} + \frac{1}{K_2} \right) + \frac{r_1 i_1^2}{K_1} + \frac{r_2 i_2^2}{K_2} \right\} + G_2, \quad (109)$$

for a heat Q produced by the heater. These differ only to order W_0/W_1 .
 Figure 9c shows an experimental arrangement that can be represented by Fig. 9b. In this case, W_1 is the thermal resistance through the thermal conductor between the junction and the heating resistor R_1 . W_0 consists of the high resistance leads to the heater as well as any exchange gas in the system; W_0 can be much smaller than W_1 with little difficulty. In practice it was found that exchange gas pressures up to 50 microns did not affect the measurements.

d. Double Junction Technique

There are a number of advantages to the double junction system shown in Figure 10. The center of sample A is anchored at temperature T_0 , as are the lead wires B. The carbon resistors C_1 and C_2 constitute two arms of a Wheatstone bridge, and the response of this thermometry system is linear (see Appendix IV), the bridge output v is given by

$$v = G_1(\Delta T_1) + G_2(\Delta T_2) \quad (10)$$

in which G_1 represents the bridge sensitivity, G_2 an adjustable bridge offset, and ΔT_1 , ΔT_2 are defined as in Figure 10. Neglecting the Thomson heat,

$$v = G_1 \left\{ \frac{R_2}{K_1} - \frac{R_2}{K_2} \right\} T_0 + R_1 \left(\frac{1}{K_1} + \frac{1}{K_2} \right) T_0 + \frac{R_1}{K_1} \Delta T_1 + \frac{R_1}{K_2} \Delta T_2 \quad (10)$$

(43)

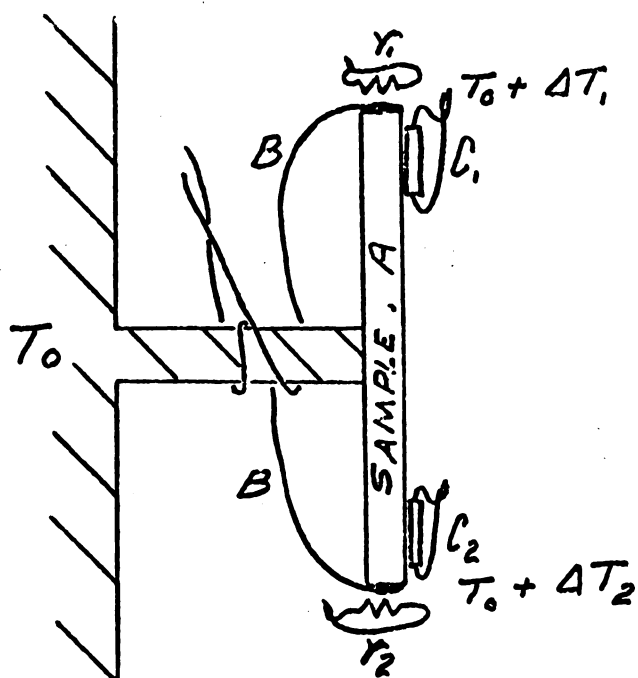
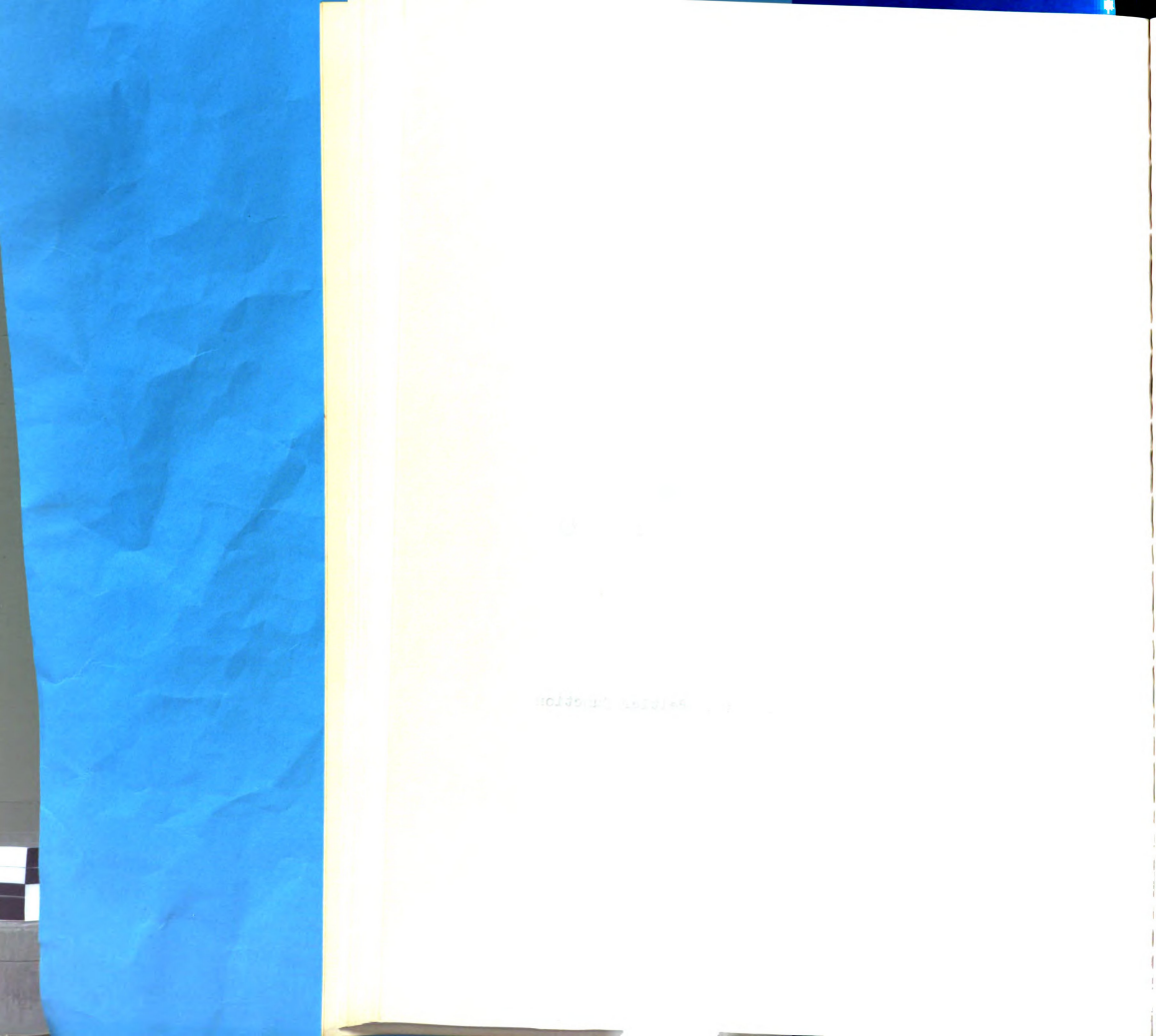


Figure 10. Double Peltier junction



(44)

where i_1 and i_2 are the currents through the heating resistors r_1 and r_2 . All other symbols have meanings analogous to those in equations 87 to 90. Reversing the sample current results in a change in v given by

$$\delta v_{\pi} = G_1 \left\{ 2\pi I \left(\frac{1}{K_1} + \frac{1}{K_2} \right) \right\} \quad (110)$$

For calibration we start with $i_1=i_0$, $i_2=0$ and switch to $i_1=0$, $i_2=i_0$. The resulting change in bridge output is

$$\delta v_r = G_1 \left\{ i_0^2 \left(\frac{r_1}{K_1} + \frac{r_2}{K_2} \right) \right\} \quad (111)$$

Evidently if $r_1 = r_2 = r$,

$$\pi = \frac{i_0^2 r}{2I} \frac{\delta v_{\pi}}{\delta v_r} \quad (112)$$

If the carbon resistors have differing sensitivities one must replace equation 108 with

$$v = G_{11}(\Delta T_1) - G_{12}(\Delta T_2) + G_2 \quad (113)$$

but this has no effect on equation 112.

Besides the obvious doubling of sensitivity obtainable by this method it has the further advantage that the

where i_1 and i_2 are the currents through the heating resistors r_1 and r_2 . All other symbols have meanings analogous to those in equation (10). Reversing the sample current results in a change in γ given by

$$\Delta \gamma = \frac{1}{\gamma} \left(\frac{\Delta i_1}{i_1} - \frac{\Delta i_2}{i_2} \right) \quad (110)$$

For calibration we start with $i_1 = i_2$, $i_2 = 0$ and write to first order $\Delta \gamma = \frac{1}{\gamma} \frac{\Delta i_1}{i_1}$. The resulting change in bridge output is

$$\Delta V_x = \frac{1}{2} \left(\frac{\Delta i_1}{i_1} - \frac{\Delta i_2}{i_2} \right) \quad (111)$$

Evidently if $r_1 = r_2 = r$,

$$\Delta \gamma = \frac{1}{\gamma} \frac{\Delta i_1}{i_1} \quad (112)$$

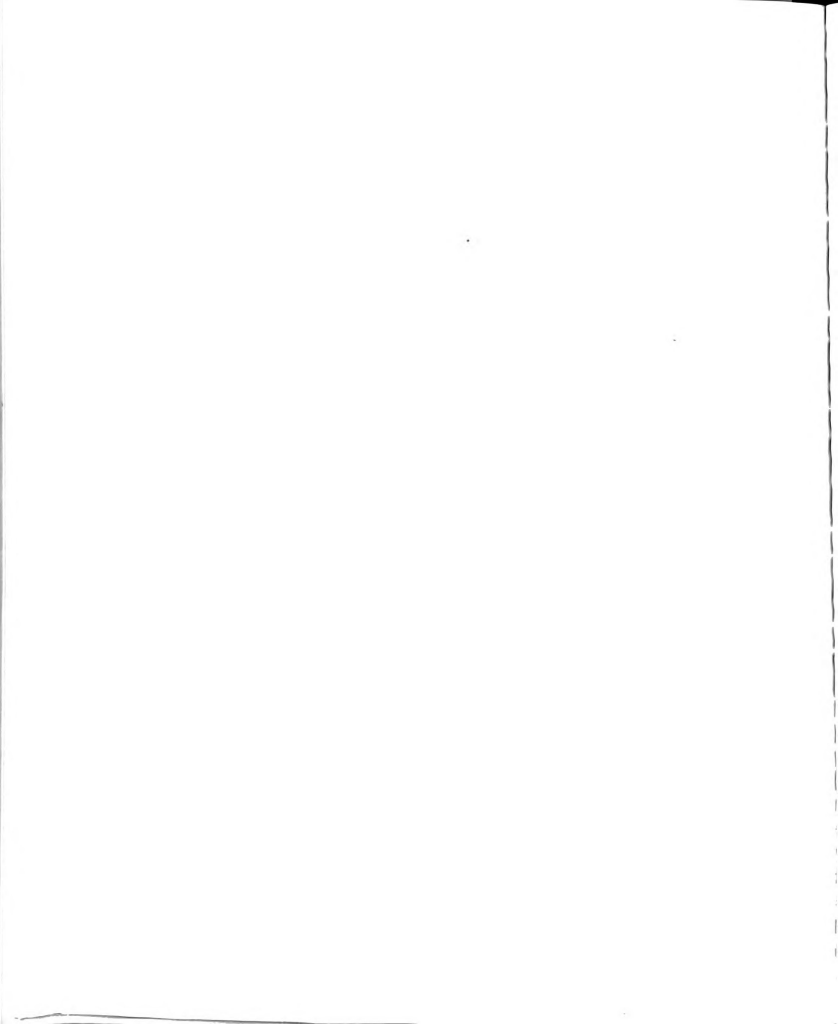
If the carbon resistors have different sensitivities one must replace equation (10) with

$$\gamma = \frac{1}{2} \left(\frac{\Delta i_1}{i_1} - \frac{\Delta i_2}{i_2} \right) + \frac{\Delta r_1}{r_1} - \frac{\Delta r_2}{r_2} \quad (113)$$

but this has no effect on equation (112). Besides the obvious doubling of sensitivity obtainable by this method it has the further advantage that the

(45)

Joule temperature differences of the two arms tend to cancel (see equation 109). This is particularly useful for continuous measurements in a changing magnetic field, in which the magnetoresistance causes large changes in the individual Joule terms.



VII. Experimental Apparatus

A. Cryostat

Figure 11 is a diagram of the lower portion of the cryostat. The sample chamber was evacuated through stainless steel supporting tubes. The projection at the base of the sample holder was soldered through a hole at the bottom of the enclosing can during the runs but otherwise the sample holder was supported only by the twelve pin electrical connector at the top. This arrangement allowed the removal of this section when mounting new samples, while still assuring rigidity in operation.

The ten mil sample current leads were run directly from the connector to the ends of the sample and were either Pb of six-nines purity or four-nines silver, severely cold worked. All other leads went through a secondary connector at the terminal boards. Seven mil copper leads were run from the connector through holes in these boards, and held in place with G.E. 7031 varnish. In order to limit heat conduction down these leads they were wrapped around the supporting rods. The ends sticking out of the terminal boards were then clipped to about $3/16$ in. and the coating stripped off to provide a soldering "post".

The carbon resistors were attached to the sample with G.E. 7031 varnish using one layer of cigarette paper as an insulator. Care was taken to place the two resistors on the same side of the crystal in order to minimize interference from transverse effects. The leads from these to the terminal boards were three mil manganin wire, twisted together to minimize pickup noise.

The calibrating heaters were coils of manganin wire

A. Overview

Figure 10 is a diagram of the lower portion of the apparatus. The sample circuit was connected through a lead at the top of the sample holder. The connection at the base of the sample holder was connected through a hole at the bottom of the electrode container. The same but other-
 was the sample holder was supported only by the twelve pin electrical connector at the top. This arrangement allowed the removal of the reaction vessel containing new samples, while still assuming stability in operation.

The ten mill ampere current leads were run directly from the connector to the ends of the sample and were either 10 or six-mill ampere or four-mill ampere, never less than worked. All other leads went through a secondary connector at the terminal boards. Seven mill copper leads were run from the connector through holes in these boards, and held in place with G.E. 7031 varnish. In order to limit heat conduction down these leads they were wrapped around the supporting rods. The ends attaching one of the terminal boards were then clipped to about 1/16 in. and the coating stripped off to provide a soldering "post".

The carbon resistors were attached to the sample with G.E. 7031 varnish using one layer of cigarette paper as an insulator. Care was taken to place the two resistors on the same side of the crystal in order to minimize interference from transverse effects. The leads from these to the terminal boards were three mill manganin wire, twisted together to minimize pickup noise.

The calibrating lead wires were coils of manganin wire

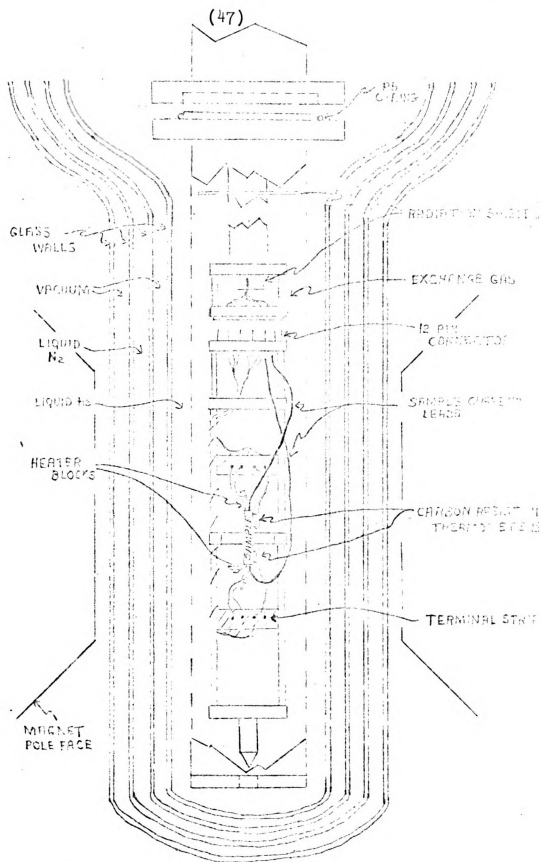


Figure 11 . Cryostat



PRINTED IN GREAT BRITAIN

on 1/2 in. lengths of approximately 50 mil copper wire, potted in G.E. 7031 varnish. The copper form was soldered directly to the junction. About two or three feet (70-100 Ω) of manganin wire was used, one inch (3%) of which was used as leads to the terminal board.

As only the room temperature resistance of the heaters was measured the resistance ratio and magnetoresistance of manganin were needed. These measurements were made and are discussed in Appendix V.

The samples were in the form of a rod about 1/2 in. in length and 3/32 in. in diameter. They were soldered to the support with Cerrolow 117 solder.

The dewar fit between the pole faces of the magnet as shown in figure 11. The magnet could be rotated about the axis of the dewar. Obviously the current in the sample always flowed transverse to the magnetic field direction, to the accuracy of the sample alignment (Appendix VII).

B. Pumping System

There was very little to this "system". It consisted of a mechanical vacuum pump, a valve, and a thermocouple gauge. Although a diffusion pump was available in the system it was used only for purposes of leak detection.

An exchange gas pressure of about ten microns, measured at 4°K, was needed in the sample chamber to provide a thermal path from the sample to the liquid helium bath. After this was admitted the system was closed off and left unpumped for the remainder of the run.

on a $1/8$ in. diameter approximately 50 mil copper wire, potted in G.E. 7021 varnish. The copper lead was soldered directly to the junction. About two or three feet (70-100 ft) of manganin wire was used, one inch (3%) of which was used as leads to the terminal board.

As only the room temperature resistance of the heaters was measured the resistance ratio and magneto-resistance of manganin wire needed. These measurements were made and are discussed in Appendix V.

The samples were in the form of a rod about $1/2$ in. in length and $3/32$ in. in diameter. They were soldered to the supports with Germeton 17 solder.

The dewar fit between the pole faces of the magnet as shown in Figure 11. The magnet could be rotated about the axis of the dewar. Obviously the current in the sample always flowed transverse to the magnetic field direction. To the accuracy of the sample alignment (Appendix VII).

B. Pumping System

There was very little to this "system". It consisted of a mechanical vacuum pump, a valve, and a thermocouple gauge. Although a diffusion pump was available in the system it was used only for purposes of leak detection. An exchange gas pressure of about ten microns, measured at 4°K, was needed in the sample chamber to provide a thermal path from the sample to the liquid helium bath. After this was admitted the system was closed off and left unpumped for the remainder of the run.

C. Measuring Electronics

A block diagram of the measuring circuit is shown in figure 12. The bridge-phase sensitive detector 1 (PSD1) was the basic thermometer circuit and the output from PSD1 was just the v referred to in equation 108. In the simplest mode PSD2 was omitted from the circuit and the output from PSD1 charted by the strip chart recorder. A standard switching sequence then produced a square wave-like trace on the chart from which the ratio $\delta v_{\pi} / \delta v_r$ was obtained. PSD2 was used for detection at the switching frequency. When this was in use only the sample current was switched so that the output from PSD2 was proportional to $2\pi |I| / K$. A more extensive description of the operation will be given in the next section.

Only the control box and bridge were not commercially made. Identification of the other units are as follows:

Sample current supply--Princeton Applied Research
model Tc-602R constant
voltage supply, modified
as suggested in the manual

PSD1--PAR model JB⁴ with model CR⁴-A preamplifier

PSD2--PAR model HR-8 with type C preamplifier

Recorder--Texas Instruments ServoRiter II

Figure 13 is a circuit diagram of the bridge used in this work. It is a standard Wheatstone bridge with a number of special features which facilitate its use in low tempera-

Figure 13 is a circuit diagram of the bridge used in this work. It is a standard Wheatstone bridge with a number of special features which facilitate its use in low frequency-

Recorder--Texas Instruments ServoRecorder XI

FD25--PAR model HR-2 with type C preamplifier

FD11--PAR model 1M5 with model CM5-A preamplifier

as suggested in the manual
voltage supply, modified
model TC-605R constant
sample current supply--Frickson Applied Research

made. Identification of the other units are as follows:

Only the control box and bridge were not commercially

in the next section.

A more extensive description of the operation will be given that the output from FD25 was proportional to $251/V_1$.

this was in use only the sample current was switched so

was used for detection at the switching frequency. When

chart from which the table "v₁" was obtained. FD25

ing sequence then produced a square wave-like trace on the

FD21 checked by the strip chart recorder. A standard auto-

mode FD25 was checked from the circuit and the output from

that the v₁ referred to in equation 106. In the subsequent

for the basic three-resistor circuit and the output from FD21

Figure 12. The bridge-circuit sensitive detector I (FD21)

A block diagram of the measuring circuit is shown in

C. Measuring Microphones

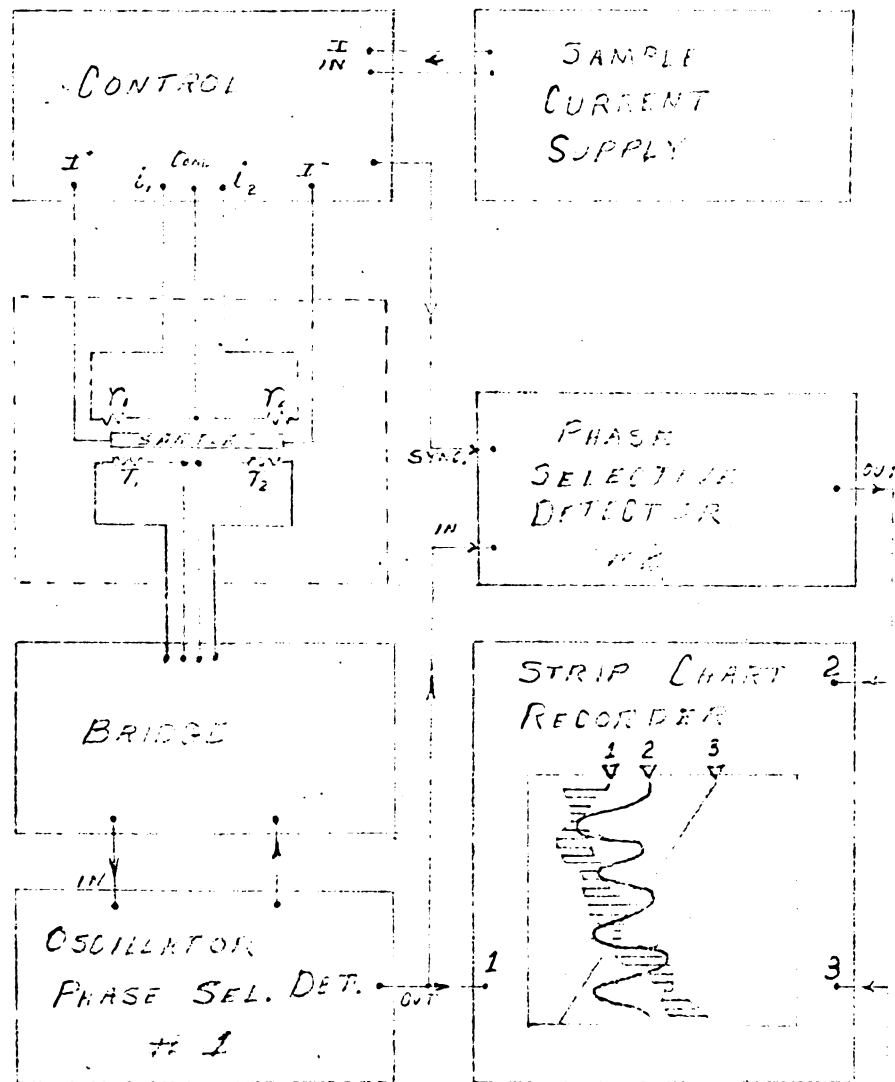
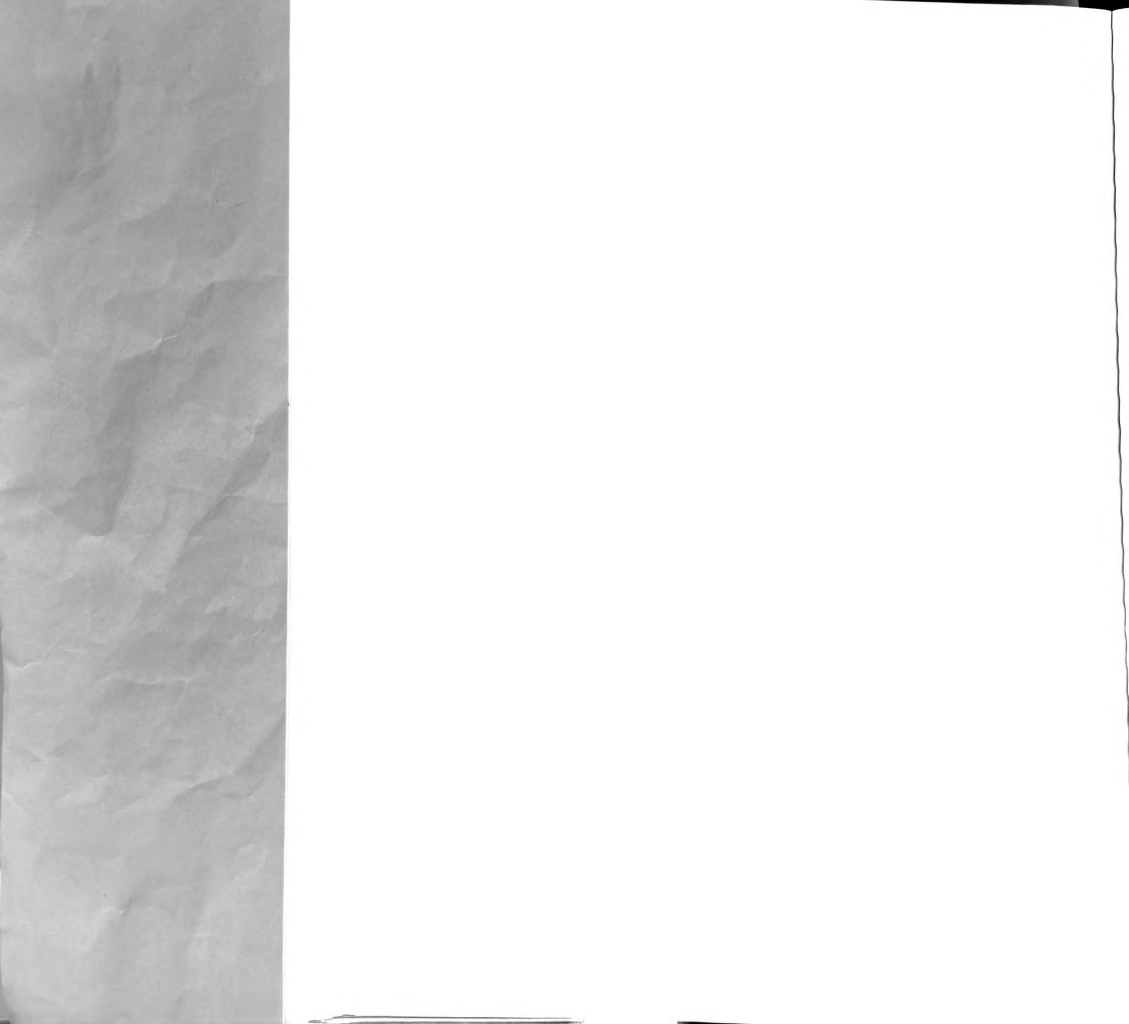


Figure 12. Measuring electronics



ture differential thermometry.

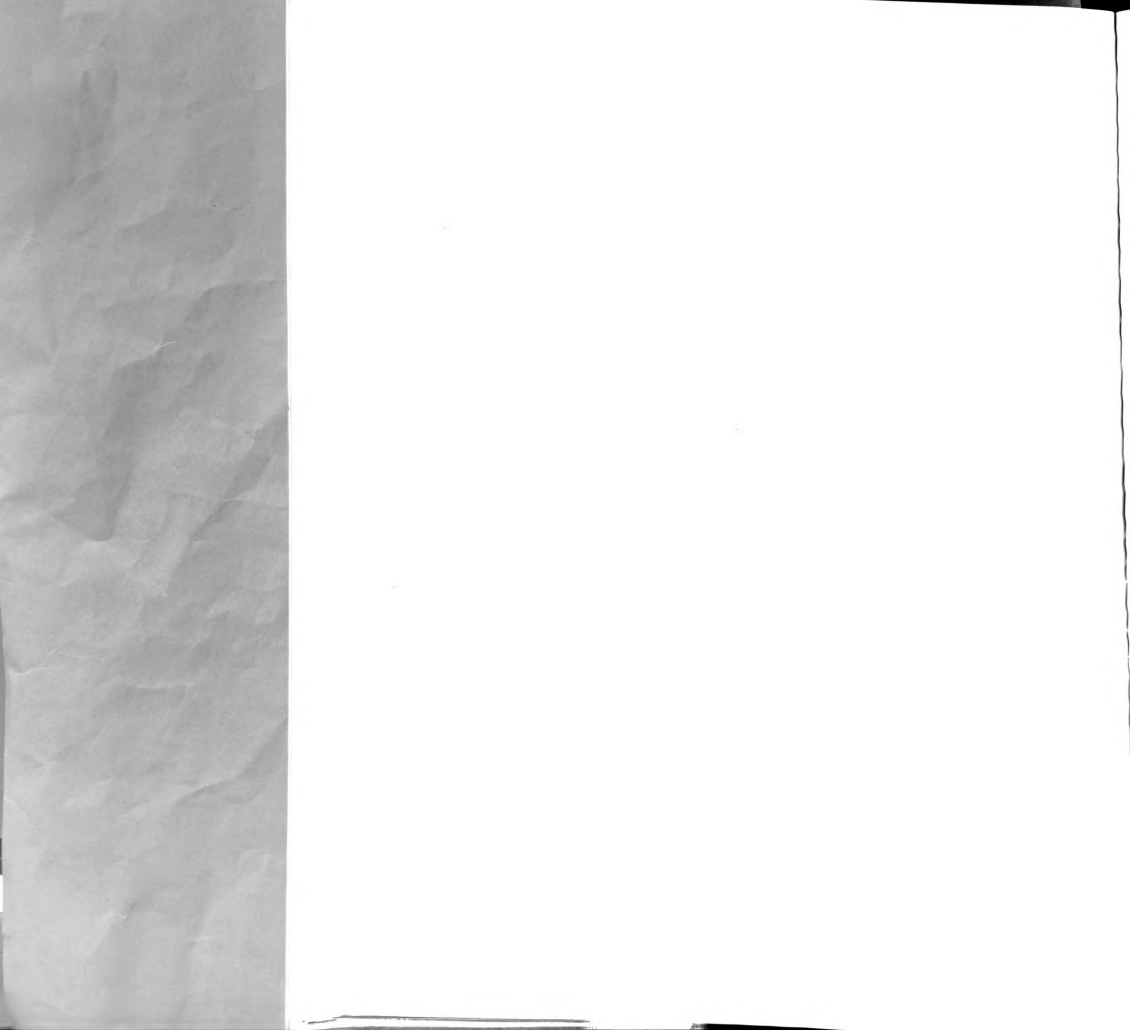
The carbon resistors were connected to J3 as shown in figure 14a. The reason for using four leads becomes apparent when considering figure 14b, which is a diagram of the bridge in a calibrating mode. This lead arrangement added the lead resistance to both arms (R_{C1} and R_S) so that at balance $R_S = R_{C1}$.

The total resistance of the ratio arms of the bridge could be selected as 2K, 6K, 20K, 60K or 200K. For purposes of standardization either the ratio arms or the cryostat arms could be replaced by 5K, 1 per cent resistors. There was also a provision for changing the resistance of one of the bridge arms by .1, 1, 10, or 100 Ω , an input attenuating network, and an out of phase balance network. The latter was used to eliminate the out of phase signal arising from interlead capacitance.

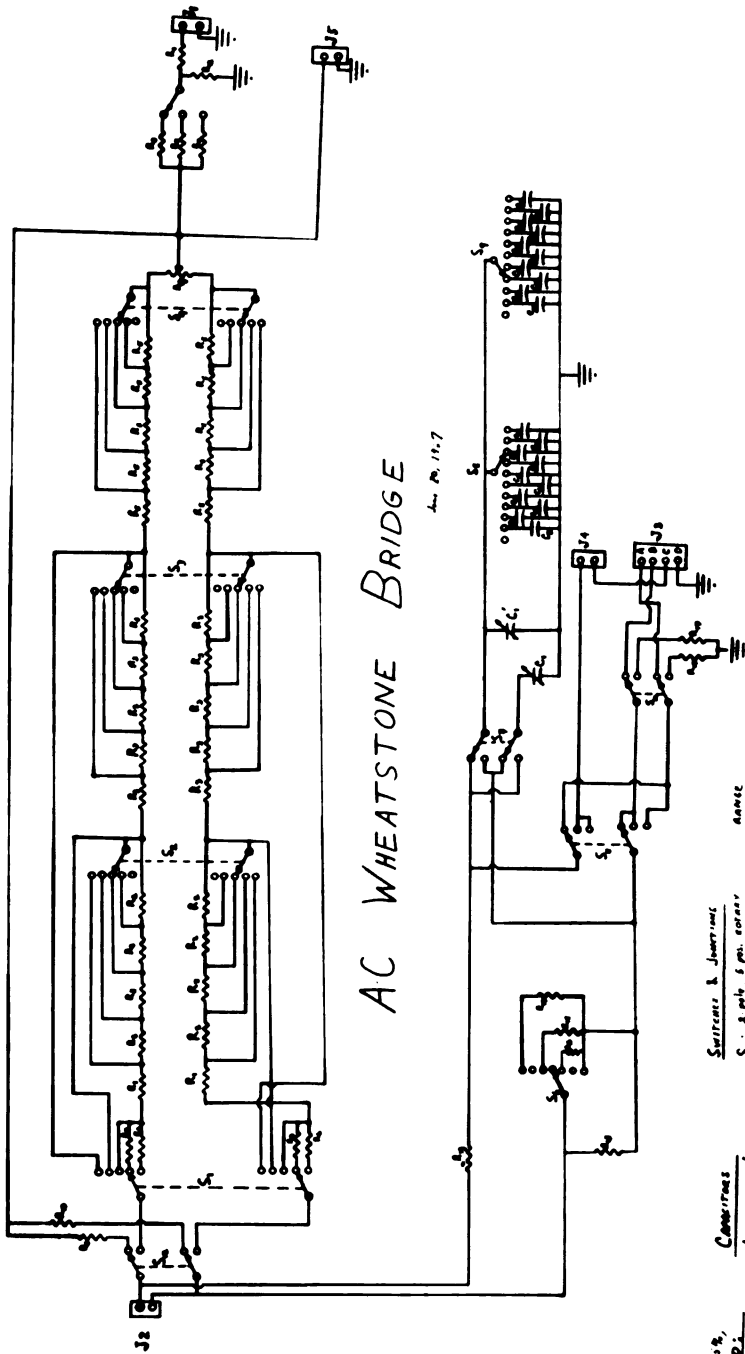
The control panel contained all of the switching circuitry as well as the current source for the calibrating heaters. Figure 15 is a complete circuit diagram.

The power supply section of the control panel was a standard type of regulated supply, capable of a 10 volt output but set to about 6.5 volts. The heater current control was a simple potential divider-current limiter circuit with full range currents of about .01, .1, 1, or 3 ma. R_1 was a 1333 Ω , .2 per cent resistor used to measure the heater current. The potential across R_1 was fed directly to pins 5 and 6 of connector C_1 . A schematic of this portion of the circuit is shown in figure 17a.

The sample current was passed through the reversing switch shown in 17b. The relays were arranged as shown so that one was off for both current directions, thereby reducing the load on the internal power supply. This current was measured by measuring the potential across the 3.784 Ω



YR04HL



AC WHEATSTONE BRIDGE

Am. No. 112.7

All resistors A W. 1/2, better as noted.

Capacitors

C1-C100 = 100 pF each

Switches & Joints

S1: 2 pole 6 pos rotary

S2: 2 pole 6 pos rotary

S3: 2 pole 6 pos rotary

S4: 2 pole 6 pos rotary

S5: 2 pole 6 pos rotary

S6: 2 pole 6 pos rotary

S7: 2 pole 6 pos rotary

S8: 2 pole 6 pos rotary

S9: 2 pole 6 pos rotary

S10: 2 pole 6 pos rotary

S11: 2 pole 6 pos rotary

S12: 2 pole 6 pos rotary

S13: 2 pole 6 pos rotary

S14: 2 pole 6 pos rotary

S15: 2 pole 6 pos rotary

S16: 2 pole 6 pos rotary

S17: 2 pole 6 pos rotary

S18: 2 pole 6 pos rotary

S19: 2 pole 6 pos rotary

S20: 2 pole 6 pos rotary

S21: 2 pole 6 pos rotary

S22: 2 pole 6 pos rotary

S23: 2 pole 6 pos rotary

S24: 2 pole 6 pos rotary

S25: 2 pole 6 pos rotary

S26: 2 pole 6 pos rotary

S27: 2 pole 6 pos rotary

S28: 2 pole 6 pos rotary

S29: 2 pole 6 pos rotary

S30: 2 pole 6 pos rotary

S31: 2 pole 6 pos rotary

S32: 2 pole 6 pos rotary

S33: 2 pole 6 pos rotary

S34: 2 pole 6 pos rotary

S35: 2 pole 6 pos rotary

S36: 2 pole 6 pos rotary

S37: 2 pole 6 pos rotary

S38: 2 pole 6 pos rotary

S39: 2 pole 6 pos rotary

S40: 2 pole 6 pos rotary

S41: 2 pole 6 pos rotary

S42: 2 pole 6 pos rotary

S43: 2 pole 6 pos rotary

S44: 2 pole 6 pos rotary

S45: 2 pole 6 pos rotary

S46: 2 pole 6 pos rotary

S47: 2 pole 6 pos rotary

S48: 2 pole 6 pos rotary

S49: 2 pole 6 pos rotary

S50: 2 pole 6 pos rotary

S51: 2 pole 6 pos rotary

S52: 2 pole 6 pos rotary

S53: 2 pole 6 pos rotary

S54: 2 pole 6 pos rotary

S55: 2 pole 6 pos rotary

S56: 2 pole 6 pos rotary

S57: 2 pole 6 pos rotary

S58: 2 pole 6 pos rotary

S59: 2 pole 6 pos rotary

S60: 2 pole 6 pos rotary

S61: 2 pole 6 pos rotary

S62: 2 pole 6 pos rotary

S63: 2 pole 6 pos rotary

S64: 2 pole 6 pos rotary

S65: 2 pole 6 pos rotary

S66: 2 pole 6 pos rotary

S67: 2 pole 6 pos rotary

S68: 2 pole 6 pos rotary

S69: 2 pole 6 pos rotary

S70: 2 pole 6 pos rotary

S71: 2 pole 6 pos rotary

S72: 2 pole 6 pos rotary

S73: 2 pole 6 pos rotary

S74: 2 pole 6 pos rotary

S75: 2 pole 6 pos rotary

S76: 2 pole 6 pos rotary

S77: 2 pole 6 pos rotary

S78: 2 pole 6 pos rotary

S79: 2 pole 6 pos rotary

S80: 2 pole 6 pos rotary

S81: 2 pole 6 pos rotary

S82: 2 pole 6 pos rotary

S83: 2 pole 6 pos rotary

S84: 2 pole 6 pos rotary

S85: 2 pole 6 pos rotary

S86: 2 pole 6 pos rotary

S87: 2 pole 6 pos rotary

S88: 2 pole 6 pos rotary

S89: 2 pole 6 pos rotary

S90: 2 pole 6 pos rotary

S91: 2 pole 6 pos rotary

S92: 2 pole 6 pos rotary

S93: 2 pole 6 pos rotary

S94: 2 pole 6 pos rotary

S95: 2 pole 6 pos rotary

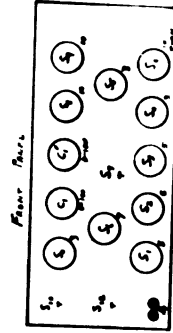
S96: 2 pole 6 pos rotary

S97: 2 pole 6 pos rotary

S98: 2 pole 6 pos rotary

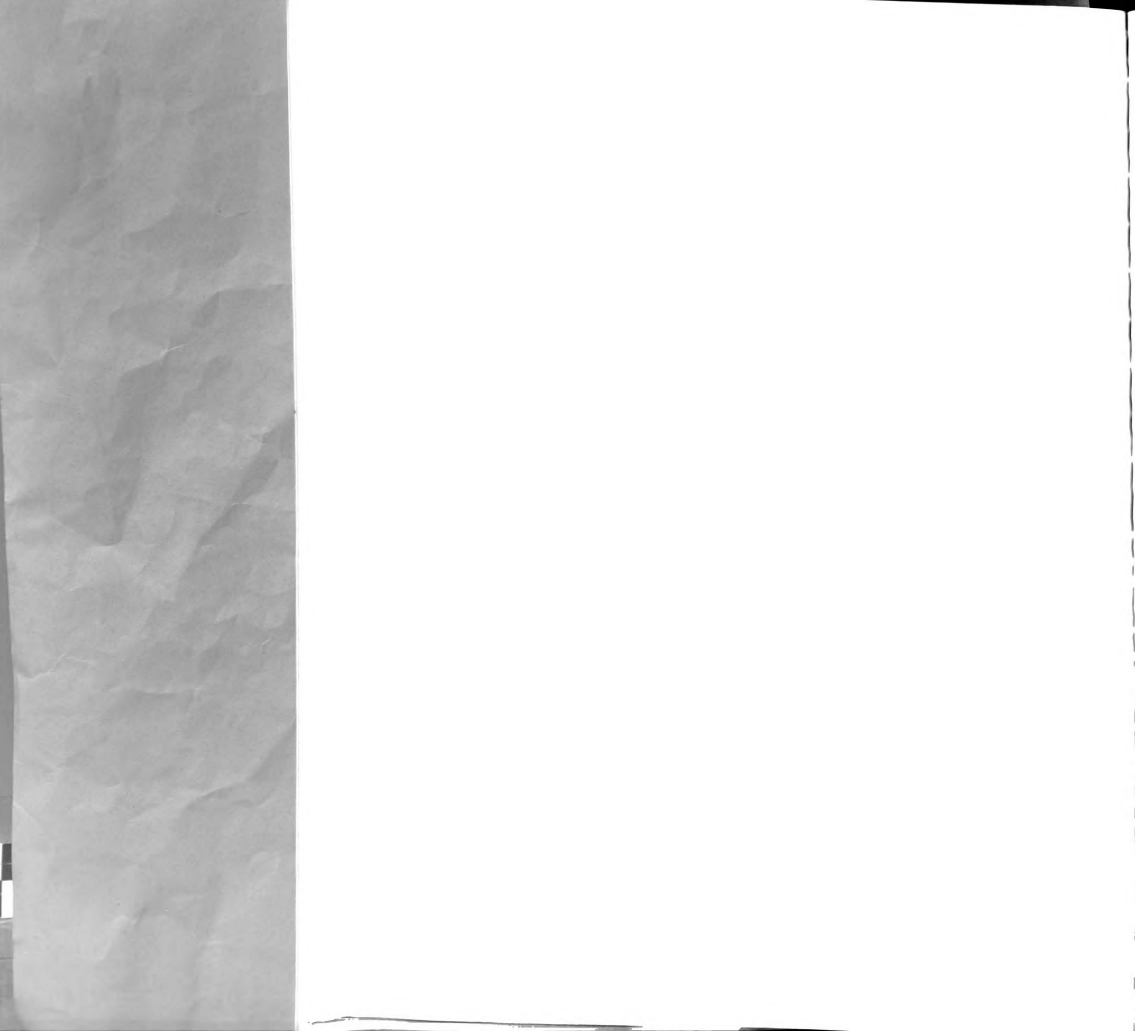
S99: 2 pole 6 pos rotary

S100: 2 pole 6 pos rotary



6745

Figure 13. Thermometer bridge



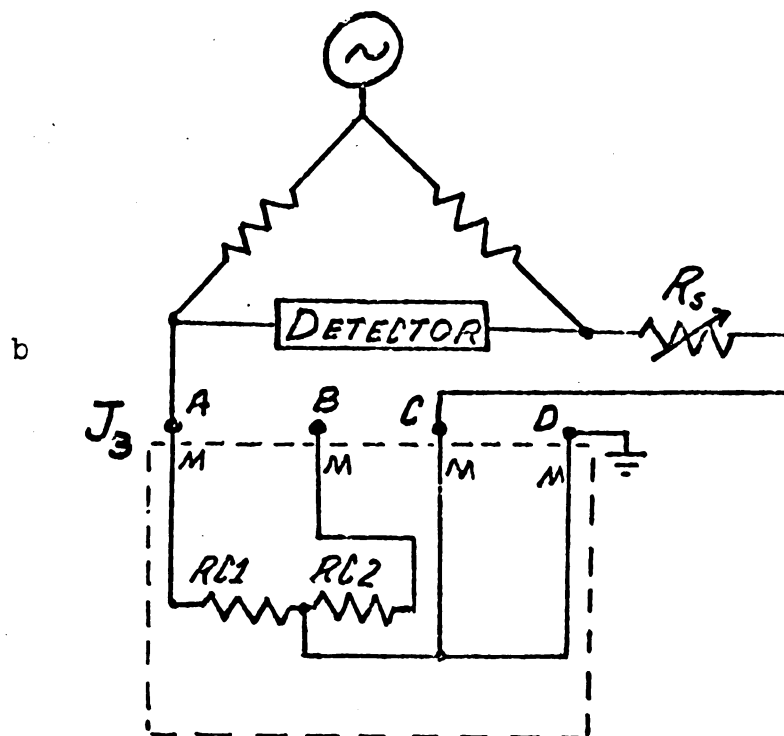
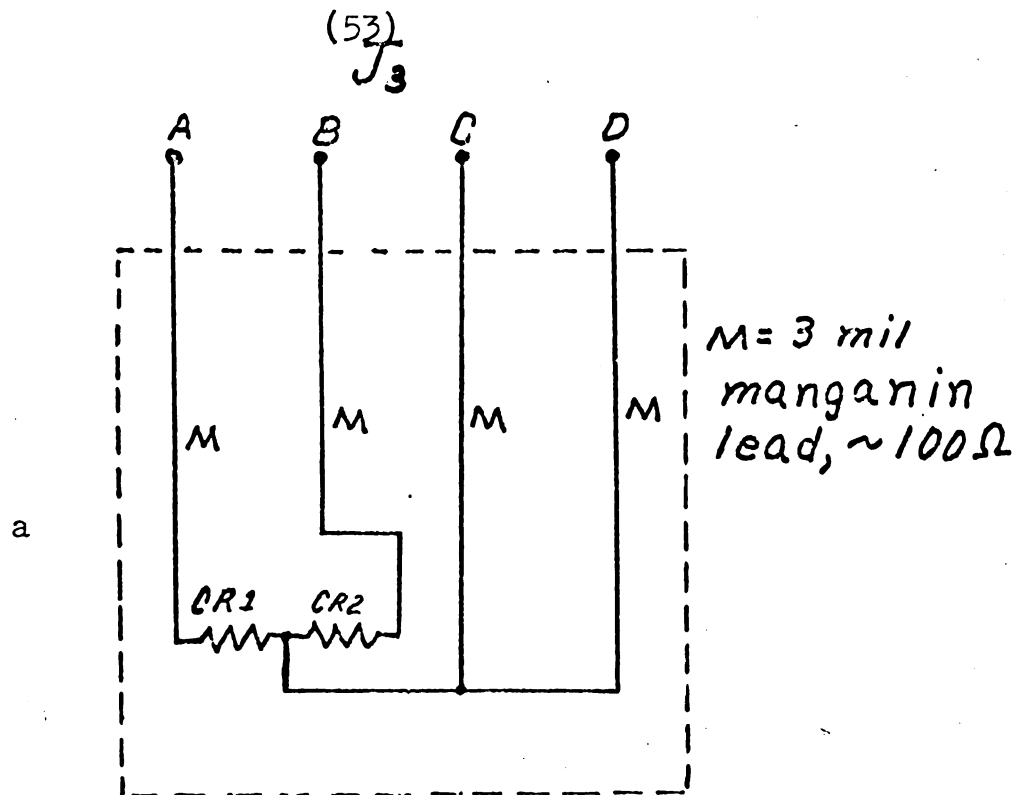


Figure 14. Bridge to cryostat leads

Steel structure of the bridge

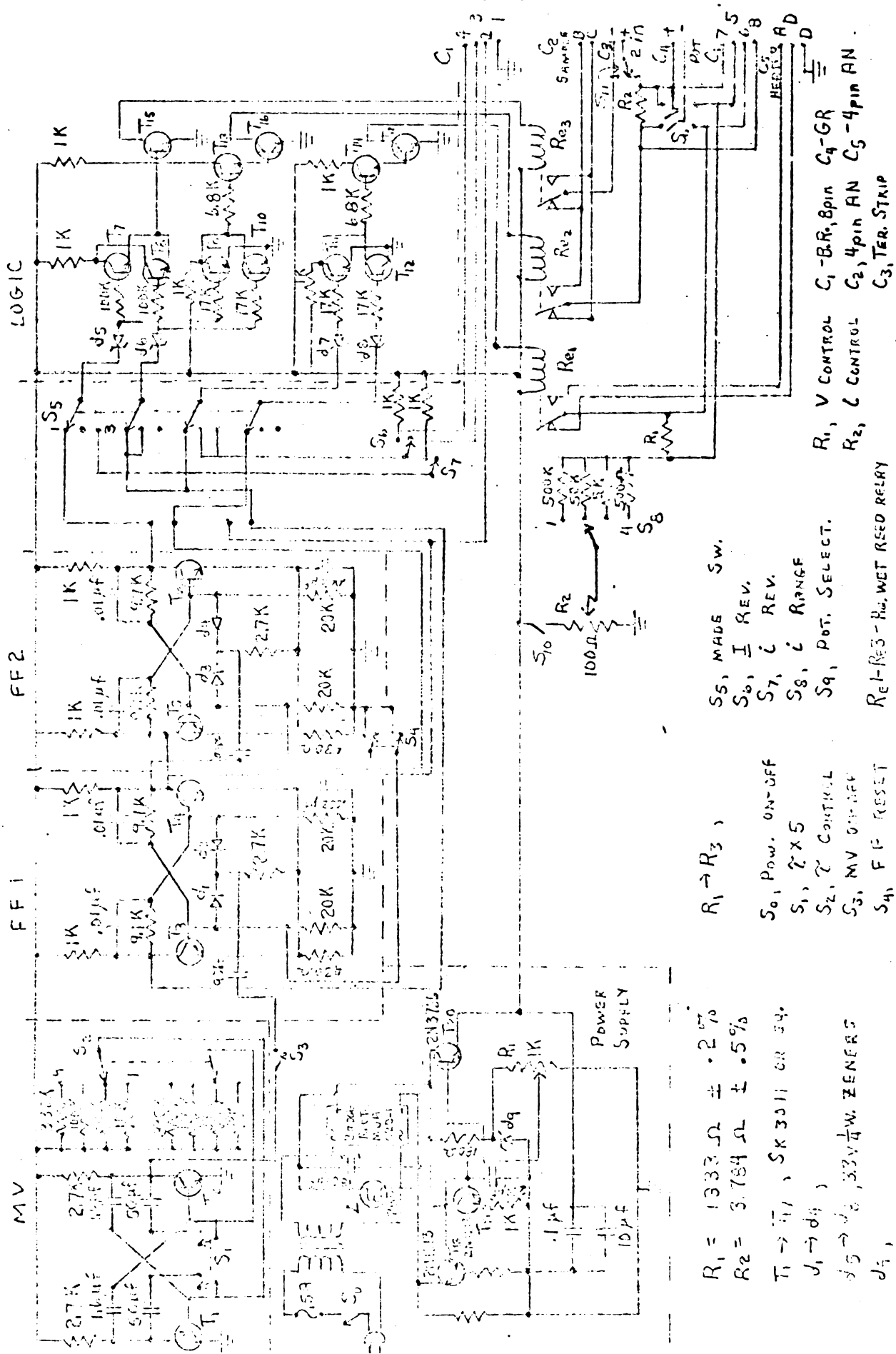


Figure 15. Control electronics

ATTORNEY'S OFFICE

1000 10th Street, N.W., Washington, D.C.

Telephone: 1000 10th Street, N.W., Washington, D.C.

1000 10th Street, N.W., Washington, D.C.

1000 10th Street, N.W., Washington, D.C.

1000 10th Street, N.W., Washington, D.C.

1000 10th Street, N.W., Washington, D.C.

1000 10th Street, N.W., Washington, D.C.

1000 10th Street, N.W., Washington, D.C.

1000 10th Street, N.W., Washington, D.C.

1000 10th Street, N.W., Washington, D.C.

1000 10th Street, N.W., Washington, D.C.

1000 10th Street, N.W., Washington, D.C.

1000 10th Street, N.W., Washington, D.C.

1000 10th Street, N.W., Washington, D.C.

1000 10th Street, N.W., Washington, D.C.

1000 10th Street, N.W., Washington, D.C.

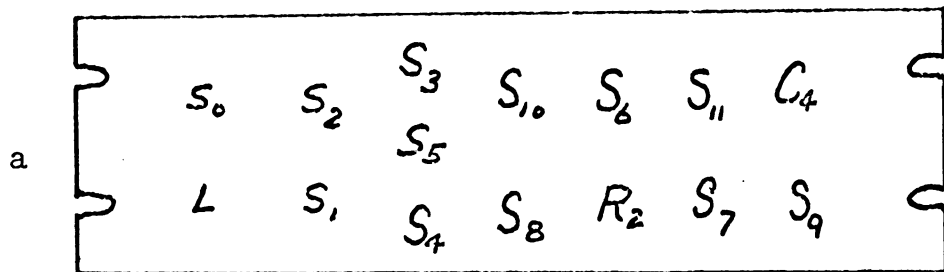
1000 10th Street, N.W., Washington, D.C.

1000 10th Street, N.W., Washington, D.C.

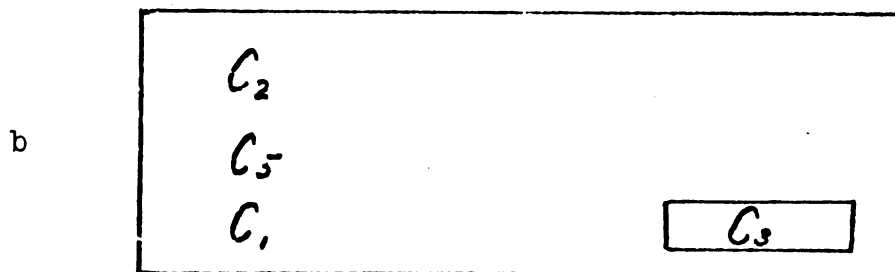
1000 10th Street, N.W., Washington, D.C.

1000 10th Street, N.W., Washington, D.C.

(55)



Front panel



Back panel

Figure 16. Control circuit switch positions.

(56)

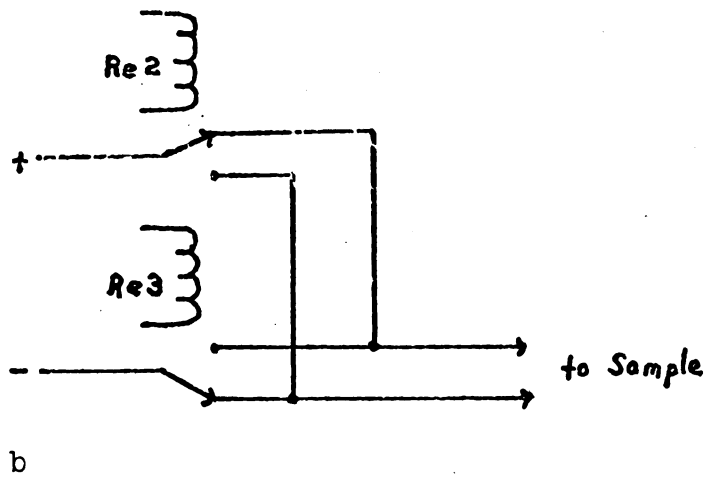
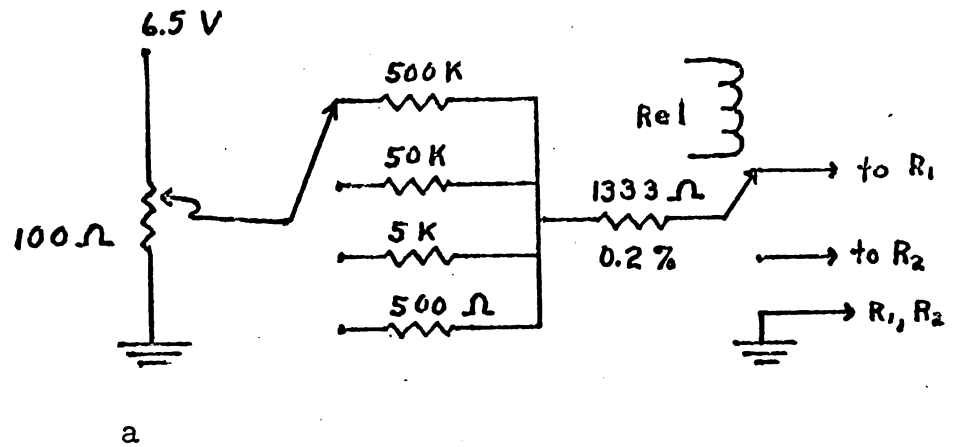


Figure 17. Current control sections

resistor R_2 , appearing across pins 7, 8 of C_1 . Either this voltage or that across R_1 (measuring heater current) could be monitored at the front panel G.R. connector C_4 .

Control relays Rel--Re3 were all Magnecraft type W133-MPCX2 mercury wetted reed relays with a response time of about two milliseconds.

The switch control was made to operate in three modes. The most complex, labeled mode 1, was a completely automated mode in which the sample and heater currents were switched in the sequence shown in figure 18a. Figure 18b is a block diagram of the circuit used to accomplish this. The various components of this network are identified in figure 15, in which the "logic" section includes the nand gates, the or gate, and the relay drivers. The multivibrator period τ could be selected from the following: .02, .08, .2, .35, 1.0, 4.0, 10, and 20 seconds.

In mode 2 the sample current was switched automatically in a square wave manner with a frequency of $1/2\tau$. The circuit used to accomplish this was just a variation of that used in mode 1 and is shown in figure 19. In this mode F.F.2 was removed from the circuit and Rel was under manual control. The lead marked "to C_1 , no. 2" was used as a reference sync., for it carried a 5 volt p.p. square wave of the same frequency as the sample current. The control would not operate in mode 1 if this lead was connected to an instrument. The capacitance across the input terminals of most instruments is enough to affect the triggering of F.F.2. This was remedied by placing a 10K or 100K resistor in series with the instrument, as indicated in figure 19b.

In mode 3 both currents were under manual control. The circuit used for this was the same in either case and is

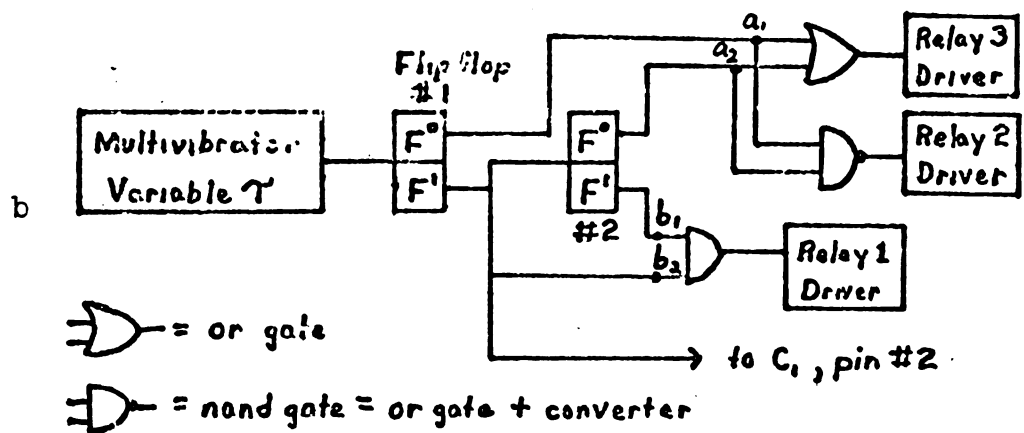
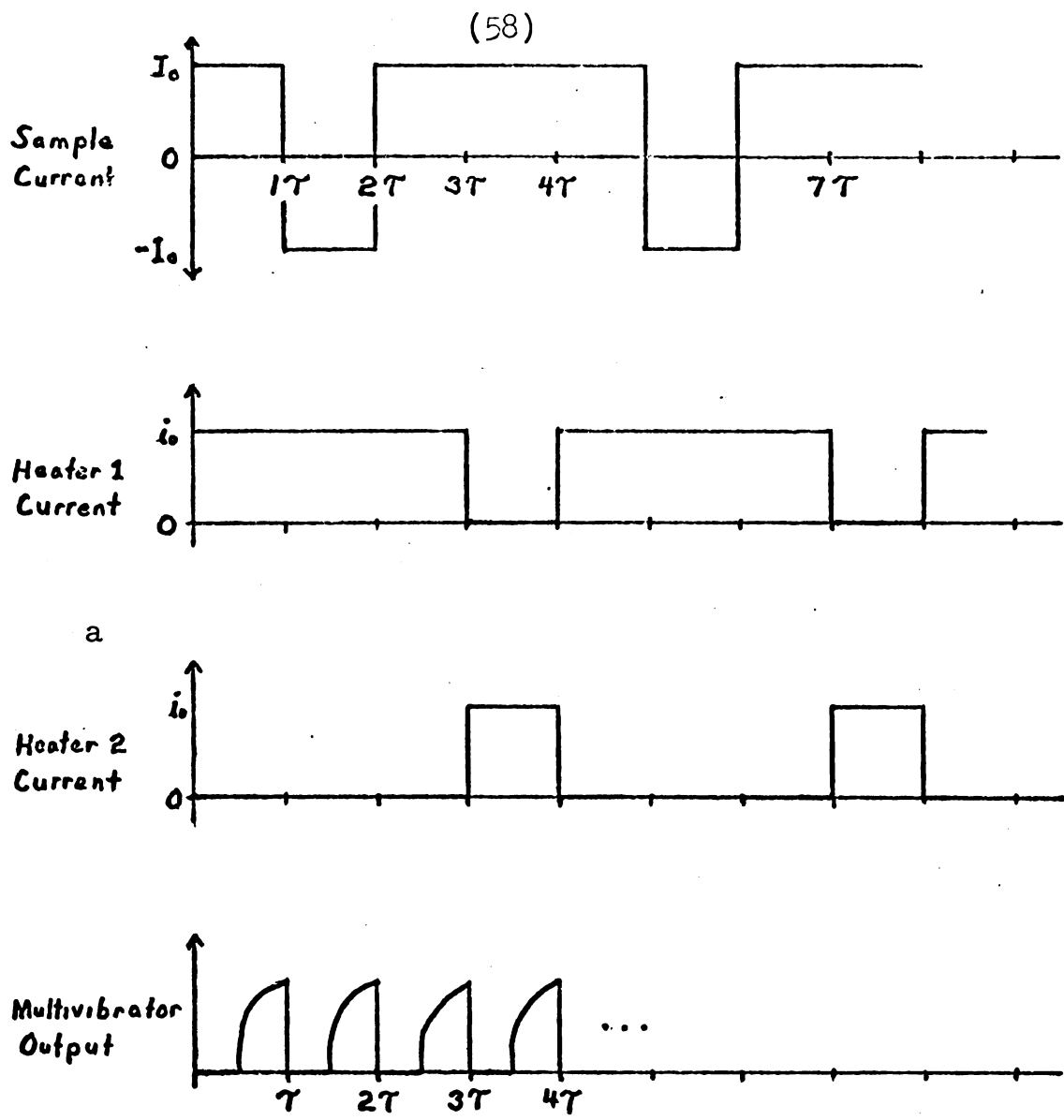


Figure 18. Mode 1 control logic

(59)

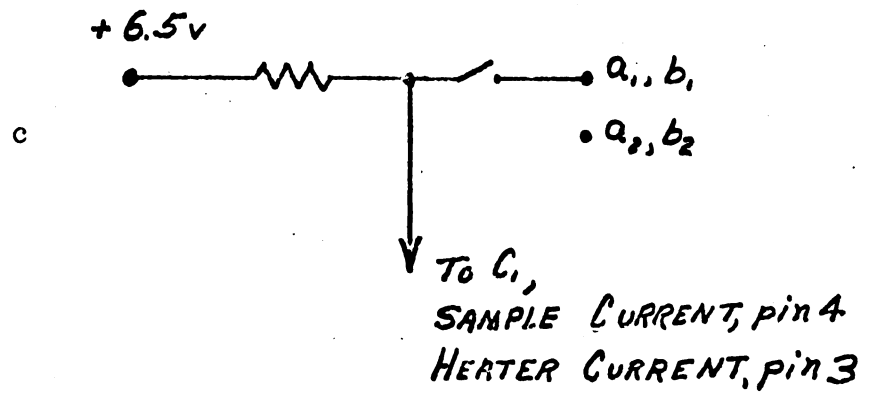
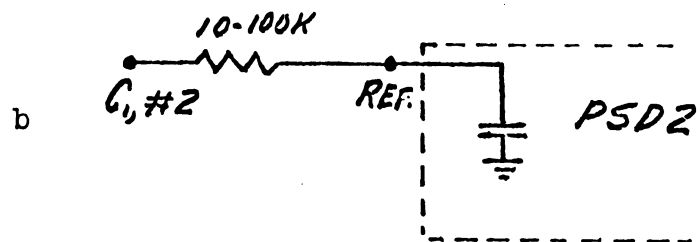
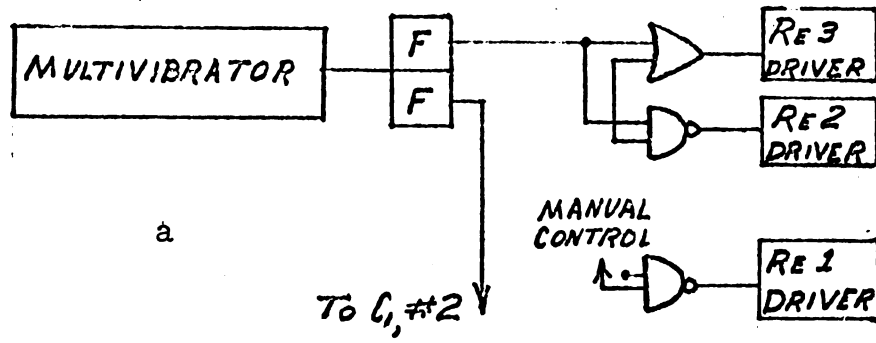


Figure 19. Mode 2 control logic

shown in figure 19c. Closing or opening the switch reversed the states of the appropriate relays. When the switch was closed the currents could still be switched by shorting the lead marked "to C_1 " to ground, which provided a method of external control.

D. Magnetic Field Electronics

The magnet used was a Harvey Wells 6 in. magnet capable of providing up to 22 kilogauss with a homogeneity of about .01 per cent in the central one inch cylinder. The magnet current was controlled by an adjustable internal reference voltage to which could be added an external reference signal.

The magnetic field sweep was a second generation model of a system originally designed by James Le Page.³² The output of a stationary pickup coil placed between the pole faces was compared with a reference voltage, the difference amplified and integrated and used as a reference for the magnet power supply. By adjusting the amplifier gain it was possible to keep the field sweep rate proportional to the reference to within about one percent.

In the unregulated mode the pickup coil was not used; the reference was simply integrated so that the magnet current, rather than the field was controlled.

The reference for a constant sweep rate was a constant voltage, supplied internally. For any other sweep form one would have to supply a reference external to the sweep control.

The primary difficulty encountered with this circuit was that the system would oscillate unless the reference voltage was increased slowly from zero. This necessitated

(61)

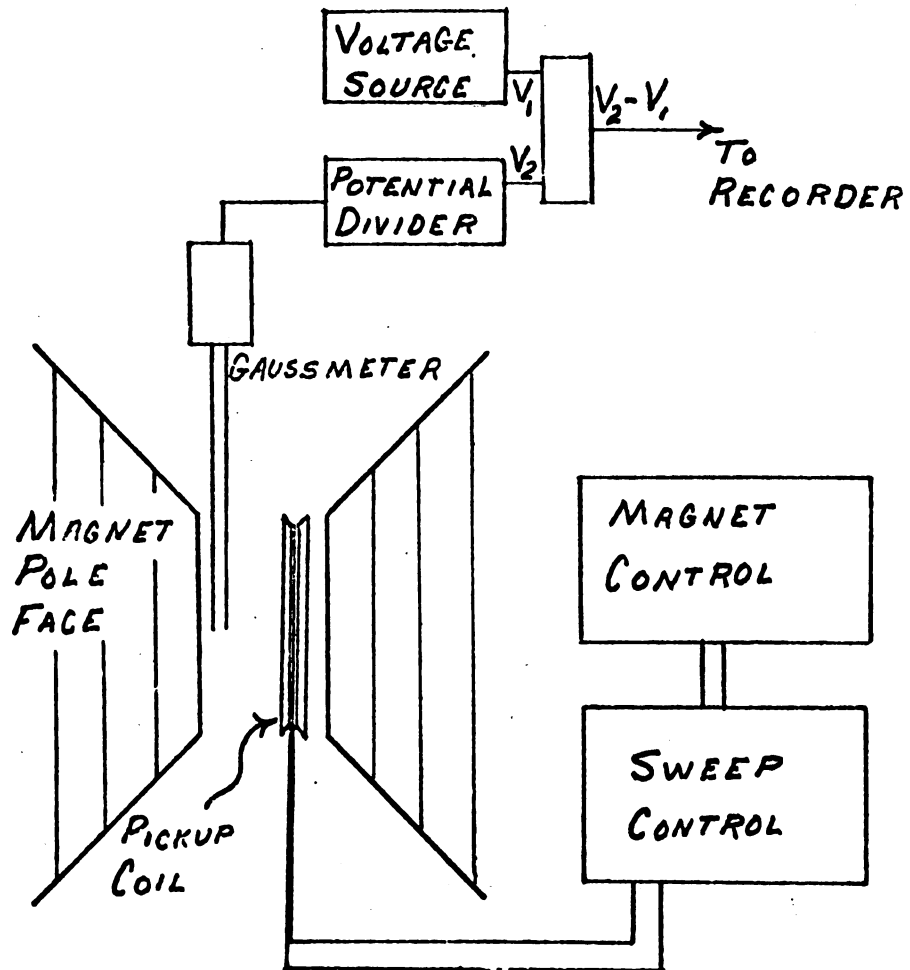


Figure 21. Magnetic field electronics

cranking the sweep rate potentiometer to zero and back up whenever a new sweep was started. It could be corrected with an appropriately designed, RC controlled transistor switch at the input to the sweep rate potentiometer.

The magnetic field was measured with a Rawson rotating coil gaussmeter which had been calibrated against an NMR probe. The difference between the potential divided output and a constant voltage source was plotted by the strip chart recorder described in the preceding section. The source could be changed in steps equivalent to 2.26 kilogauss. Due to loading of the Rawson meter in the network the following equation was used to calculate the magnetic field:

$$H = 2.26 \text{ Kilogauss } [N + x(1.03)] \quad (114)$$

N = number of (100 mv) steps applied from the constant voltage source,

x = position of the pen tracing, in fractions of full scale (100 mv).

E. Temperature Control and Measurement

Temperatures below 4.2°K were obtained in the standard manner by pumping on the liquid helium bath. The pressure above the bath was controlled through the use of a "Walker manostat" and measured with either a manometer or a McLeod gauge. The temperature of the bath was then determined using the 1958 scale of the liquid Helium vapor pressure. After the carbon resistors had been calibrated against the vapor pressure, they were used as the basic thermometers.

VIII. Operation, Data Reduction

A. Introduction

The data desired in this study were a set of values for the Peltier (equivalent to the Seebeck) coefficient as a function of magnetic field strength and direction. Generally, the approach employed was to change the magnetic field continuously while monitoring the Peltier heat.

B. Point by Point Methods

This method of measurement did not require the second phase sensitive detector in figure 12; the output from PSD1 was fed directly to the recorder. If operated in switching mode 1 the recorder trace was similar to the one shown in figure 23, the amplitude of the square pulses representing (δT_{\parallel}) alternating with (δT_r). By comparing a δT_{\parallel} to the two δT_r 's flanking it, a value of the Peltier coefficient was obtained. One could carry out this operation while varying the field to obtain results but the calculations would be overwhelming. An improvement was affected by doing all of the computational work on a computer but as the charts still had to be read by hand the work was still so great as to make the method impractical. It was hoped that a digital recording system would be completed in time to use it in this application but it was not.

Since the thermal resistance of the system showed little field dependence other than a monotonic increase it was possible to use mode 2, switching the sample current only, to obtain meaningful data. In this mode the system had to be calibrated by obtaining δT_r as a function of field for every temperature used, although the mesh of points used for this measurement was much more coarse than that necessary for

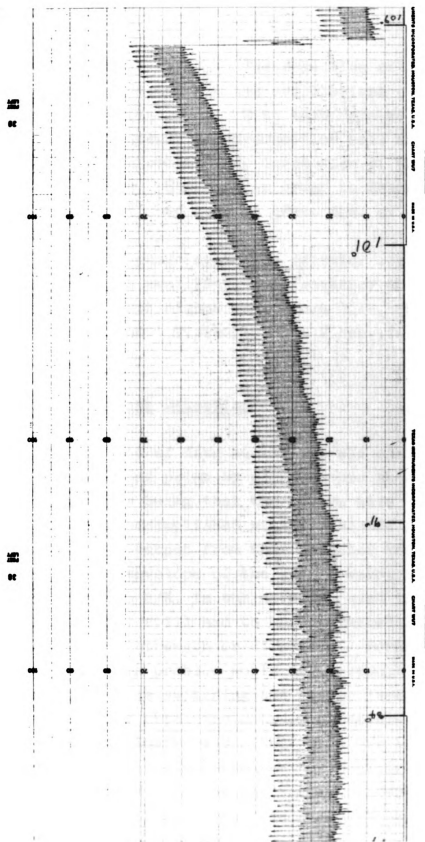


Figure 23. Typical recorder trace, mode 1,
a rotation

the measurements of δT_{Π} . The reduction of such data was still quite tedious, but the oscillations could be seen directly; see figure 24. With such data we obtained de Haas van Alphen frequency measurements as well as a limited amount of amplitude information by inspection of the envelope of the square wave. However, in order to measure harmonic content we still had to do a great deal of manual data handling.

Since the phase sensitive detector used had a Q of 25 in the input amplifier, the frequency at which it was operated was kept higher than about $25/\tau$, where τ is the switching period. Typically, $\tau \approx 2$ sec., $f = 23$ cps.

C. Continuous Detection

This method of data acquisition was basically quite similar to the second point by point method described above, the only difference being that the square wave form was detected. This was accomplished with the second phase sensitive detector. The output from this detector was, of course, the amplified envelope of the square wave, and was directly proportional to Π/K , in the notation used in section VI, B. The scale ($1/K$) still had to be determined as a function of magnetic field strength or direction. Perhaps the best approach to this problem would be to repeat the magnetic field sweep while switching the heater current at the same frequency, thus obtaining a trace representing the scale factor. The primary reason that this was not done was that the required switching mode was not provided in the control box. The method would assume that the thermal time constants associated with the Peltier and calibrating heats were

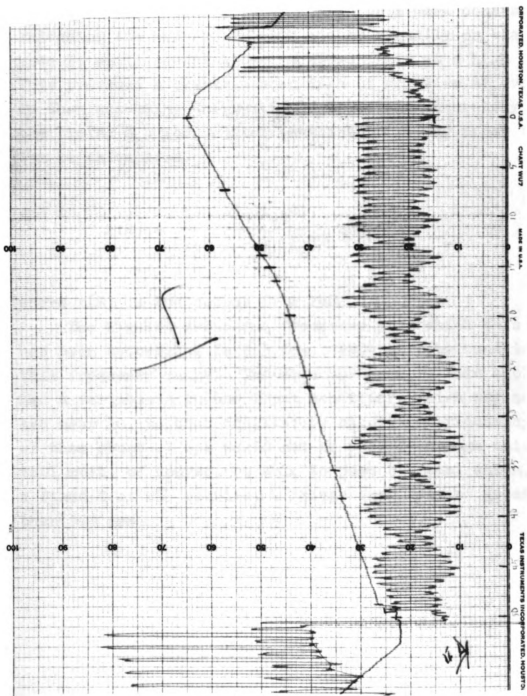


Figure 24. Typical recorder trace, mode 2, a sweep, diagonal line records field strength

identical, or else very small.

The calibrating method used in this work consisted of switching the heater current, either manually or via control mode 1, while sweeping the magnetic field at a high rate. This provided a rather coarse mesh of relative δT_r values. By then measuring the Peltier coefficient accurately at one field, H_o , the Peltier coefficient at any other field can be calculated.

$$\Pi(H) = \left[\frac{\Pi(H_o) \delta T_r(H)}{x(H_o) \delta T_r(H_o)} \right] x(H) \quad (115)$$

where $x(H)$ is the output from PSD2.

The highest switching frequency with which this method has been successful is 2.5 cps. PSD2 must be tunable in this frequency range. The detector used in this application had a variable Q in the input amplifier, which was normally set near 10, so that oscillatory signals of frequency greater than about .1 cps would not be passed through this stage. PSD1 must, of course, be able to pass 2.5 cps, which, with a fixed Q of 25, required a bridge frequency of greater than 100 cps.

IX. Samples

Two zinc samples were used in this work. The preparation and characteristics are discussed in this section.

A. Zn 1

The first sample was cut from a slug supplied by Metals Research Ltd. with a Servomet spark cutter. The orientation of the cylinder axis was within a few degrees of the [0001] axis. The resistance ratio ($\rho_{300^{\circ}\text{K}}/\rho_{4.2^{\circ}\text{K}}$) of this sample was measured to be about 15,000.

B. Zn 2

The second sample was oriented with the [0001] axis within a few degrees of perpendicular to the cylinder axis. The resistance ratio was 3800. This sample was cut from a rod grown in an optical zone refiner built and described by J. C. Abele.³³

IX. Results

A. Zinc Fermi Surface

The Fermi surface of zinc has been studied with a determination applied to few metals. As a consequence the Fermi surface dimensions, effective masses, and magnetic breakdown fields are known in some detail.³⁴⁻⁴⁰ Figure 25 is a sketch of the results of this work. In spite of an apparent complexity the Fermi surface is very nearly a one O.P.W. surface, although deviations are relatively large for some of the very small sections. The oscillations observed in this work were due to the α , β and γ orbits indicated in the figure.

B. Data Interpretation

The frequency of oscillatory terms in any measurement is a function of the field direction \hat{h} . Thus,

$$\mathfrak{S} = S_1(H,T) \sin\left[\frac{f(\hat{h})}{H} + \frac{\pi}{2}\right]. \quad (116)$$

One may observe this effect by monitoring the Seebeck coefficient while varying either the field strength or the direction. Obviously either method will provide amplitude data. However, the frequency information that can be obtained from the two methods is quite different. Sweeping the field strength in a fixed direction provides a frequency in that direction

(71)

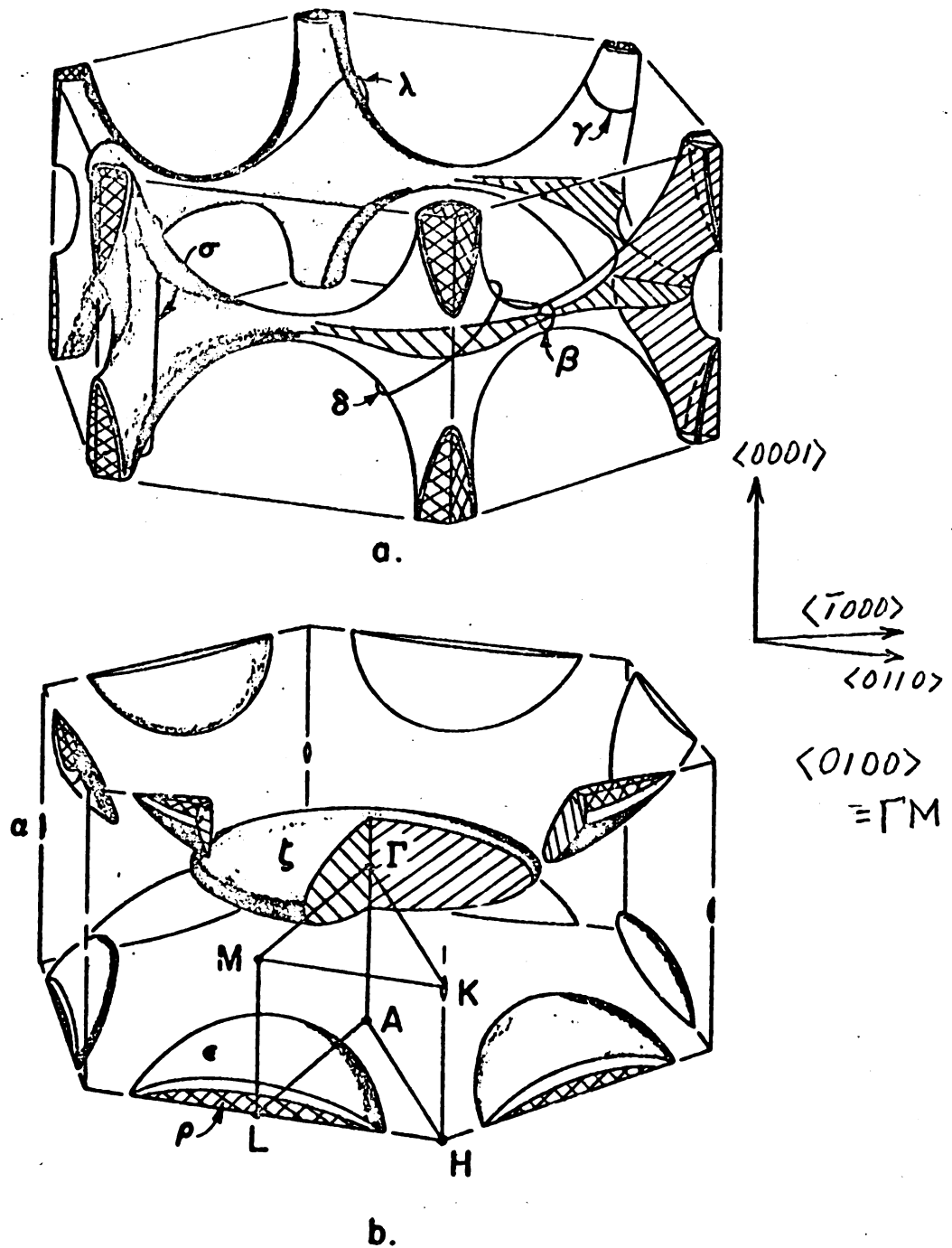


Figure 25 (after Gibbons and Falicov³⁴)
The Fermi surface of zinc

while from rotational data one can extract $|df/dh|$, i.e. the change of frequency with field direction. A combination of the two methods can be used to provide a detailed picture of the absolute frequency as a function of field direction.

C. Zn 1

In this crystal the current was along the $\langle 0001 \rangle$ axis, the magnetic field restricted to the basal plane. Due to the six fold axis along $\langle 0001 \rangle$ one need make measurements over only sixty degrees of field angle.

The only oscillations that could be observed in this crystal were those due to the monster neck (β) orbits, which could be observed for all field angles. Some of the data are shown in figure 26. A pronounced beating is evident for the last two angles, which are near the $\langle 1000 \rangle$ axis. An inspection of figure 25 will serve to assure one that this can be expected, for near the $\langle 1000 \rangle$ there will be two sets of β orbits of nearly the same cross sectional area. The frequencies of these oscillations were measured with sufficient accuracy to identify the $\langle 0110 \rangle$ axes of the crystal. As we were most interested in the amplitude of the oscillations we picked one of these as the field direction for most of the study. Such a choice both maximized the amplitude and minimized the beating.

Figure 27 shows the measured amplitude at 21 kilogauss as a function of temperature. Although the error bars on the data at 4.2° are rather large, the oscillations are clearly evident. It should be noted that we have plotted the total amplitude here, rather than the amplitude of the

(73)

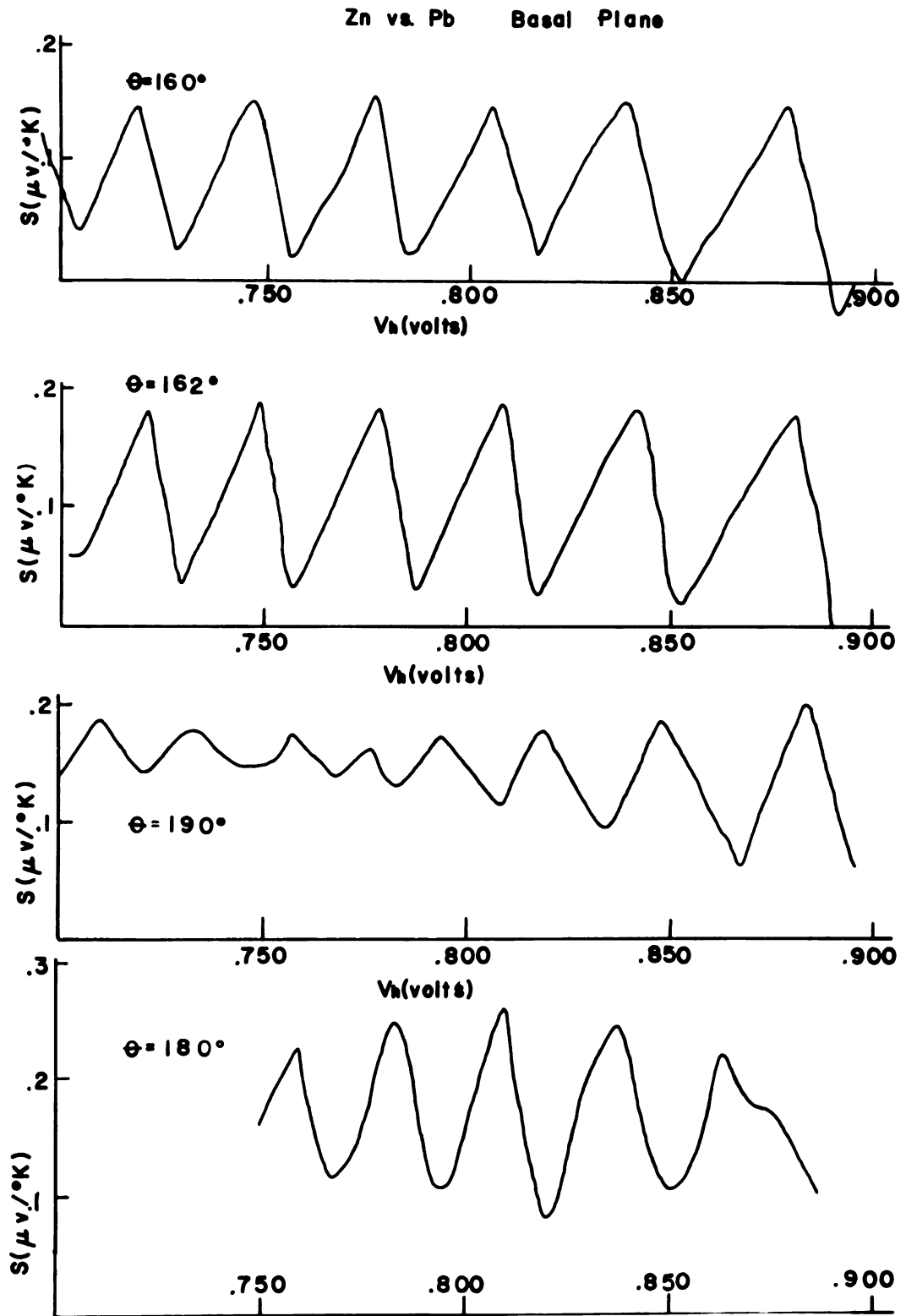


Figure 26. β oscillations in Zn 1

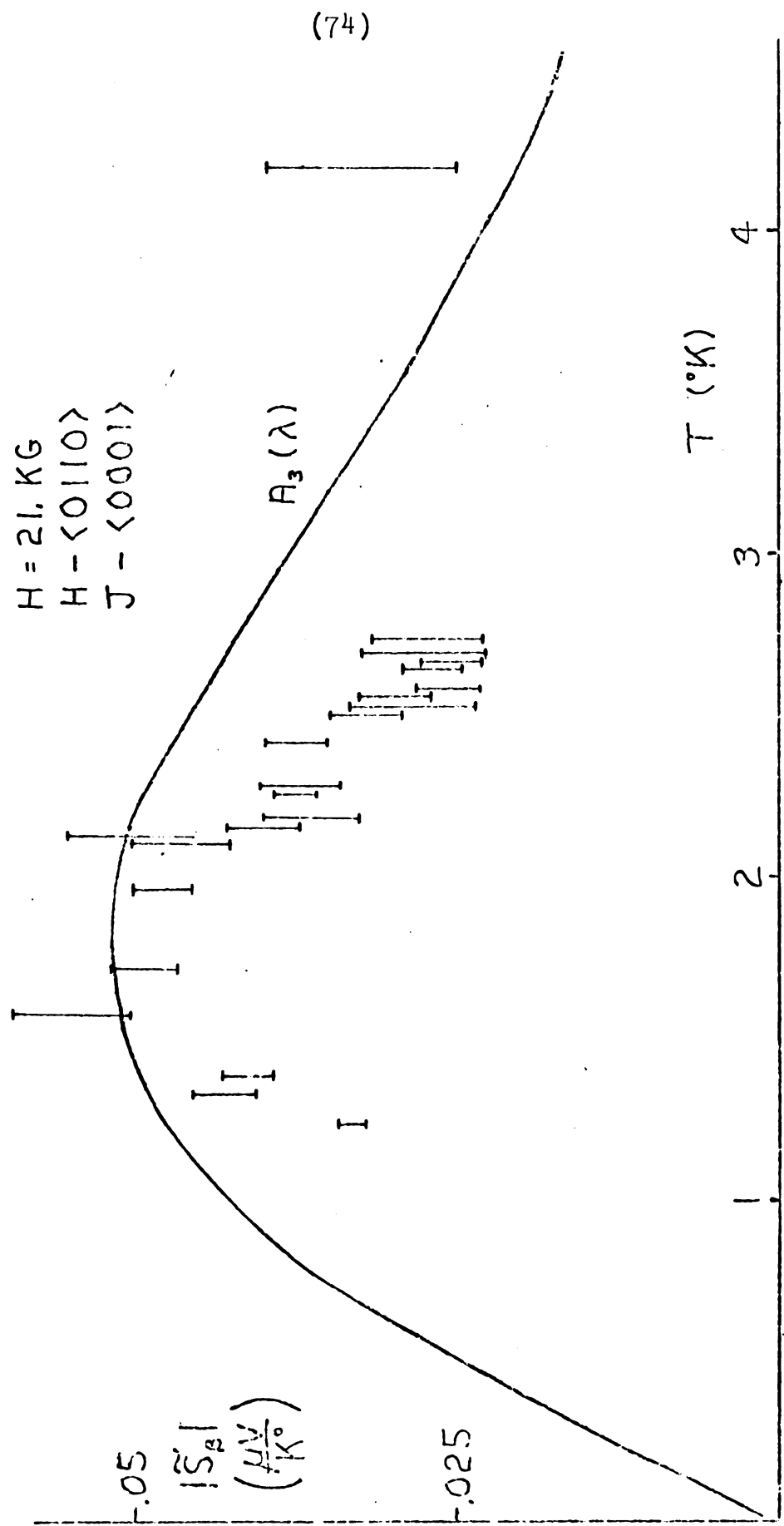


Figure 27. $| \tilde{S}_\beta |$ vs. T, Zn 1

fundamental component. That the two are quite different is evident in figure 28, which shows the wave shapes at two temperatures. A plot of the oscillation amplitudes as a function of field strength is shown in figure 29. Such data were collected at only one temperature.

Figure 30 shows the dependence of the background Seebeck coefficient as a function of field direction at 1.32°K . As this pattern was repeated every sixty degrees it was a consequence of the crystalline structure rather than some peculiarity in the physical arrangement. If one subtracts the Seebeck coefficient of Pb, the value of S at $\langle 0110 \rangle$ is $0 \pm .05 \mu\text{v/K}^{\circ}$.

The temperature dependence of the anisotropy of S is shown in figure 31.

D. Zn₂

In this crystal the current flowed along the $\langle 1000 \rangle$ axis. The magnetic field could be applied along any vector in the (1000) plane, i.e. the plane defined by the $\langle 0001 \rangle$ and $\langle 0110 \rangle$ axes.

Figure 32 is a diagram of the measured Seebeck coefficient as a function of field direction at 19.6 kilogauss. The proper inversion symmetry is observed about the $\langle 0001 \rangle$ and $\langle 0110 \rangle$ directions except for a ten per cent discrepancy about twenty degrees from the $\langle 0001 \rangle$ axis. The oscillations extending to 50° on either side of $\langle 0110 \rangle$ can be associated with the β orbits while those centered 35° from the $\langle 0001 \rangle$ arise from the monster arm (γ) orbits. The background Seebeck coefficient is almost constant except near the $\langle 0110 \rangle$ axis where we find a pronounced dip.

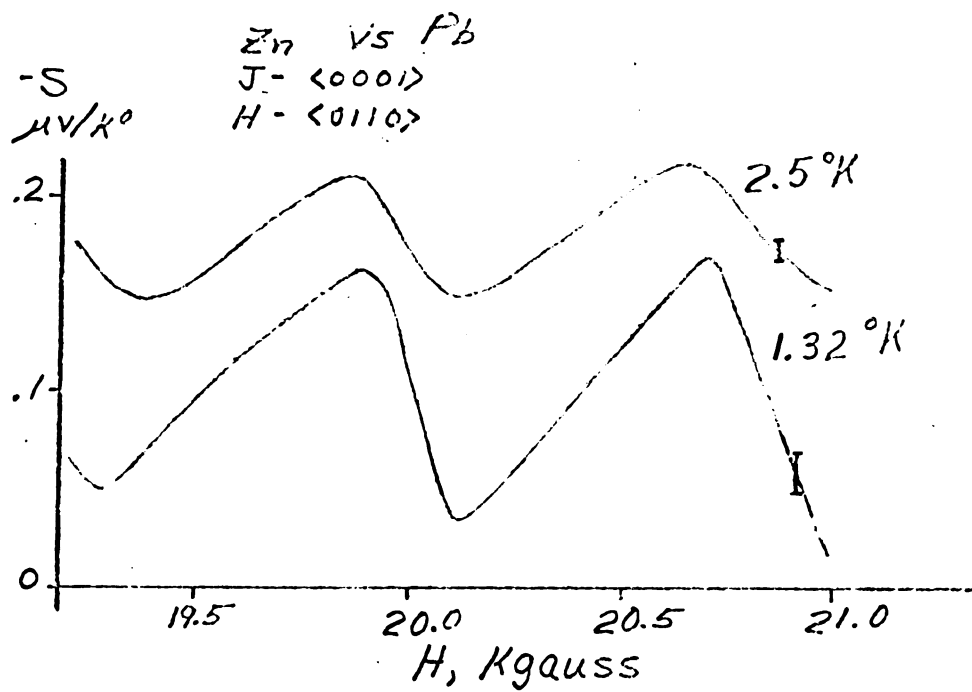


Figure 28. Thermal damping of the β oscillations

(77)

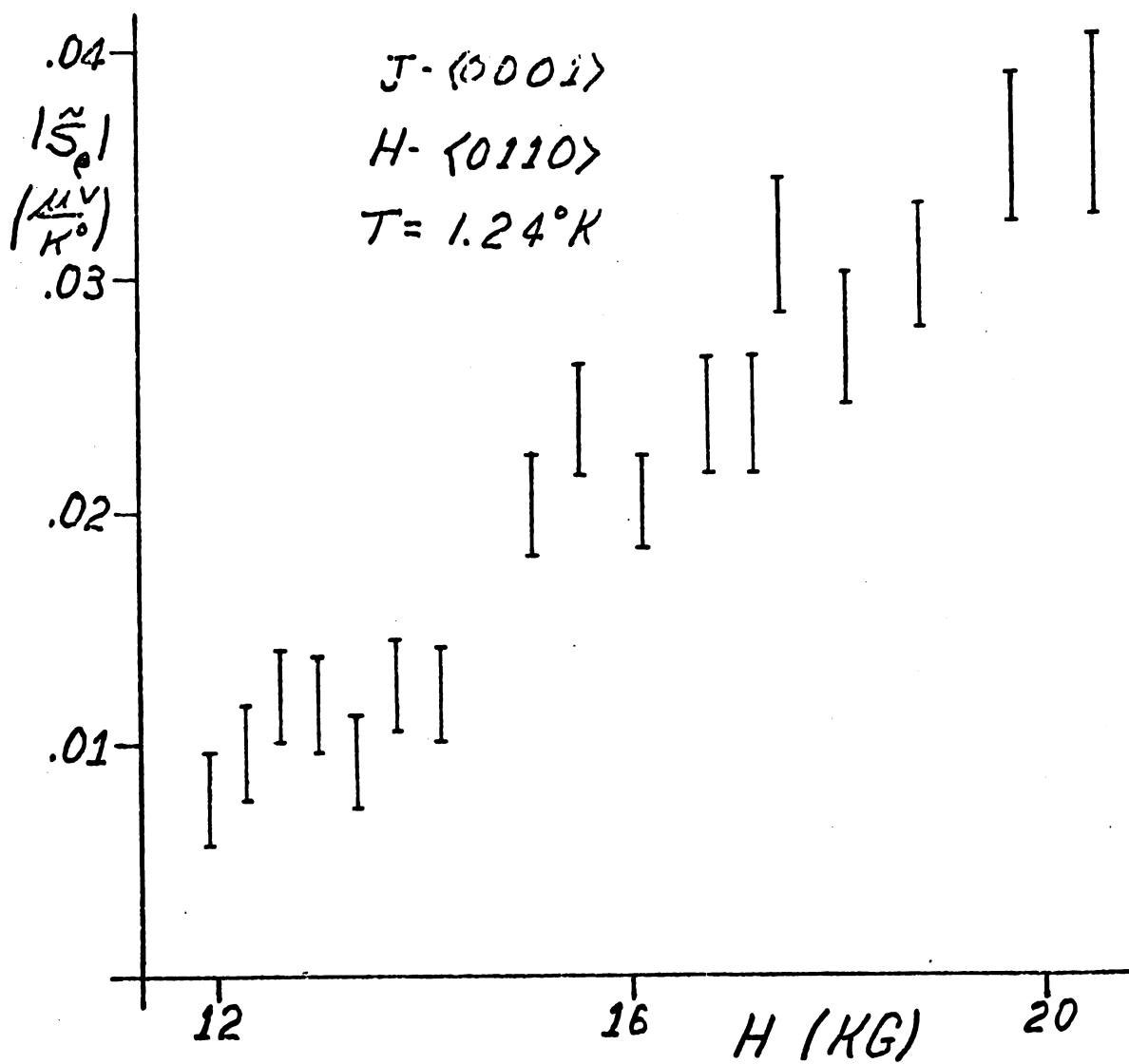


Figure 29. $|S_H|$ vs. H, Zn 1

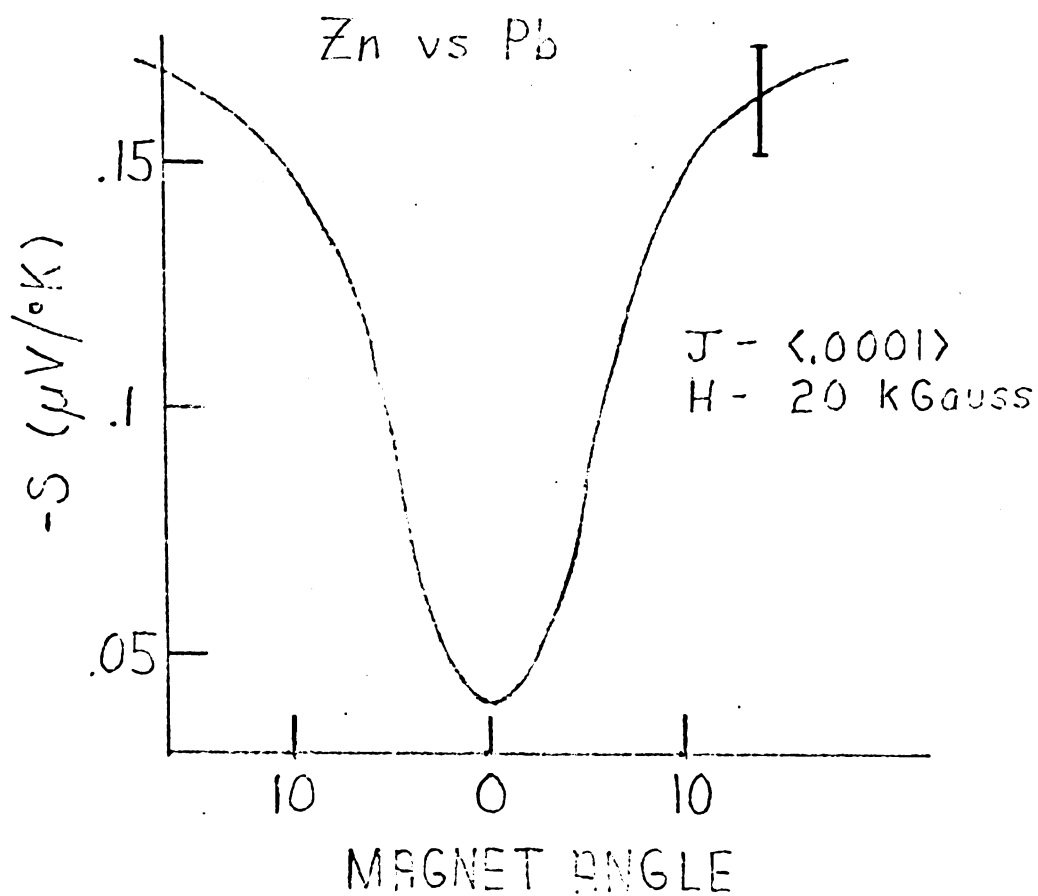


Figure 30. \bar{S} vs. θ , Zn 1

\vec{J} ALONG
 $\langle 0001 \rangle$

(79)

\vec{H} ALONG

$\uparrow - \langle 1000 \rangle$

$\downarrow - \langle 0110 \rangle$

$H = 21 \text{ KG}$

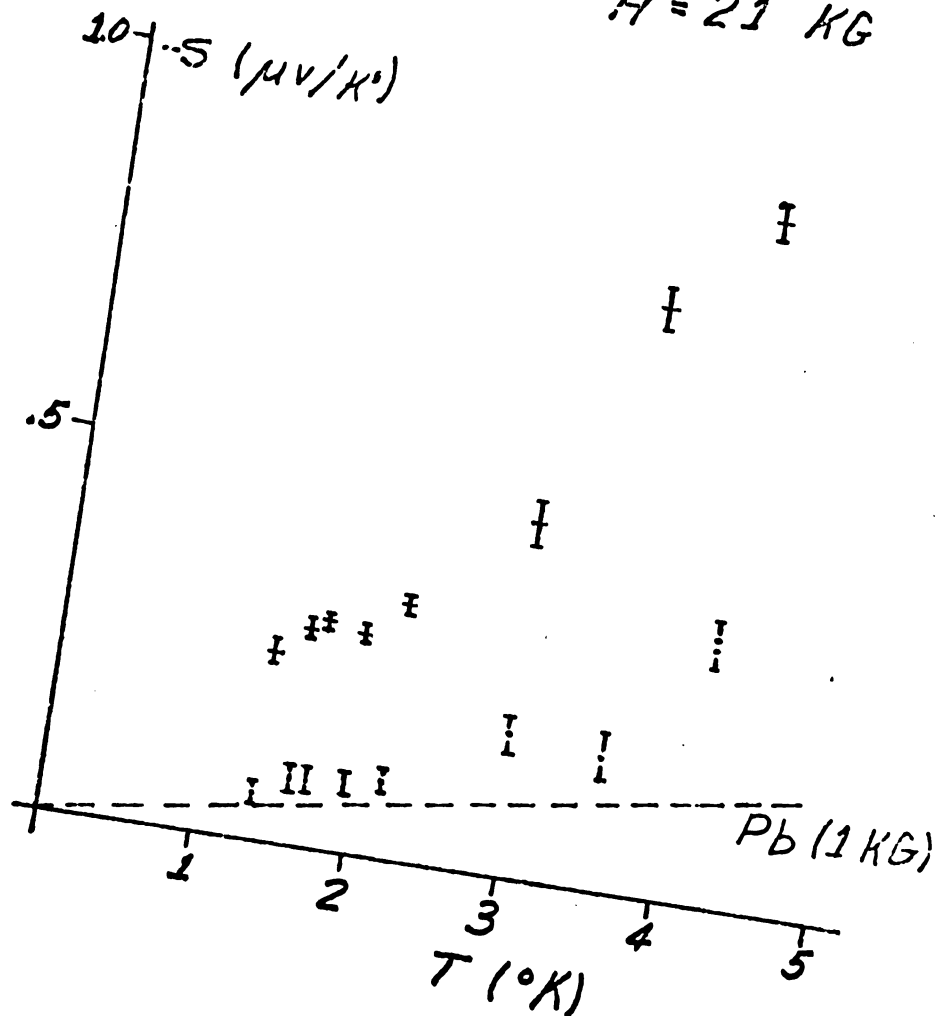


Figure 31. \bar{S} vs. T , Zn 1

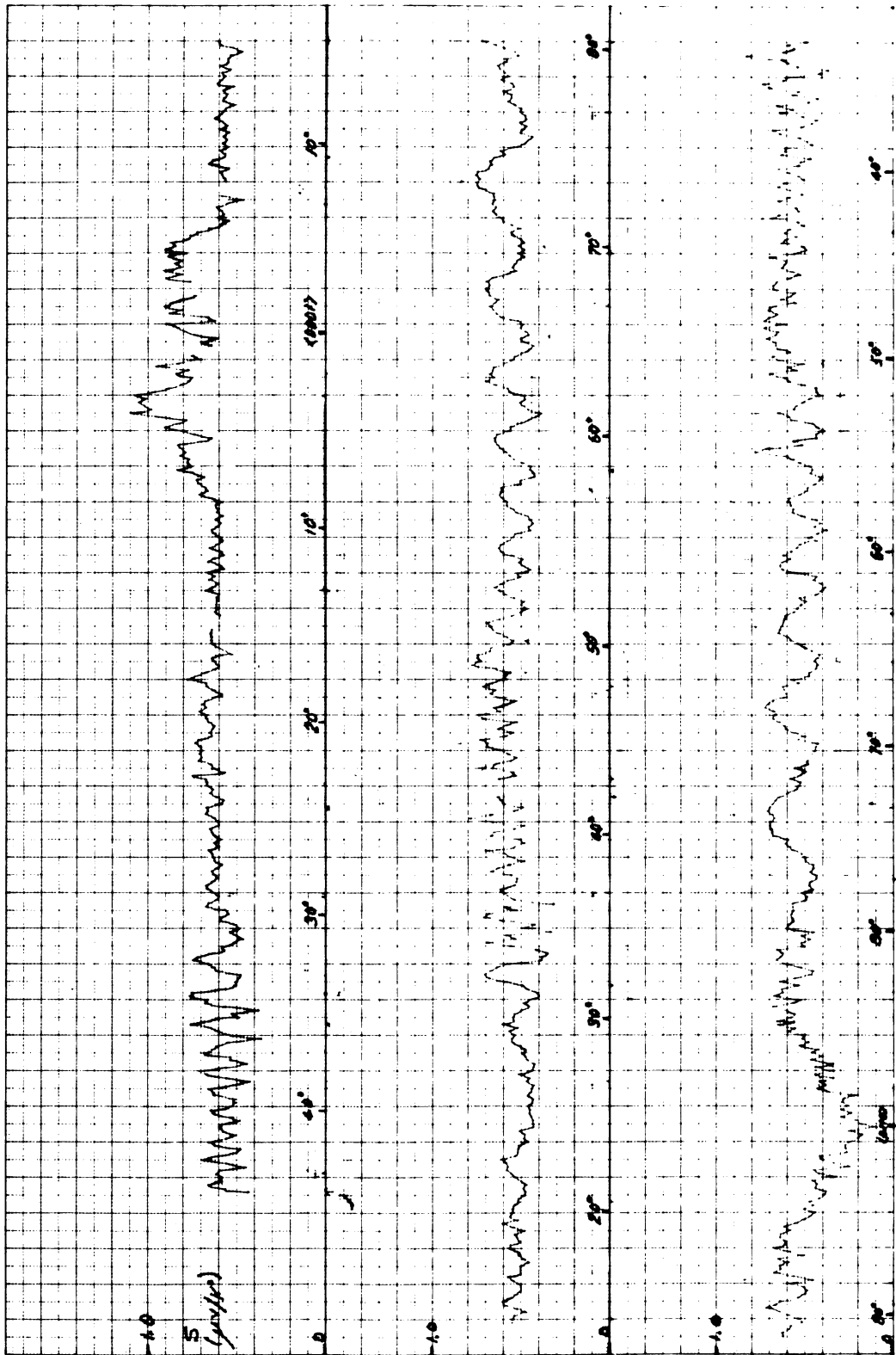


Figure 32. Field rotation, Zn 2

The α , β and γ oscillations were all observed in this crystal. We shall discuss them in that order.

1. The α Oscillations

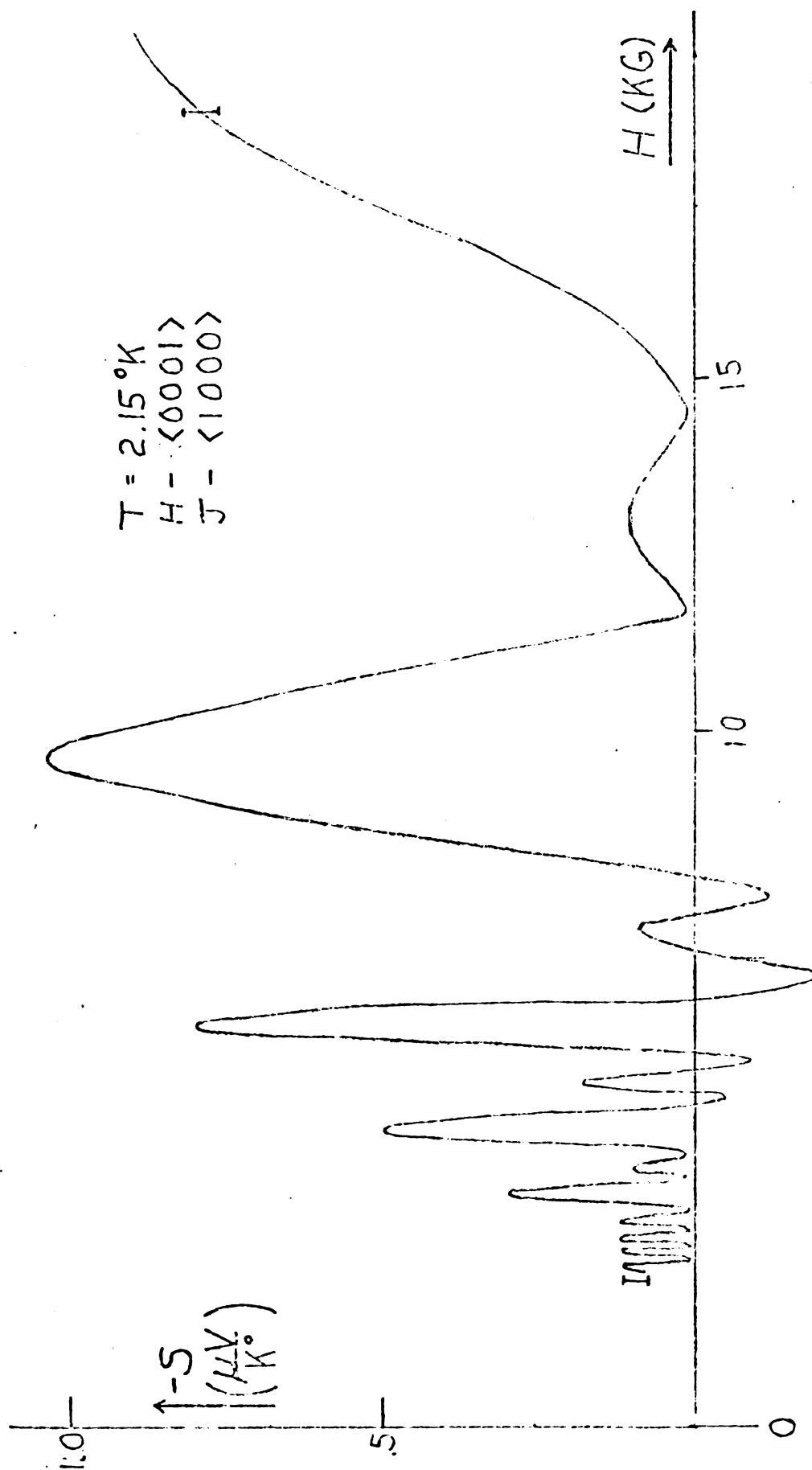
The needle (α) oscillations had the lowest frequency observed, about 1.6×10^4 gauss, as well as the largest amplitude. A plot of typical data is shown in figure 33. The oscillation amplitude was a sensitive function of field angle as can be seen in figure 34. Figure 35 shows the amplitude as a function of temperature. The apparently high values at the lowest temperature may well be due to an error in recording the temperature.

The secondary peaks observed in the oscillatory Seebeck coefficient are due to spin splitting of the Landau levels. This effect has been quite well documented³⁵ and will not be discussed here.

The needle oscillations have been observed in the Seebeck coefficient by Grenier et. al.⁴⁰ Their results agree with ours where the two overlap.

2. Monster Neck (β) Oscillations

The β oscillations were observed over almost a 100° range of field angles centered about the $\langle 0110 \rangle$ axis. A single rather accurate frequency determination 33° from $\langle 0110 \rangle$ coupled with the rotational data of figure 32 was sufficient to obtain the frequency vs field direction plot of figure 36. The amplitude at 19.6 kilogauss is plotted vs the field direction in figure 37. Due to the obvious

Figure 33. α oscillations, Zn 2

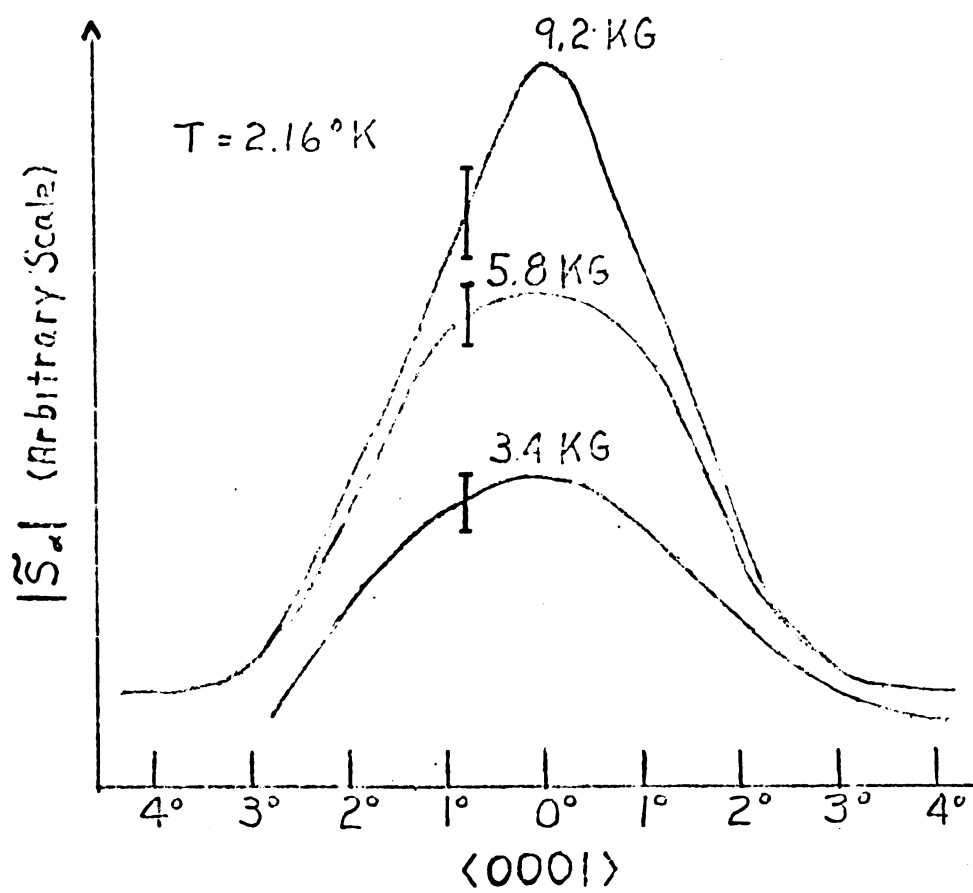
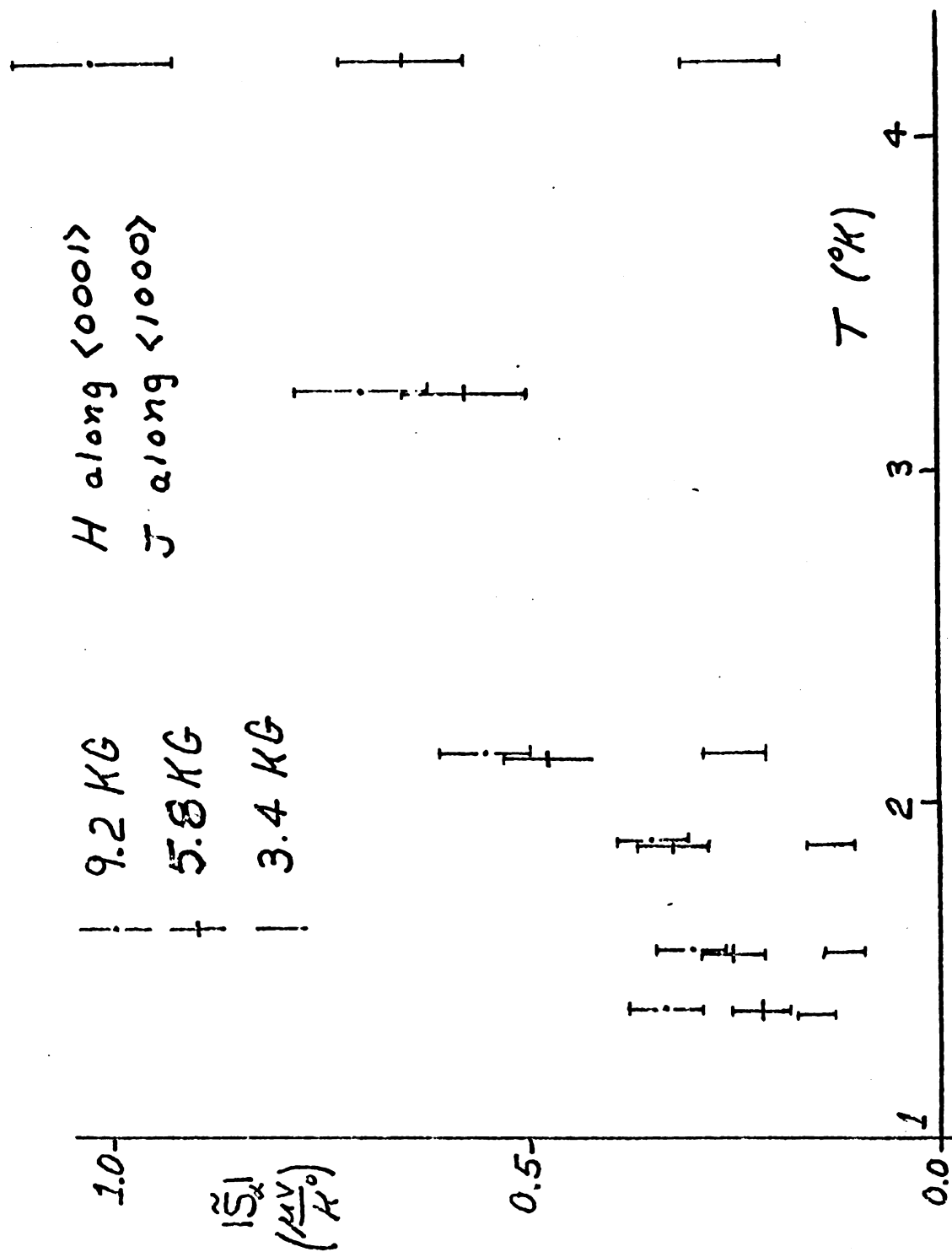
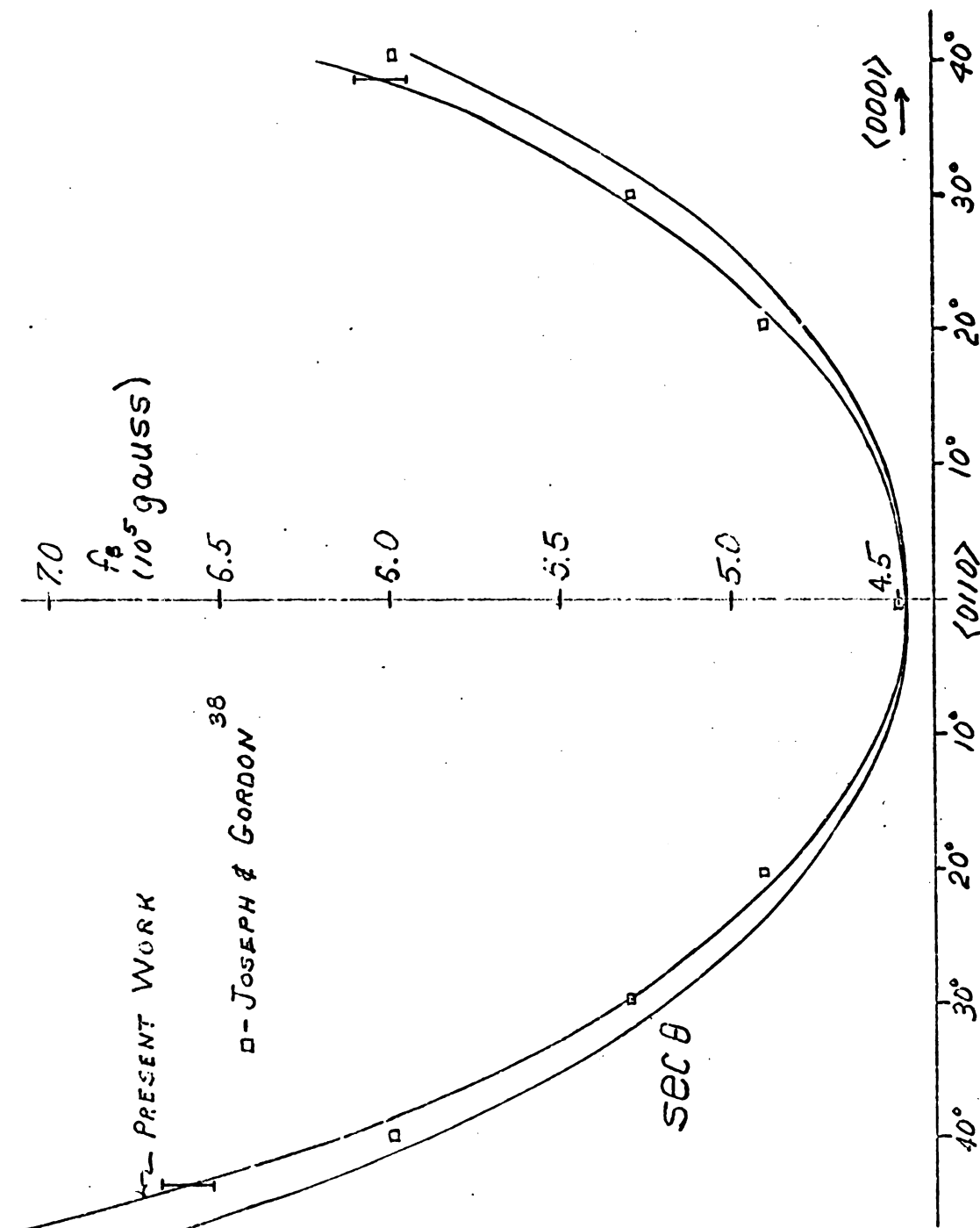


Figure 34 . $|S_\alpha|$ vs. θ Zn 2

Figure 35. $|S_H|$ vs. T , Zn 2

Figure 36. f_B vs. θ , Zn 2

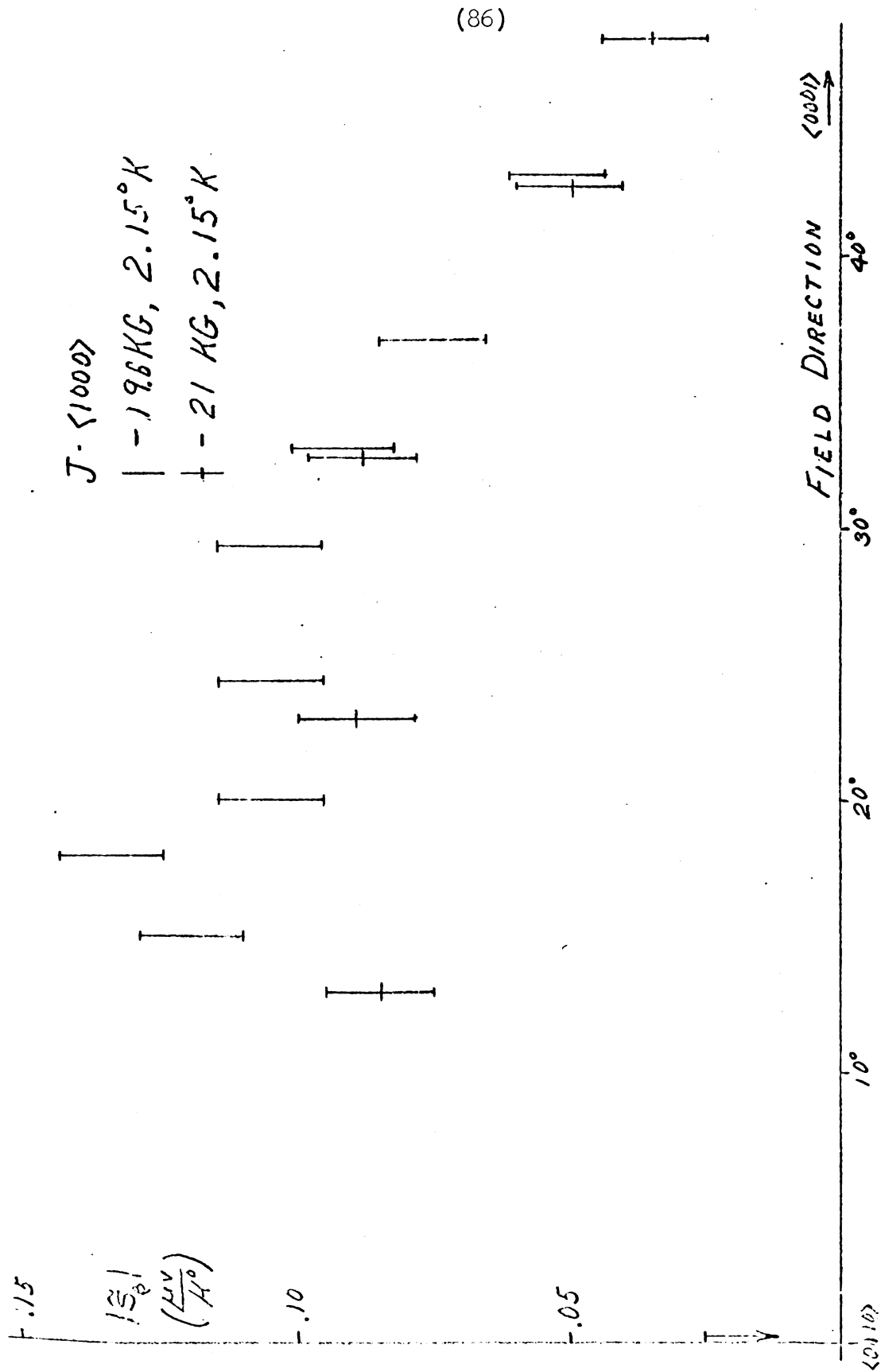


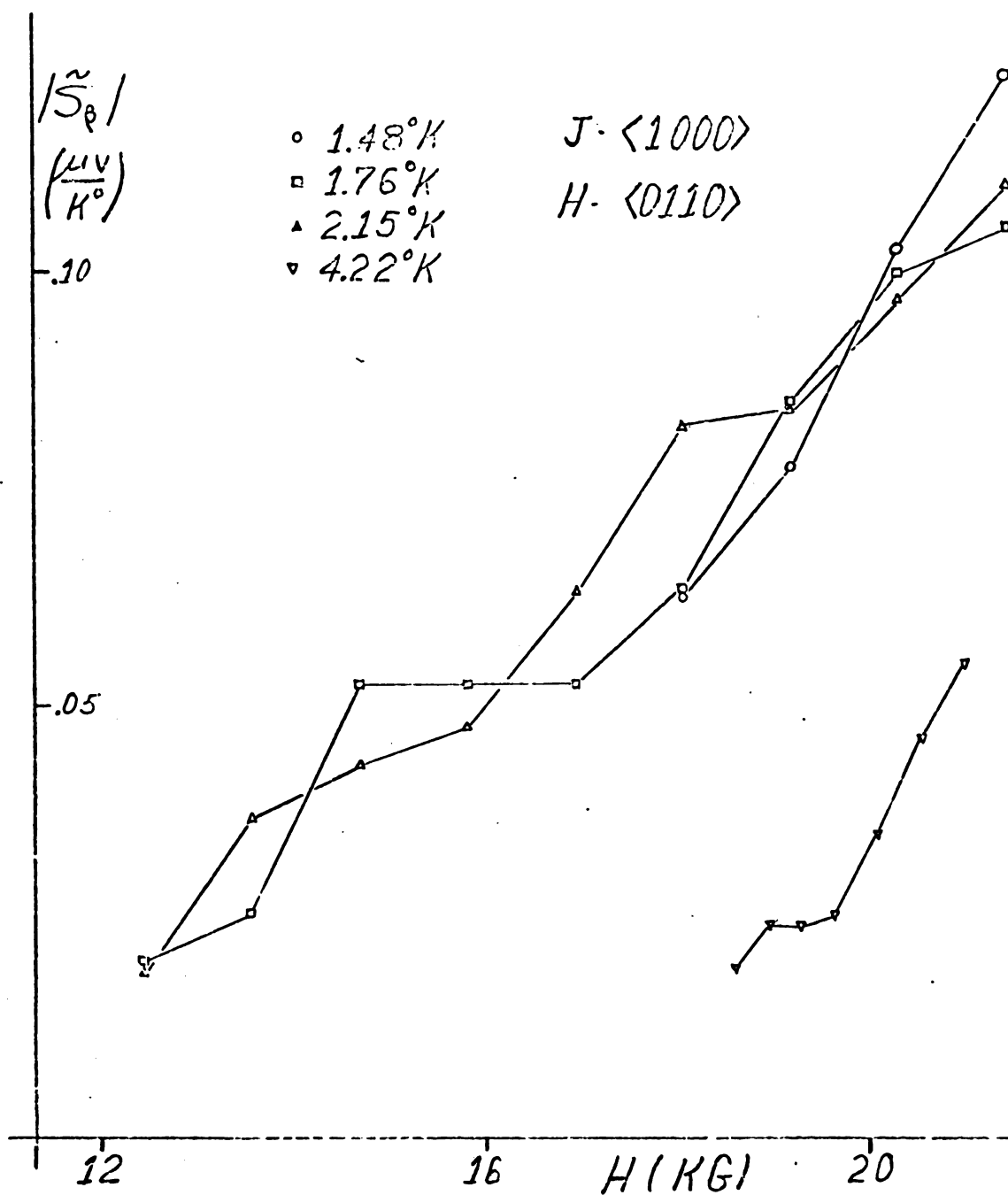
Figure 37. $|\mathcal{S}_\beta|$ vs. θ , Zn 2

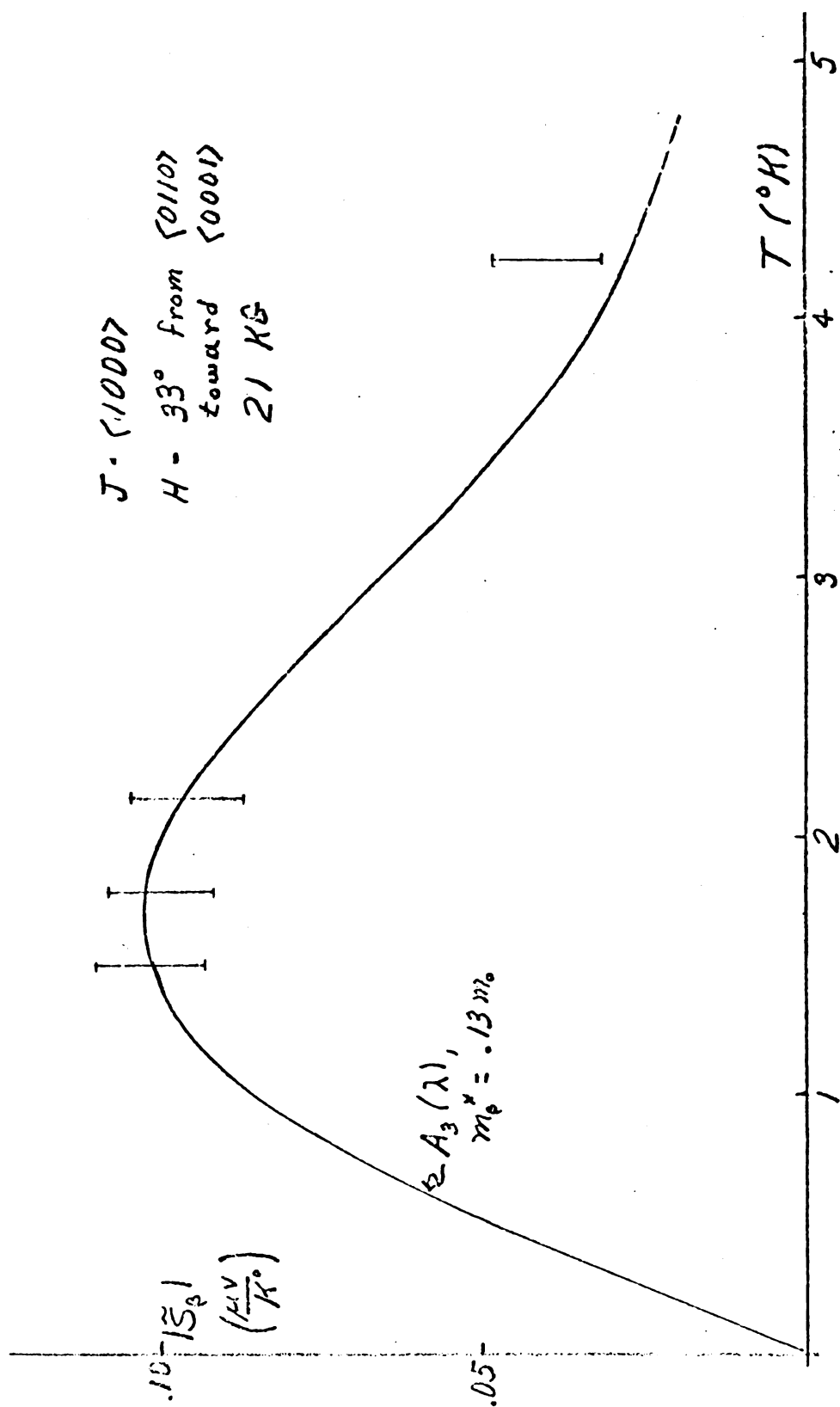
impossibility of measuring the amplitude of these oscillations with the field directly along $\langle 0110 \rangle$ (see figure 37) all further studies were carried out 33° away from the $\langle 0110 \rangle$. The observed amplitudes are plotted vs field strength in figure 38 and vs temperature in figure 39. These results include little harmonic interference, as the continuous detection mode was used (see section VIII C) in which case PSD2 acts as a low pass filter.

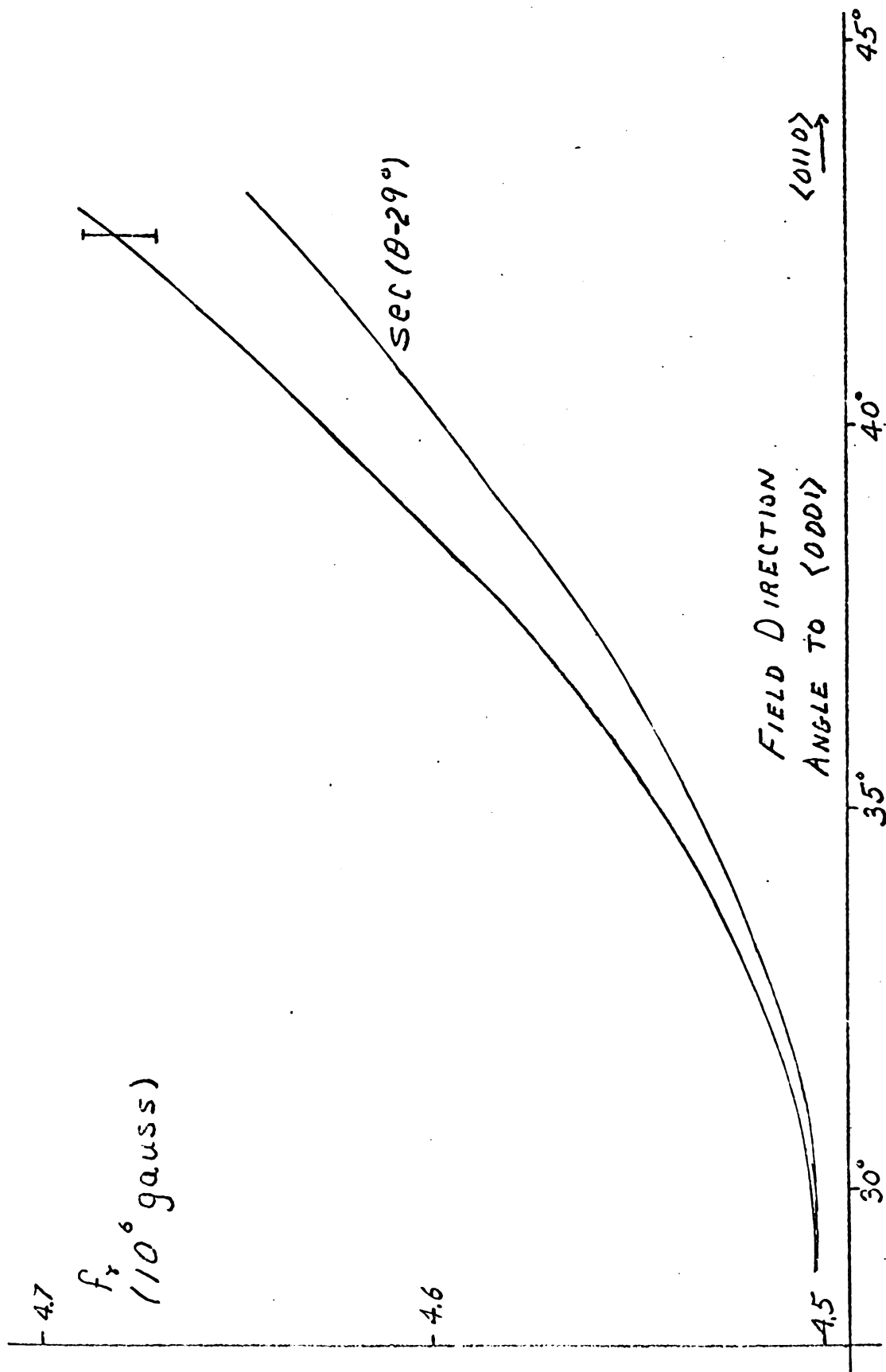
3. Monster Arm (γ) Oscillations

The frequency of the γ oscillations is plotted against field direction in figure 40. These results were obtained from a field sweep at 155° and the rotational data. A plot of the amplitude as a function of field direction follows in figure 41.

It was rather difficult to find a field direction in which the beating of several γ oscillations was absent. We picked field directions approximately 34° away from the $\langle 0001 \rangle$ for our measurements of the amplitude. The results are shown in figures 43, 44 and 45. As there was beating for both field angles we have plotted the average amplitude in figures 44 and 45.

Figure 38. $|\tilde{S}_\beta|$ vs. H, Zn 2

Figure 39. $|S_g|$ vs. T , Zn 2

Figure 40. f_r vs. θ , Zn 2

(91)

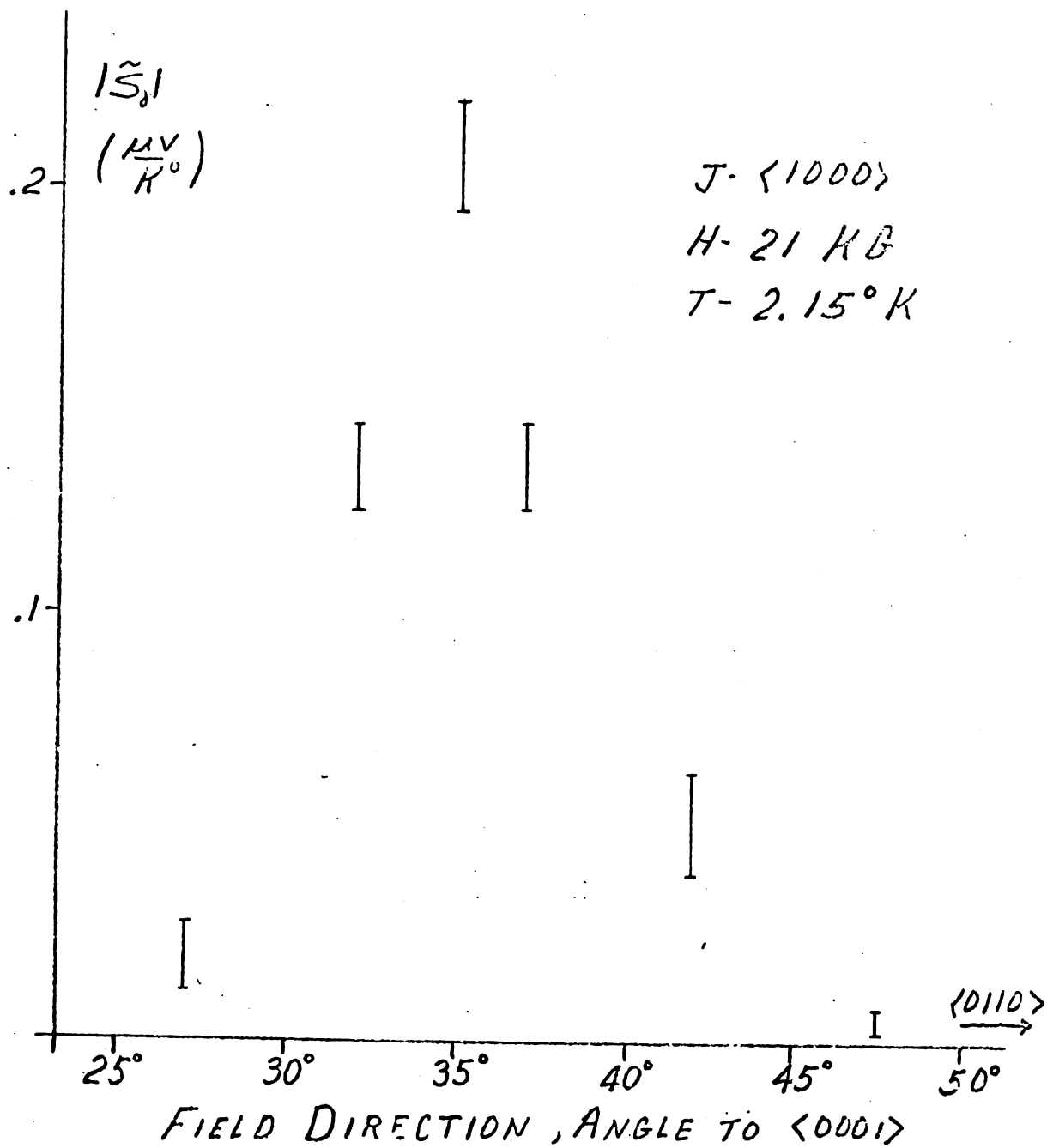


Figure 41. $|S_y|$ vs. θ , Zn 2

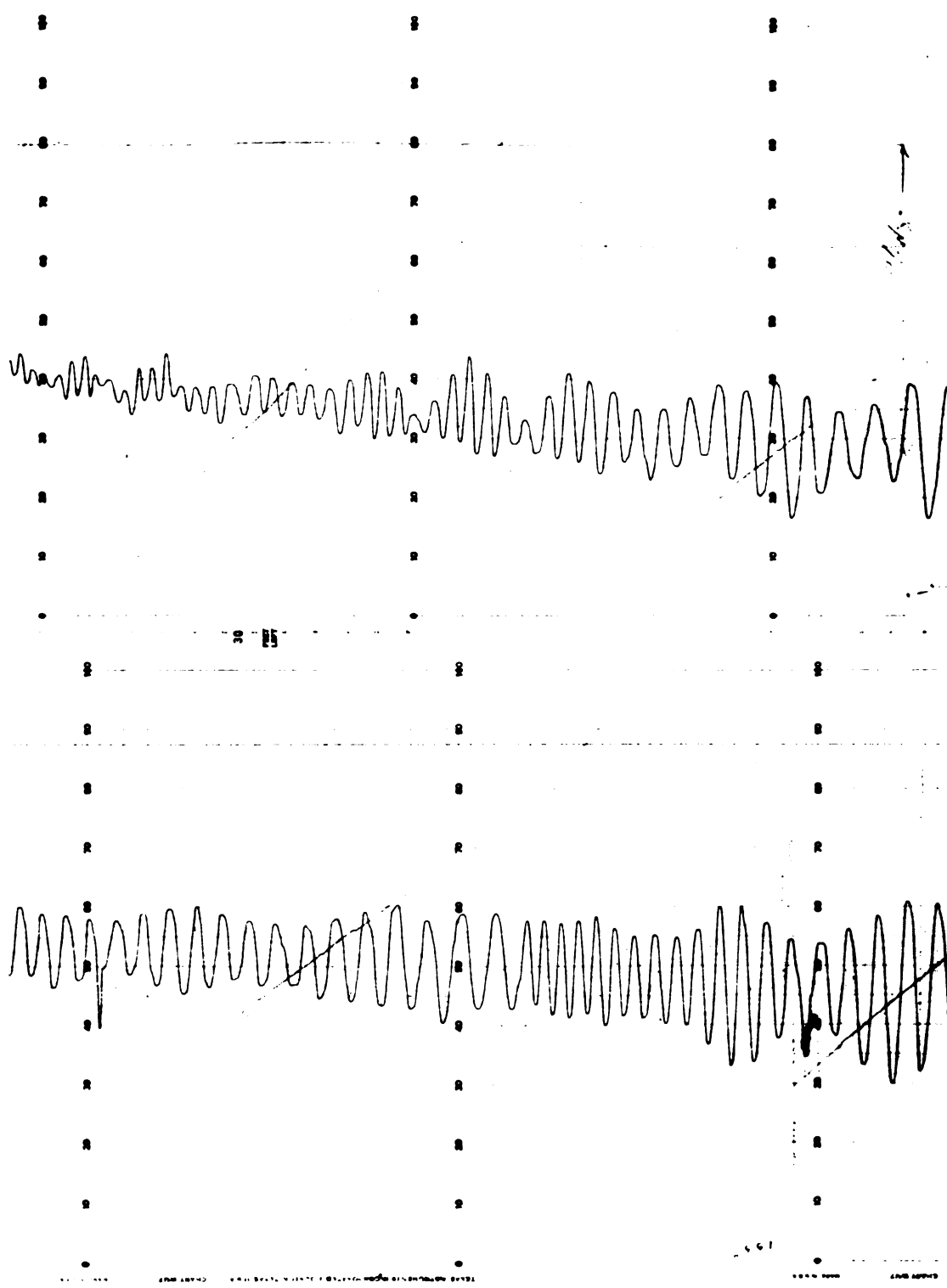


Figure 42. Typical γ oscillations,
continuous detection mode

(93)

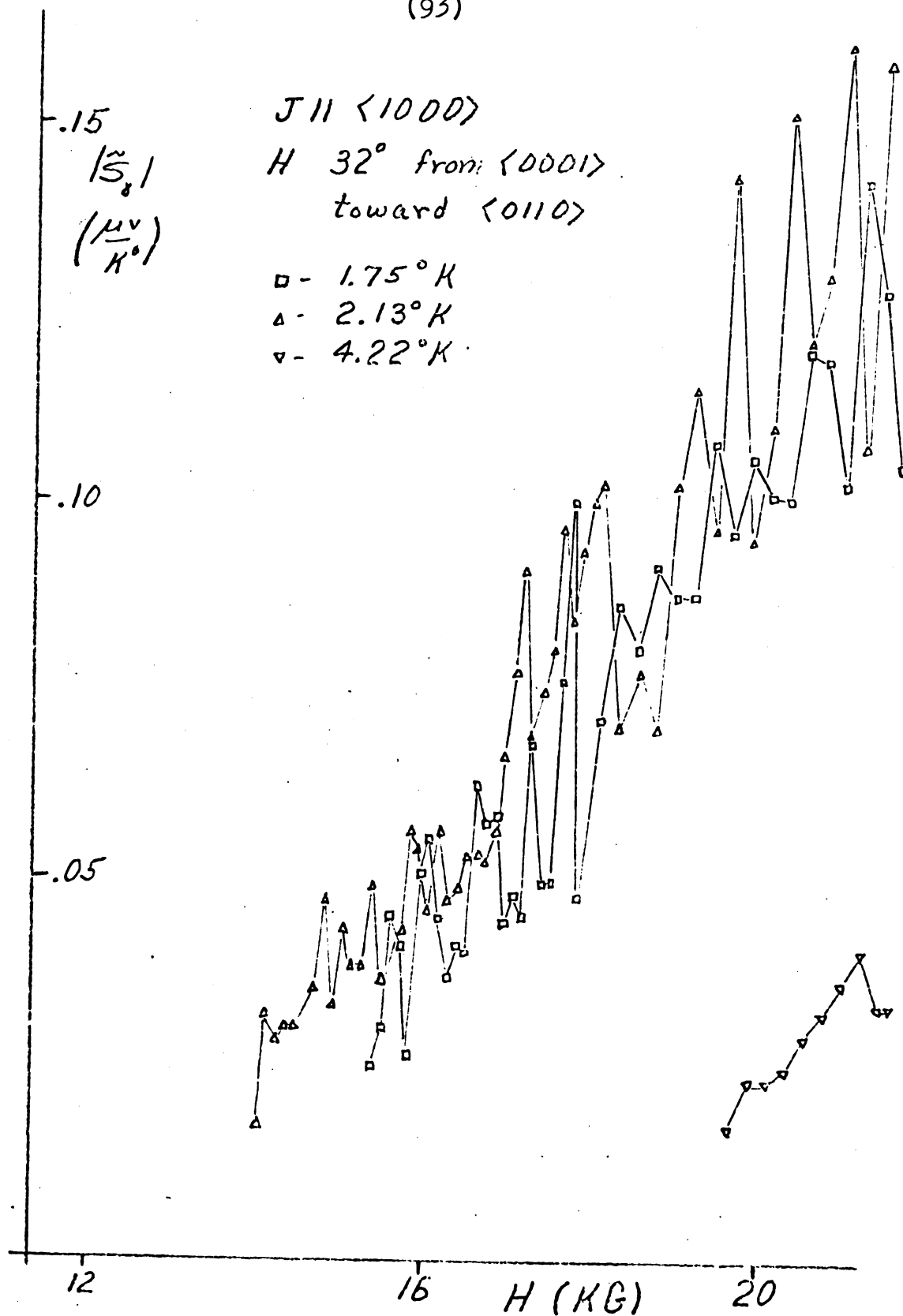


Figure 43. $|\tilde{S}_y|$ vs. H , Zn 2

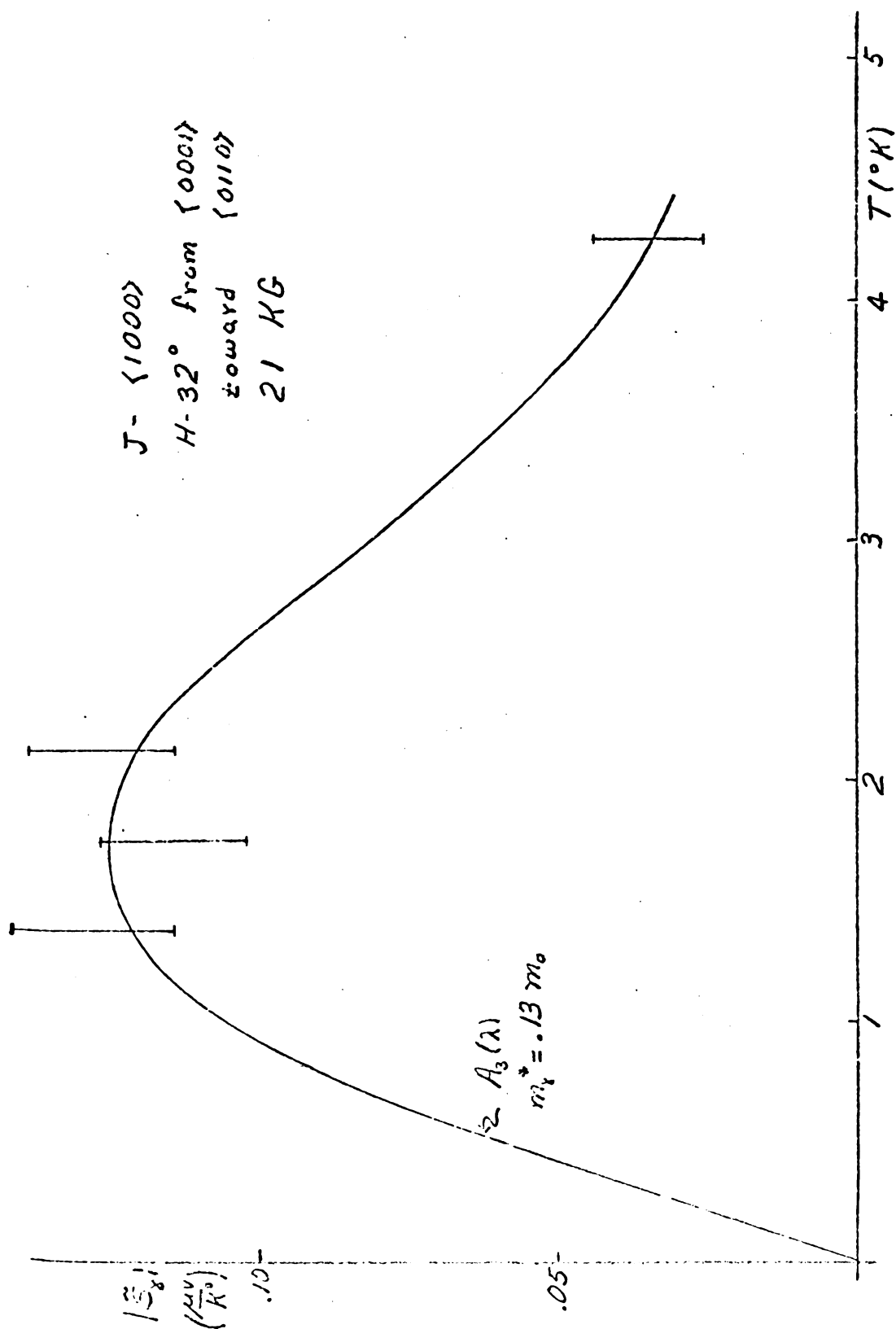


Figure 44. $|S_y|$ vs. T , Zn 2, 32° from $\langle 0001 \rangle$

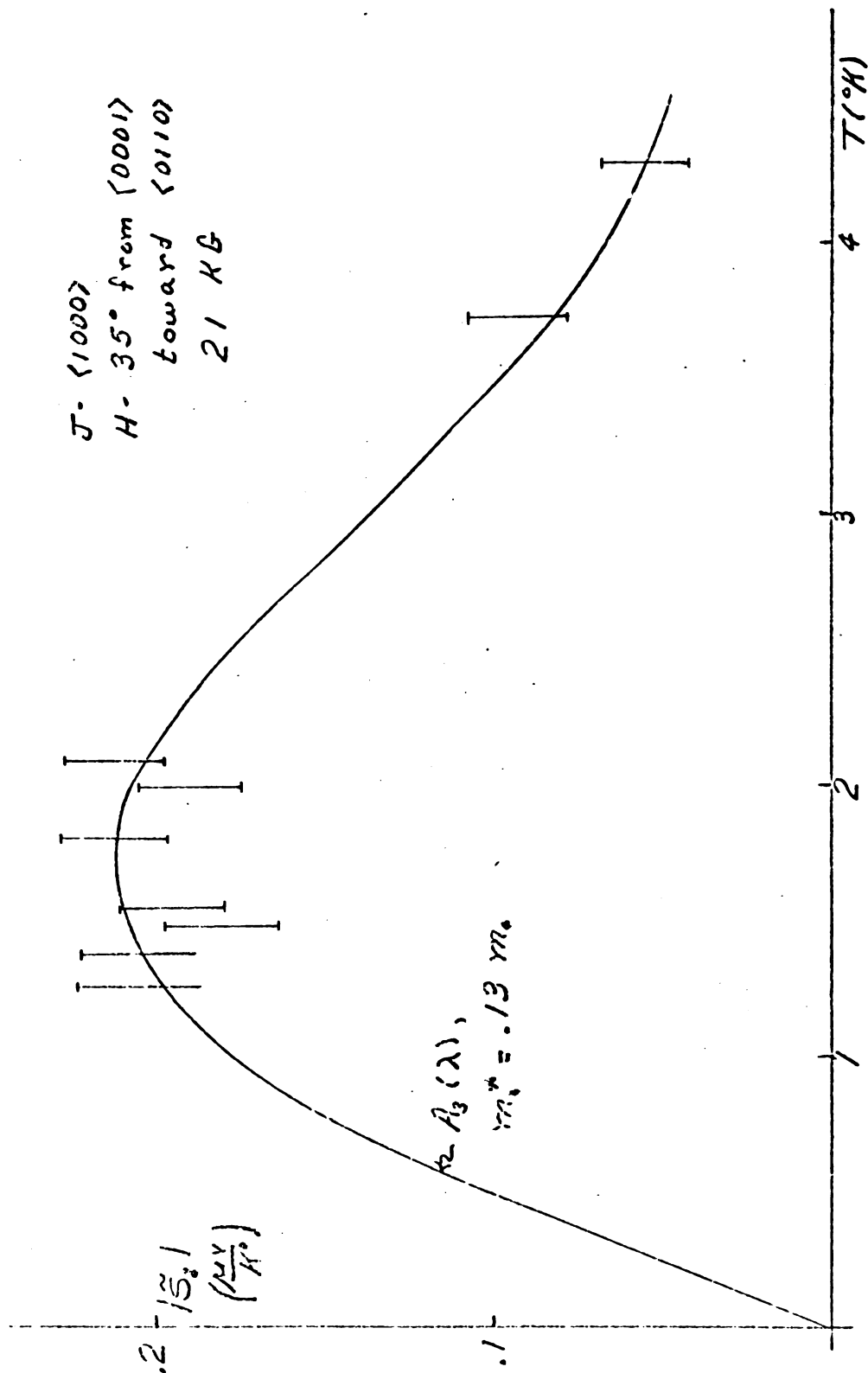


Figure 45. $|\mathfrak{S}_y|$ vs. T , Zn 2, 350 from $\langle 0001 \rangle$

X. Conclusions

A. Modified Horton Theory In Zinc

The result given by equation 86 is valid only if the relaxation time τ is constant over the Fermi surface. If, however, the relaxation time is not constant, it is evident from the discussion leading to equation 86 that that equation must be multiplied by $\eta = \tau_R/\tau_1$, where τ_1 is relaxation time for the section of the Fermi surface responsible for the oscillations and τ_R is given by equation 82. It must be remembered, however, that the entire theory assumes that the scattering potential can be approximated by a δ function. Subject to this assumption, the oscillations should still follow the form

$$\tilde{S} = S_0 \sum_{\nu} \left(\frac{-1}{\nu}\right)^{\nu} \exp\left[\frac{-\pi\nu}{\omega_c \tau_D}\right] A_3(\lambda) \sin b \quad . \quad (117)$$

The temperature dependence of the fundamental should then be given by $A_3(\lambda)$, where λ is defined by equation 47. The field dependence of the fundamental amplitude should be proportional to

$$\exp\left[\frac{-\pi}{\omega_c \tau_D}\right] A_3(\lambda) \quad . \quad (118)$$

Evidently the parameter τ_D can be derived from the measured amplitude $|\tilde{S}(H)|$ through the use of the equation

(97)

$$\ln \left[\frac{|\tilde{S}(H)|}{A_3(\lambda)} \right] = \frac{1}{\tau_D} \left(\frac{\pi m^* c}{e} \right) \frac{1}{H} + \text{constant} \quad (119)$$

and the slope of a plot of $\ln \left[\frac{|\tilde{S}(H)|}{A_3(\lambda)} \right]$ vs. $\frac{1}{H}$. The exact harmonic content one obtains from equation 117 is probably somewhat unreliable for the factor $(-1)^v/v$ may depend on the shape of the Fermi surface. Nonetheless the relative harmonic content should include the factor

$$\exp\left[\frac{-\pi v}{\omega_c \tau_D}\right] A_3(\lambda) \quad . \quad (120)$$

In zinc equation 86 becomes

$$\tilde{S} = 2.9 \times 10^{37} \text{ } \mu\text{v/K}^0 \left\{ \frac{N(m^*/m_o)}{(\partial^2 A / \partial k_z^2)_{k_o}} f_H^{1/2} a \right\} \sum_v \left[\quad \right] \quad . \quad (121)$$

All units used in the further evaluation of equation 121 must be gaussian. This equation must be multiplied by the factor η defined above if the relaxation time is not constant over the Fermi surface.

B. Auxiliary Data

The evaluation of the parameter a requires a knowledge

(98)

of the magnetoresistance $[\Delta\rho/\rho_0]$. This may well be a function of both the current and field directions.

Stark²⁵ has made measurements suitable for application to the Zn 1 measurements. He reports a magnetoresistance of

$$\frac{\Delta\rho}{\rho_0} = 12 + [108/(\text{KG})^2] H^2 . \quad (122)$$

Thus,

$$a_{\text{Zn } 1} = [1.08 \times 10^{-4}] \rho_0^2 . \quad (123)$$

Unfortunately the exact value of ρ_0 is not reported although the residual resistance ratio (ρ_{300°/ρ_0) is given as almost 50,000. The use of the resistivity at an elevated temperature (eg. 3°K) in the denominator of the resistance ratio would of course reduce the ratio, i.e.

$$\frac{\rho_{300^\circ}}{\rho_T} < 50,000 \quad (124)$$

We shall assume that the resistance ratio for the ρ_0 appearing in equation 123 is given by 35,000. As this may be in error by as much as 40 per cent, the value of a obtained may be in error by a factor of 2,

$$a_{\text{Zn } 1} = [1.08 \times 10^{-4}] (\rho_{300^\circ})^2 / (35,000)^2 . \quad (125)$$

(99)

The handbook value for the room temperature resistance of zinc is $7.0 \mu\Omega\text{-cm}$ ⁵⁶, giving

$$a = 4 \times 10^{-48} \text{ gaussian units} . \quad (126)$$

Stark has also reported magnetoresistance data on a crystal of the same orientation as our Zn 2. Unfortunately the value of \underline{a} derived from his measurements suffers from the same uncertainty that is discussed above. Assuming a resistance ratio of 35,000 and a room temperature resistance of $6.7 \mu\Omega\text{-cm}$, we can plot the value of \underline{a} as a function of field direction (see figure 46). Of course \underline{a} is not defined near the $\langle 0110 \rangle$ and $\langle 0001 \rangle$ axes where the magnetoresistance saturates.

One of the assumptions made in the derivation of equation 86 was that the Hall field is small. In particular, we must establish that

$$\frac{R_H H}{\rho} \ll \omega_c \tau . \quad (127)$$

Logan and Marcus³⁹ have reported Hall effect measurements on a zinc crystal with the current vector lying $8 \frac{1}{2}$ degrees from the $\langle 0001 \rangle$ axis. For no field direction did they find a Hall resistivity ($R_H H$) larger than $1.5 \times 10^{-9} \Omega\text{-cm}$ in fields to ten kilogauss. In such a field the resistivity of our Zn 1 should be at least $10^{-7} \Omega\text{-cm}$, thus reducing inequality 127 to

$$.015 \ll \omega_c \tau . \quad (128)$$

(100)

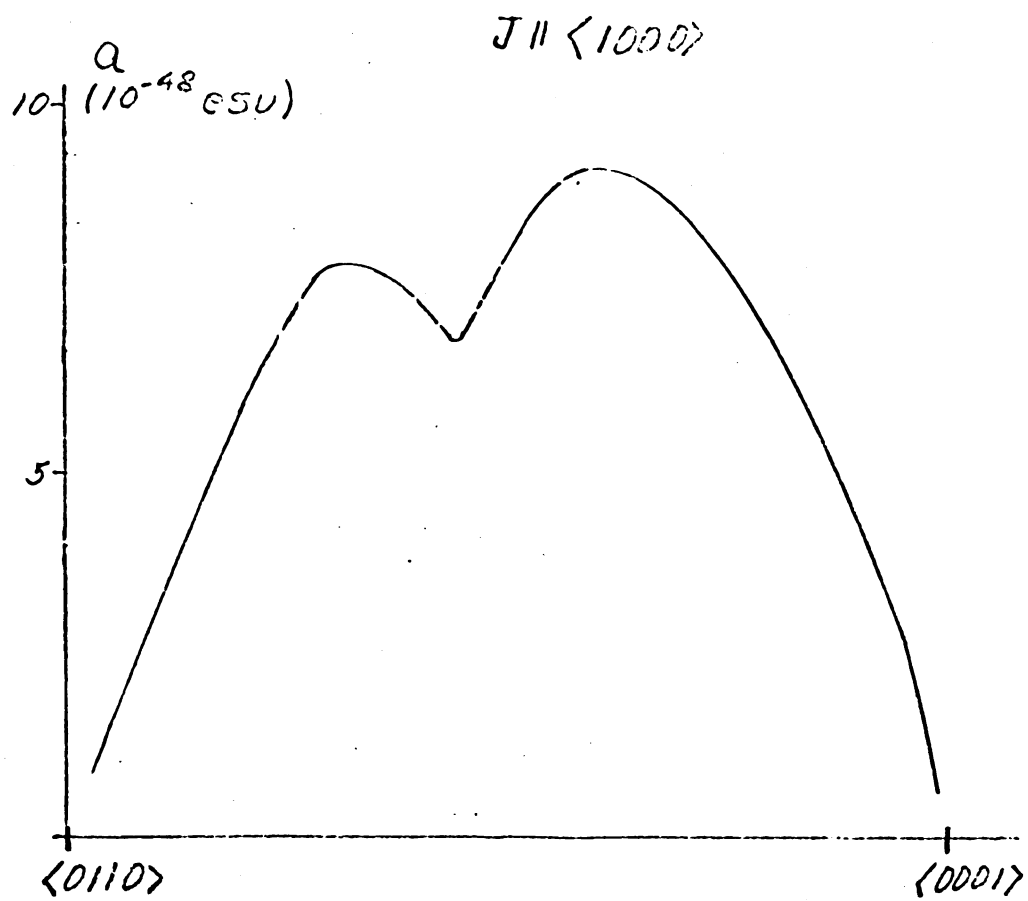


Figure 46. a vs. θ , Zn 2

At higher fields inequality 127 should become even less restrictive because the resistivity is proportional to H^2 and the Hall resistivity tends to decrease with increasing fields³⁹.

The evaluation of the right hand side of 127 requires a knowledge of the relaxation time τ about which there is a significant uncertainty (see section X, D, 2). The use of the resistivity relaxation time defined by equation 82 results in an $\omega_c \tau$ of about 1000 in Zn 1 for the β orbits at 20 kilogauss. As even the smallest apparent Dingle relaxation time (table 3) does not imply an $\omega_c \tau$ of less than 1, it would appear that we are justified in neglecting the Hall term in the expression for \mathfrak{S} (equation 57) in reference to Zn 1.

Hall effect measurements in a crystal of the same orientation as Zn 2 have been reported by Borovik⁴¹. He reports the ratio of Hall field to resistivity field for all field directions and in fields as large as 25 kilogauss. This ratio remains below .1 except when the field is near the $\langle 0001 \rangle$ axis or the basal plane. Thus for this crystal inequality 128 becomes

$$.1 \ll \omega_c \tau \quad (129)$$

Since the effective mass of both the β and the γ orbits is the same ($.13 m_0$), the values of $\omega_c \tau$ obtained using the resistivity relaxation time are identical,

$$(\omega_c \tau)_\gamma = (\omega_c \tau)_\beta \approx 100$$

in Zn 2. Inequality 129 is thus satisfied. If we again use the smallest apparent Dingle relaxation time, $\omega_c \tau$ becomes slightly larger than unity, thus introducing the possibility of a 10 per cent error in equation 86 when applied to Zn 2 calculations.

The curvature of the Fermi surface $(\partial^2 A / \partial k_z^2)_{k_0}$ can be obtained from equation 72 and values of α extracted from the data represented in figures 36 and 40 or can be calculated through the use of equation 80. The results of these operations are listed in table 1.

Table 1. Fermi surface curvature

	eq.72	eq.80(N.F.E. Approx.)
$(\partial^2 A / \partial k_z^2)_{k_0}, \beta$	1.1	.235
$(\partial^2 A / \partial k_z^2)_{k_0}, \gamma$	1.9	.75

In all further calculations we shall use the results of equation 72. In any event this factor has a relatively small effect on the calculation (<50 per cent), as it enters as a square root in equation 121.

C. The α Oscillations

A calculation of the amplitude to be expected in the α oscillations is all but impossible. Magnetic breakdown occurs between the needles and the monster in fields greater

than about one kilogauss^{35,36}, invalidating Hortons treatment. The probability of breakdown depends on the oscillating density of states on the surface of the needle providing a complex mechanism for obtaining oscillatory effects and giving rise to very large (~ 80 per cent) Shubnikov-de Haas oscillations^{35,36}. Furthermore a very large Hall effect has been measured with the field along the $\langle 0001 \rangle$ axis^{35,36}; in fact there are few assumptions made in the derivation of equation 86 which are valid in this case.

D. The β And γ Oscillations

1. Absolute Amplitude

The cyclotron mass of the electron in a β orbit is $.12 m_0$ if the field is directly along the $\langle 0110 \rangle$ and scales approximately as the frequency in other field directions³⁸. The γ orbits have roughly the same cyclotron mass ($.13 m_0$) when the field is directed along the axis of the monster arms.³⁸ For our amplitude calculations we shall use an effective mass ratio of $.13$ which should be accurate to about 20 percent. Table 2 gives the calculated amplitude factor (i.e. everything outside the summation) obtained from equation 121 for the various oscillations observed, along with the amplitudes measured at the maximum of the amplitude vs. temperature curve. All amplitudes are calculated for a magnetic field of 20 kilogauss. The last column is meaningful only if the Dingle factor $\exp[-\pi/\omega_c \tau]$ is near unity. The use of the resistivity relaxation time defined by equation 82 results in a value larger than $.9$ for this factor. Evidently the ratios in the last column of table 2 represent a substantial disagreement between the theory and the measurements.

Table 2. Comparison of theoretical and experimental amplitudes

	J	H	$ S _{th}(\frac{\mu V}{K^\circ})$	$ S _{exp}(\frac{\mu V}{K^\circ})$	$\frac{ S _{exp}}{ S _{th}}$
β osc.	$\langle 0001 \rangle$	$\langle 0110 \rangle$.0016	.05	32
β osc.	$\langle 1000 \rangle$	$\langle 0110 \rangle$ +33°	.002	.10	50
γ osc.	$\langle 1000 \rangle$	$\langle 1000 \rangle$ +35°	.020	.20	10

2. Field Dependence, Apparent Dingle Factor

The use of equation 119 to derive an effective Dingle relaxation time from the data presented in figures 29, 38 and 43 results in the values listed in table 3. The last

Table 3. Apparent Dingle relaxation times

	J	H	T(°K)	$\tau_D(10^{-13} \text{sec})$	$\tau_R(10^{-13} \text{sec})$
β	$\langle 0001 \rangle$	$\langle 0110 \rangle$	1.35	4.65 \pm 10	2100
	$\langle 1000 \rangle$	$\langle 0110 \rangle$ +33°	1.78	7.1 \pm 10	
			4.22	2.3 \pm 30	560
γ	$\langle 1000 \rangle$	$\langle 0001 \rangle$ +33°	1.75	5.35 \pm 30	
			4.2	4.5 \pm 30	

column lists the resistivity relaxation times. If the effective values of τ_D represent the real relaxation time of the

orbits in question the Dingle factor becomes quite small, approximately 0.1. This would reduce the calculated amplitude estimates listed in table 2 by an order of magnitude. It is interesting that if we also include the factor τ_R/τ_D as suggested in section X.A we calculate the amplitudes listed in table 4, which are in much better agreement with the data. The value of τ_D used in these calculations was

Table 4. Revised amplitude estimates

	J	H	$ \mathfrak{S} _{th}(\mu v/K^0)$	$ \mathfrak{S} _{exp}(\mu v/K^0)$
β	$\langle 0001 \rangle$	$\langle 0110 \rangle$.072	.05
β	$\langle 1000 \rangle$	$\langle 0110 \rangle + 33^\circ$.02	.10
γ	$\langle 1000 \rangle$	$\langle 0001 \rangle + 35^\circ$.2	.20

5×10^{-13} sec., which is near the average of those listed in table 3.

Unfortunately there is a very basic difficulty with this argument. If we include the Dingle factor of .1 in the calculation we must consider the effect it has on the harmonics, namely a very strong damping, $(.1)^{n+1}$ for the n th harmonic. This prediction is clearly at variance with the high harmonic content observed in the β oscillations.

There is a mechanism, the B-H effect⁴², which can give rise to nonsinusoidal wave shapes in the presence of complete collision damping of the harmonics. This effect arises because the field seen by an electron inside a material is

$$B = H + 4\pi\eta_m M \quad (131)$$

(106)

where γ_m is the demagnetization factor. Since the magnetization M is itself an oscillatory function of B , a nonlinear equation must be solved. For relatively small changes in B , this equation can be written

$$y = y_0 \sin(x + y) \quad (132)$$

$$x = \left(\frac{f}{H_0^2}\right) H \quad (133)$$

$$y = \frac{f}{H^2} (4\pi\gamma_m M) \quad (134)$$

The strength of the nonsinusoidal effects introduced in this way depends upon the magnitude of y_0 ; if y_0 is much less than unity the effect becomes negligible.

An expression for the de Haas-van Alphen (magnetization) oscillations can be obtained from the free energy (equation 34) by the thermodynamic relation

$$M = \left(\frac{\partial F}{\partial H}\right)_T \quad (135)$$

From this one can find the following expression for y_0 :

$$y_0 = \frac{32\pi^3 kT (e/2\pi\hbar c)^{3/2} f^2 \gamma_m \exp(-\pi/\omega_c \tau)}{\sqrt{(\partial^2 A / \partial k_z^2)_{k_0}} [\sinh(2\pi kT/\hbar\omega_c)] H^{5/2}} \quad (136)$$

For the β oscillations in zinc,

$$y_0 = .003[\exp(-\pi/\omega_c \tau)] \quad (137)$$

at 20 kilogauss and 2°K. This is rather too small to give rise to significant nonsinusoidal behavior.

The arguments concerning the relaxation damping of harmonics are quite general.¹⁴ However, some theory is needed to extract values of the Dingle relaxation time τ_D from the data. It is therefore more reasonable to put faith into the harmonic argument, with the obvious conclusion that the field dependence predicted by Horton's theory is not nearly strong enough.

It might be noted that the possibility of extracting an apparent τ_D does not necessarily imply an exponential field dependence. There was generally a rather large amount of scatter in the data and another form of field dependence might have appeared exponential over the rather restricted field ranges used.

3. Temperature Dependence

In contrast to the field dependence and absolute amplitude of the oscillations, the temperature dependence shows at least qualitative agreement with Horton's theory. For purposes of comparison the expected form of this dependence, proportional to $A_3(\lambda)$, has been drawn in figures 27, 39, 44, and 45. The vertical scale of A_3 has been adjusted to approximately agree with the data, while the horizontal scale is of course defined by the cyclotron mass and the magnetic field. All cyclotron masses used for this purpose were those reported by Joseph and Gordon³⁸.

E. General Conclusions

Evidently much more theoretical work must be done before the amplitude of these oscillations can be understood. The difficulty with the theory presented here is probably in the scattering potential, as the form of this potential may affect the Seebeck coefficient quite strongly. Furthermore the theory cannot be easily modified to include any field dependent scattering.

More detailed experimental data may also assist in sorting out the field dependence due to collision broadening from the intrinsic field dependence. In particular, a study of the amplitude and the field dependence in crystals of varying purity would be very helpful.

F. Nonoscillatory Seebeck Coefficient

Although the exact form of the field dependence of the average Seebeck coefficient \bar{S} was not studied in detail, we did note two pronounced dips in \bar{S} . Both of these occurred for the field directly along the $\langle 0110 \rangle$ axis, although the current direction differed in the two cases. The theoretical results of Bychkov et. al.²⁴ would predict that \bar{S} is proportional to the field strength for all field directions out of the basal plane, but that it should saturate for field directions in the basal plane where significant bands of open orbits occur.^{35,36} This clearly is not in complete agreement with the experimental results.

References

1. T. J. Seebeck, Abhand. deut. Akad. Wiss. Berlin, p. 265 (1822-23); Ann. Physik 6, p.p. 1, 133, 253 (1826); Ostwald Klassiker 70, (1895), as referred to in reference 3.
2. J. C. A. Peltier, Ann. Chim. Phys. 56, p. 371(1834); L'Institut 2, p.p. 133, 265 (1845), as referred to in reference 3.
3. B. S. Finn, Physics Today 20, p. 54 (1967).
4. C. A. Domenicali, Rev. Mod. Phys. 26, p. 237 (1954).
5. S. R. de Groot and P. Mazur, Non Equilibrium Thermodynamics, North-Holland Publishing Co., Amsterdam (1962), p.p. 338-375.
6. J. F. Nye, Physical Properties of Crystals, Oxford University Press, London (1957), p.p. 215-232.
7. J. M. Ziman, Electrons and Phonons, Oxford University Press, London (1960), p. 273.
8. N. F. Mott and H. Jones, The Theory of the Properties of Metals and Alloys, Oxford University Press, London (1936), reprinted by Dover Publications, New York (1958), p. 308.
9. H. M. Rosenberg, Low Temperature Solid State Physics, Oxford University Press, (1963), p. 352.
10. C. Kittel, Quantum Theory of Physics, John Wiley and Sons, New York (1963), p.p. 179-267.
11. A. B. Pippard, Low Temperature Physics, Gordon and Breach, New York (1962), p.p. 3-146.
12. W. A. Harrison, Pseudopotentials in the Theory of Metals, W. A. Benjamin, New York (1966).
13. L. Onsager, Phil. Mag. 43, p. 1006 (1962).
14. A. D. Brailsford, Phys. Rev. 149, p. 456 (1966).

15. R. B. Dingle, Proc. Roy. Soc. 506, p. 517 (1952).
16. E. I. Blount, Phys. Rev. 126, p. 1636 (1962).
17. E. N. Adams and T. D. Holstein, J. Phys. Chem. Solids 10, p. 254 (1959).
18. E. M. Lifshitz and A. M. Kosevich, J. Phys. Chem. Solids 4, p. 1 (1958).
19. P. S. Zyryanov, Phys. of Metals and Metallography 18, no. 2, p. 1 (1964).
20. P. S. Zyryanov and V. P. Kalashikov, Phys. of Metals and Metallography 18, no. 2, p. 8 (1964).
21. G. I. Guseva, Phys. of Metals and Metallography 18, no. 3, p. 1 (1964).
22. G. E. Zilberman, JETP (USSR) 29, p. 762 (1955), English translation in JETP 2, p. 650 (1956).
23. P. B. Horton, Quantum Transport Theory of Free Electrons in a Strong Magnetic Field, Ph.D. dissertation, Louisiana State University (1964).
24. Yu. A. Bychkov, L. E. Gurevich, and G. M. Nedlin, JETP (USSR) 37, p. 534 (1959), English translation in JETP 10, p. 377 (1960).
25. A. B. Pippard and G. T. Pullan, Proc. Camb. Phil. Soc. 48, p. 188 (1952).
26. A. R. DeVrooman and C. Van Baarle, Physica 23, p. 785 (1957).
27. I. M. Templeton, J. Sci. Instr. 32, p. 172 (1955).
28. I. M. Templeton, J. Sci. Instr. 32, p. 314 (1955).
29. A. M. Guenault, Phil. Mag. 15, p. 17 (1967).
30. C. L. Foiles, Rev. Sci. Inst. 38, p. 731 (1967).
31. J. Clarke, Phil. Mag. 13, p. 115 (1966).
32. J. J. LePage, Magnetothermal Oscillations and the Fermi Surface of Beryllium, Ph.D. dissertation, Michigan State University (1965).

33. J. C. Abele, Fermi Surface Studies of Aluminum and Dilute Aluminum - Magnesium Alloys Using the Magneto-thermal Oscillation Technique, Ph.D. dissertation, Michigan State University (1968).
34. D. F. Gibbons and L. M. Falicov, Phil. Mag. 8, p. 177 (1963).
35. R. W. Stark, Phys. Rev. 135A, p. 1698 (1964)
36. W. A. Reed and G. F. Brennert, Phys. Rev. 130, p. 565 (1963).
37. R. J. Higgins, J. A. Marcus, and D. H. Whitmore, Phys. Rev. 137A, p. 1172 (1965).
38. A. S. Joseph and W. L. Gordon, Phys. Rev. 126, p. 489 (1962).
39. J. K. Logan and J. A. Marcus, Phys. Rev. 88, p. 1234 (1953).
40. C. G. Grenier, J. M. Reynolds, and N. H. Zebouni, Phys. Rev. 129, p. 1088 (1963).
41. E. S. Borovik, JETP (USSR) 30, p. 262 (1956), english translation in JETP 3, p. 243 (1956).
42. A. B. Pippard, Proc. Roy. Soc. 272, p. 192 (1963).
43. J. A. Woollam, Electron Transport Properties of Metallic Tin in High Magnetic Fields and at Liquid Helium Temperatures, Ph.D. dissertation, Michigan State University (1967).
44. A. V. Gold and M. G. Priestly, Phil. Mag. 5, p. 1089 (1960).
45. M. Bailyn, Phys. Rev. 157, p. 480 (1967).
46. D. K. C. McDonald, Physica 20, p. 996 (1954).
47. J. M. Ziman, E & P, p. 407.
48. F. J. Blatt and R. H. Kropschot, Phys. Rev. 118, p. 480 (1960).

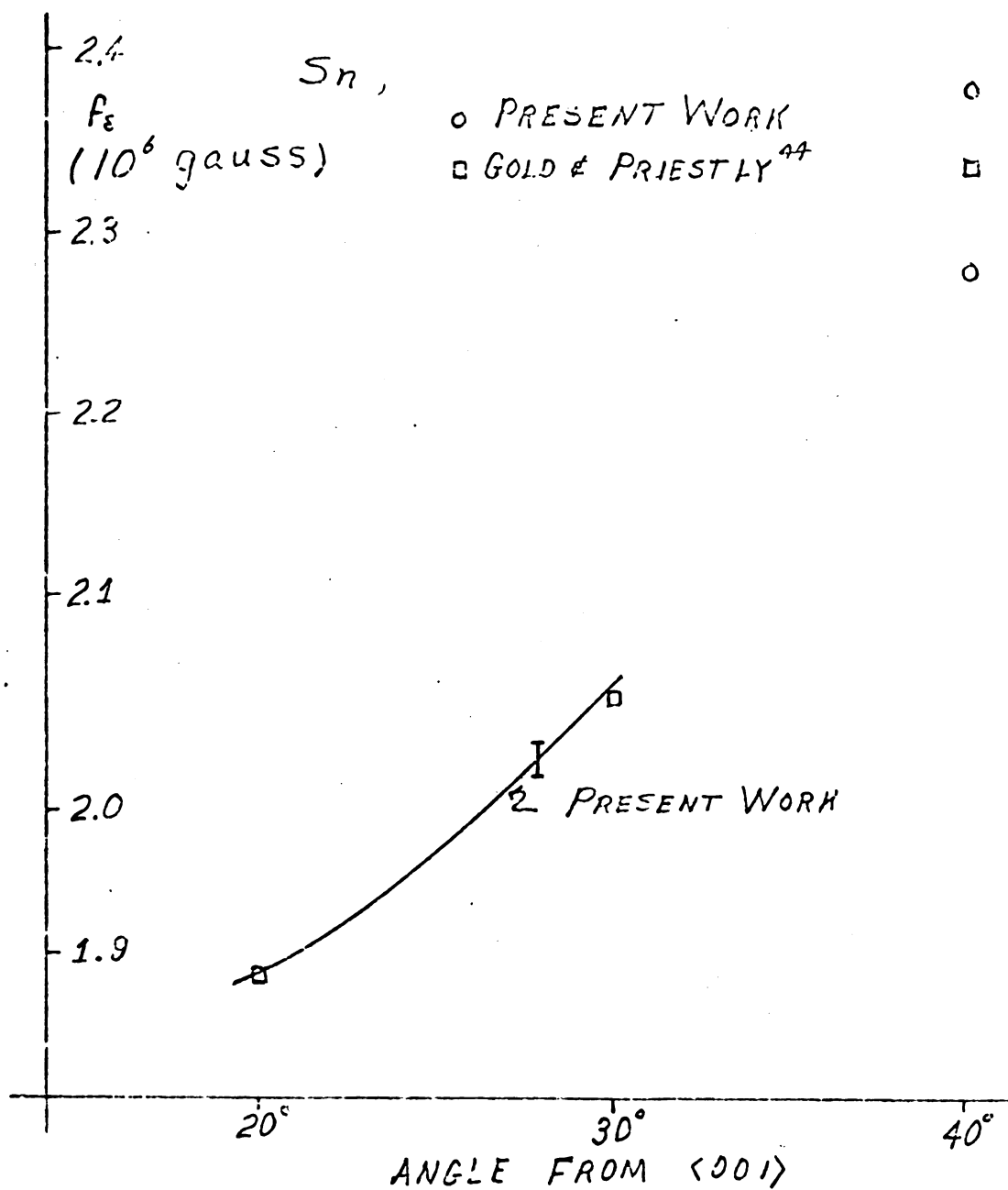
49. M. Garber, B. W. Scott, and F. J. Blatt, Phys. Rev. 130, p. 2188 (1963).
50. V. Rowe, Phonon Drag Thermopower in Cadmium, Zinc, and Magnesium, Ph.D. dissertation, Michigan State University (1967).
51. F. J. Blatt, D. J. Flood, V. Rowe, P. A. Schroeder, and J. E. Cox, Phys. Rev. Letters 18, p. 395 (1967).
52. M. C. Steele, Phys. Rev. 81, p. 262 (1951).
53. D. Grieg and J. P. Harrison, Phil. Mag. 12, p. 71 (1965).
54. P. A. Schroeder and A. I. Davidson, private communication.
55. L. Colquitt and H. Fankhauser, to be published.
56. Handbook of Chemistry and Physics, 30th edition, Chemical Rubber Publishing Co., Cleveland (1948), p. 1959.

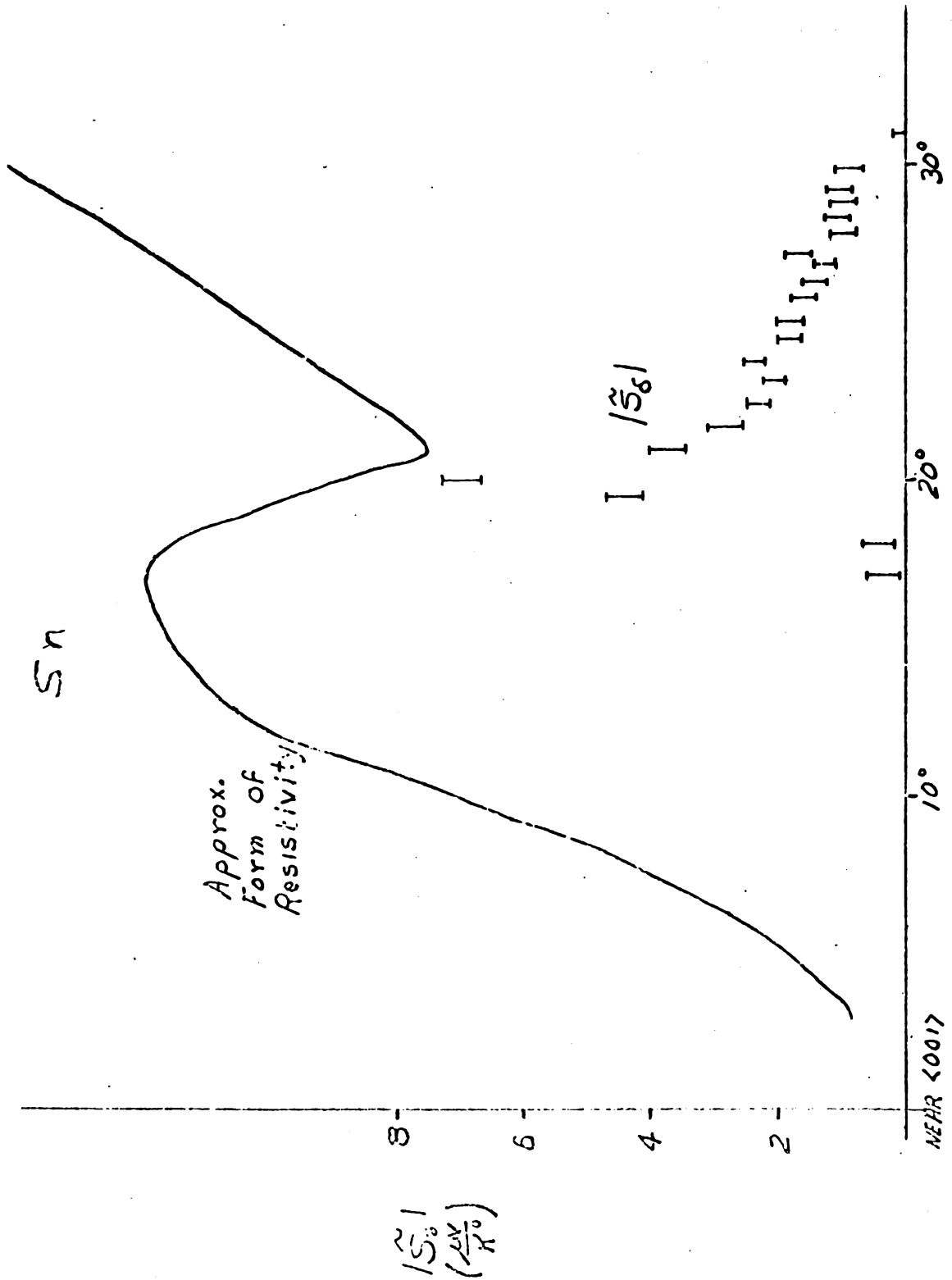
Appendix I

Sn Measurements

A single run was made on a tin crystal supplied by John A. Woollam, NASA, Cleveland. The crystal had a resistance ratio of about 30,000 and was oriented such that the cylinder axis was 79° from $\langle 001 \rangle$ and 86° from $\langle 110 \rangle$. All fields were applied in the plane perpendicular to the sample axis.

Figures 47 through 49 represent the data collected during this run. It will be noticed that the amplitude of the oscillations in tin are very large. The data obtained in this work appears to be quite consistent with the more conventional measurements performed by Woollam.⁴³

Figure 47 . f_{δ} vs. θ , Sn



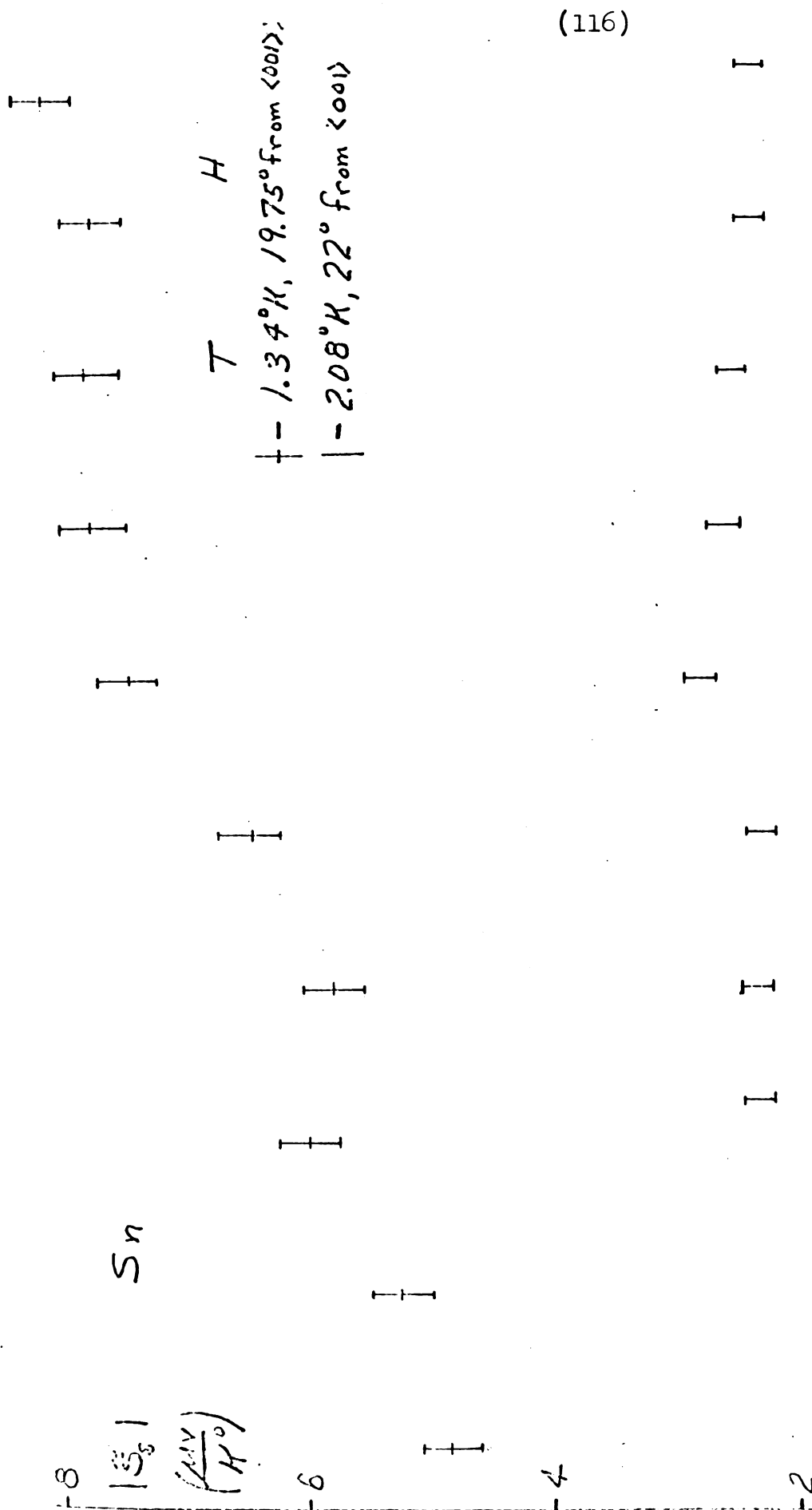


Figure 49. $|S_0|$ vs. H, S_n $H(KG)$ 20

Appendix II

Measurements on Polycrystalline Metals

Equation 28 can be applied to a metal in the impurity scattering region to obtain

$$S_i = \frac{\pi^2}{3} \frac{k^2 T}{e \epsilon_f} \quad . \quad (A-1)$$

If the same is done for high temperature phonon scattering,

$$S_p = \frac{\pi^2}{e \epsilon_f} \frac{k^2}{T} \quad . \quad (A-2)$$

These terms define what is known as the diffusion thermopower of metals. At intermediate temperatures one finds the so called phonon drag peaks in the thermoelectric power of most materials. This effect has been studied in some detail.⁴⁵⁻⁵⁰ There is also some evidence that a magnon drag effect may be present in metals.⁵¹

The cryostat and measuring techniques used in this study were essentially those used in the single crystal studies. Since the samples were in the form of wires the carbon resistors could not be attached directly; an intermediary copper block was used. The best reference material was found to be lead, which has a zero Peltier coefficient at liquid helium temperatures in the absence of a magnetic field. The electrical contacts were soldered.

The results of this study are shown in figures 50-55.

(118)

T (°K)

2

3

4

Pb in 1000 gauss

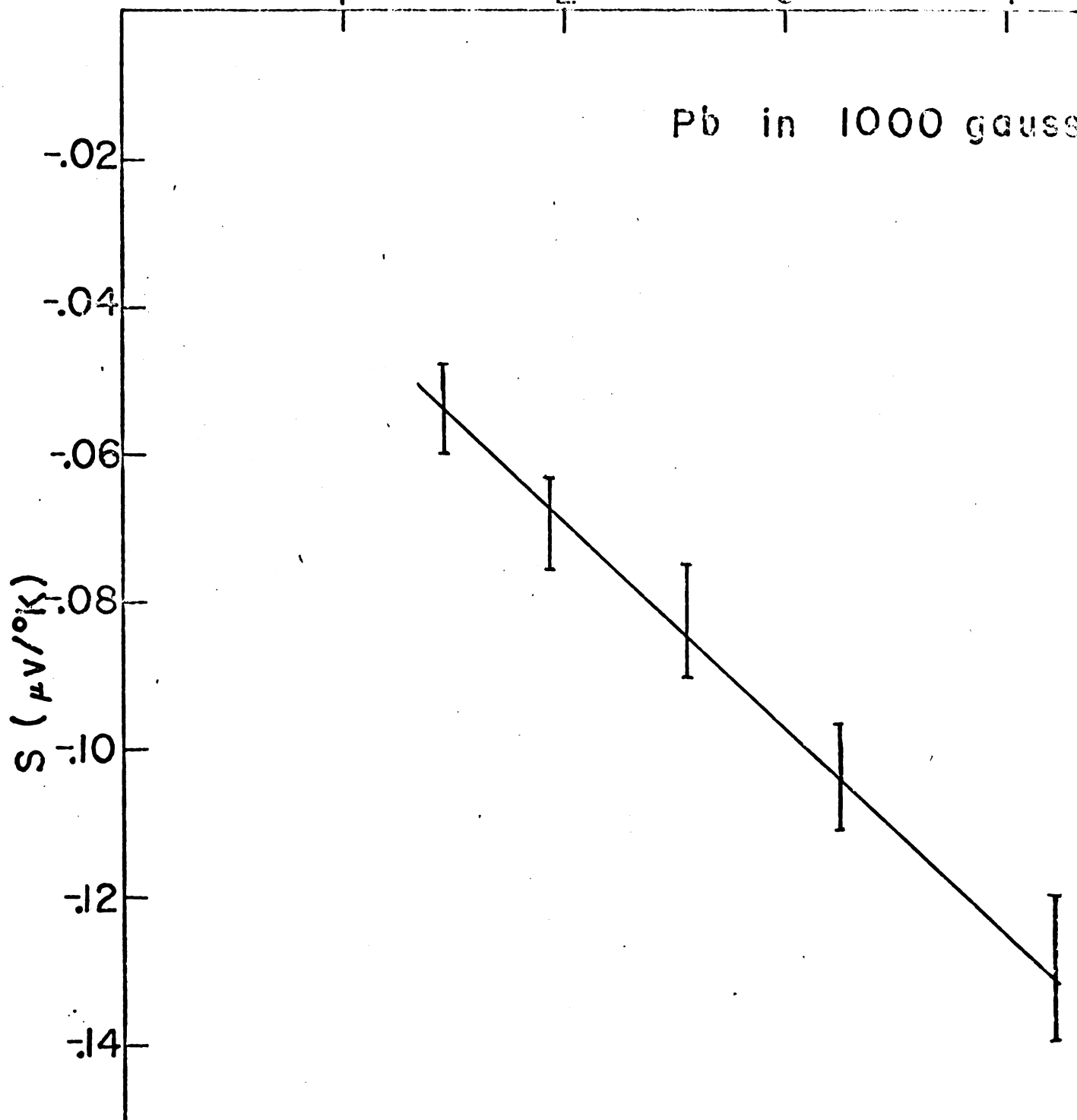


Figure 50. Seebeck coefficient
of Pb

(119)

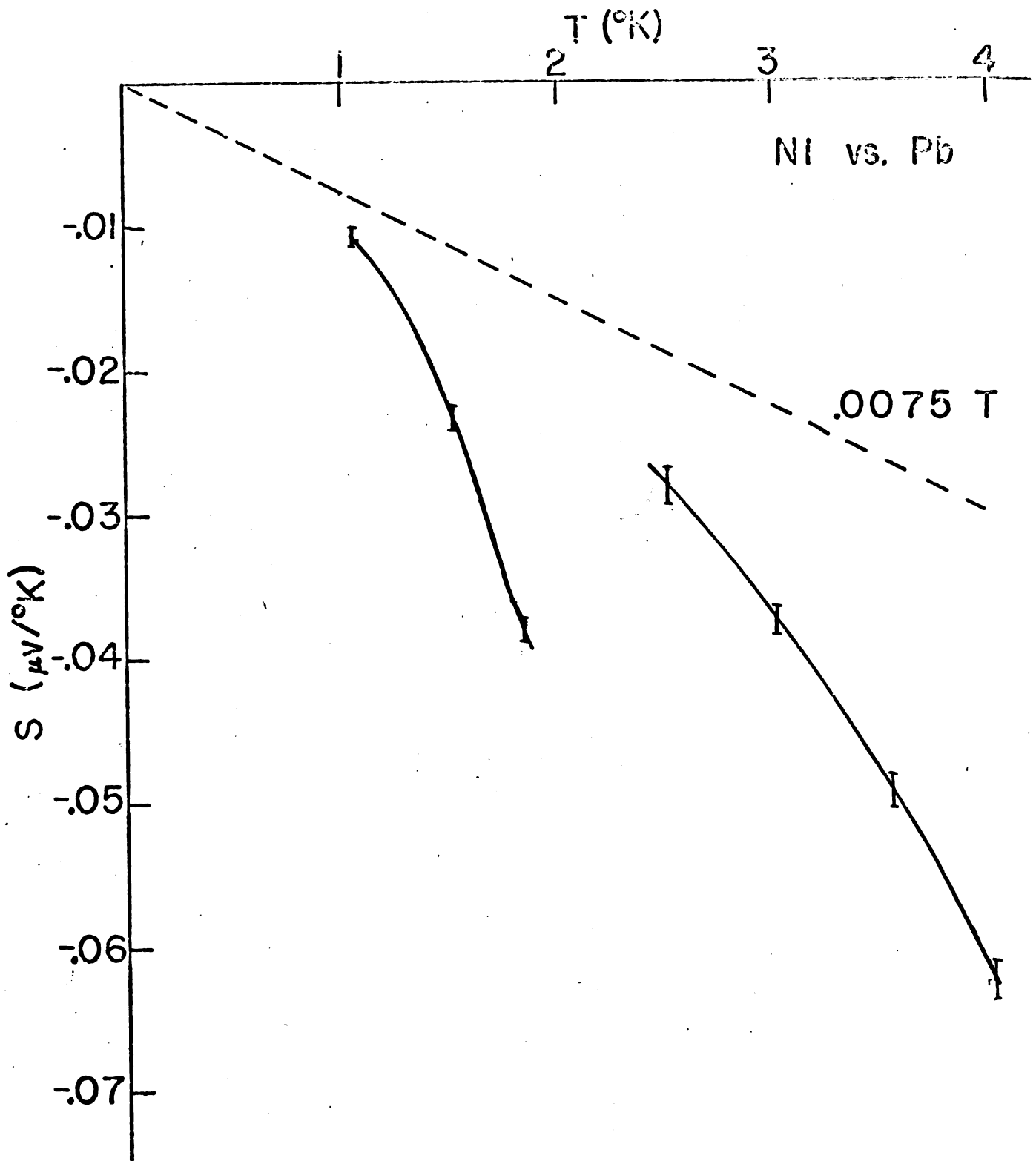


Figure 51. Seebeck coefficient of Ni

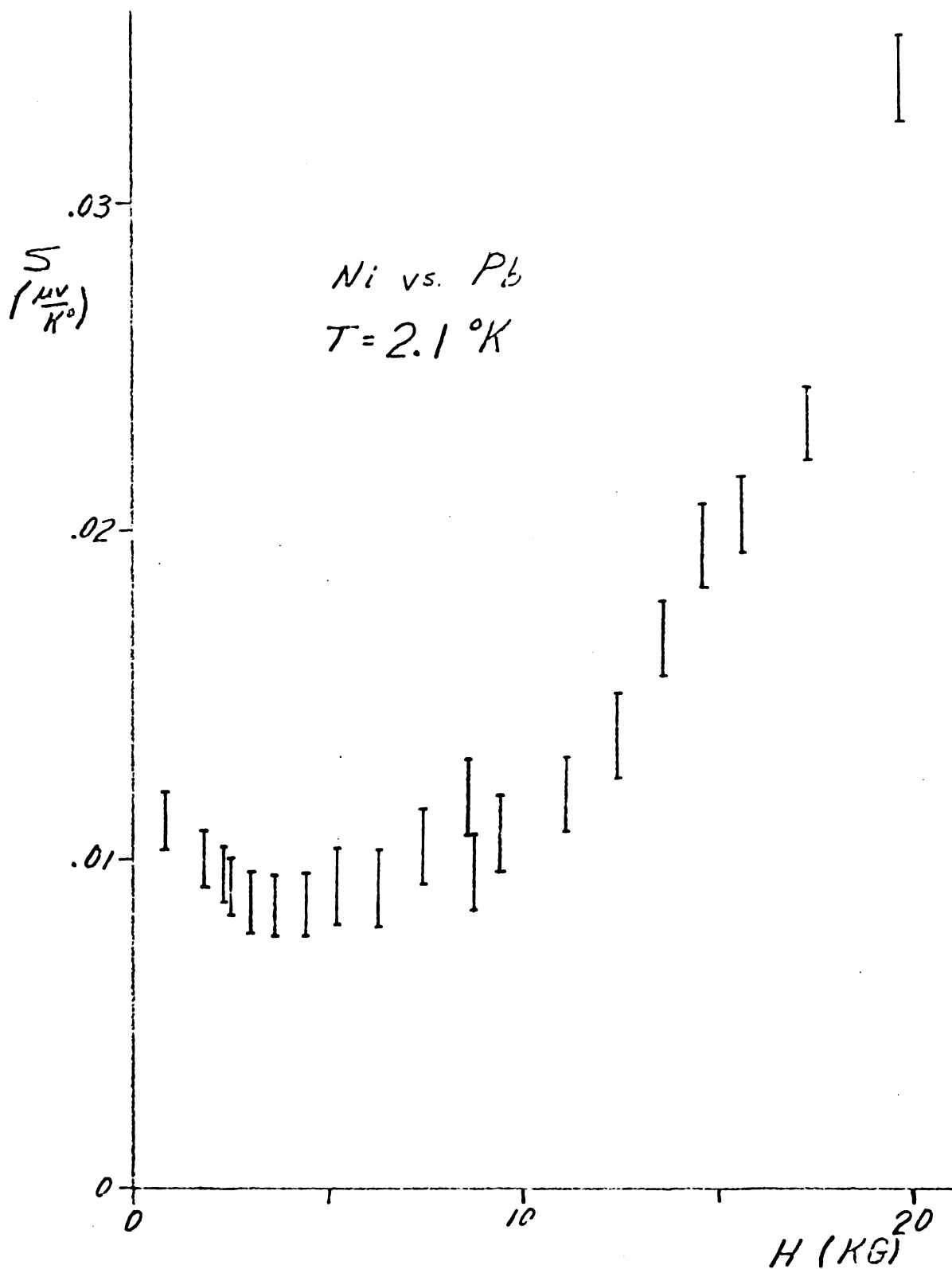


Figure 52. Ni vs. Pb in a magnetic field

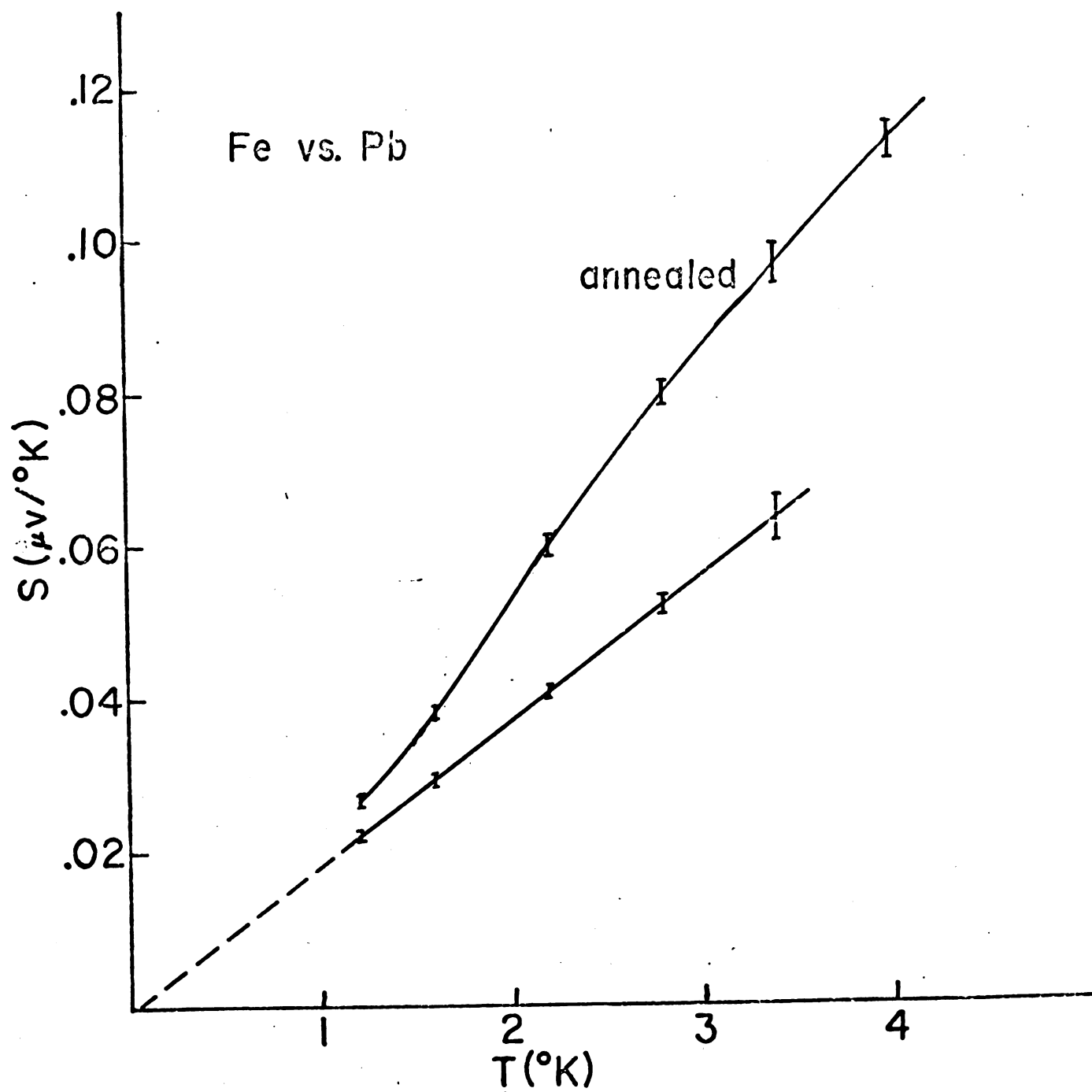


Figure 53. Seebeck coefficient
of Fe

(122)

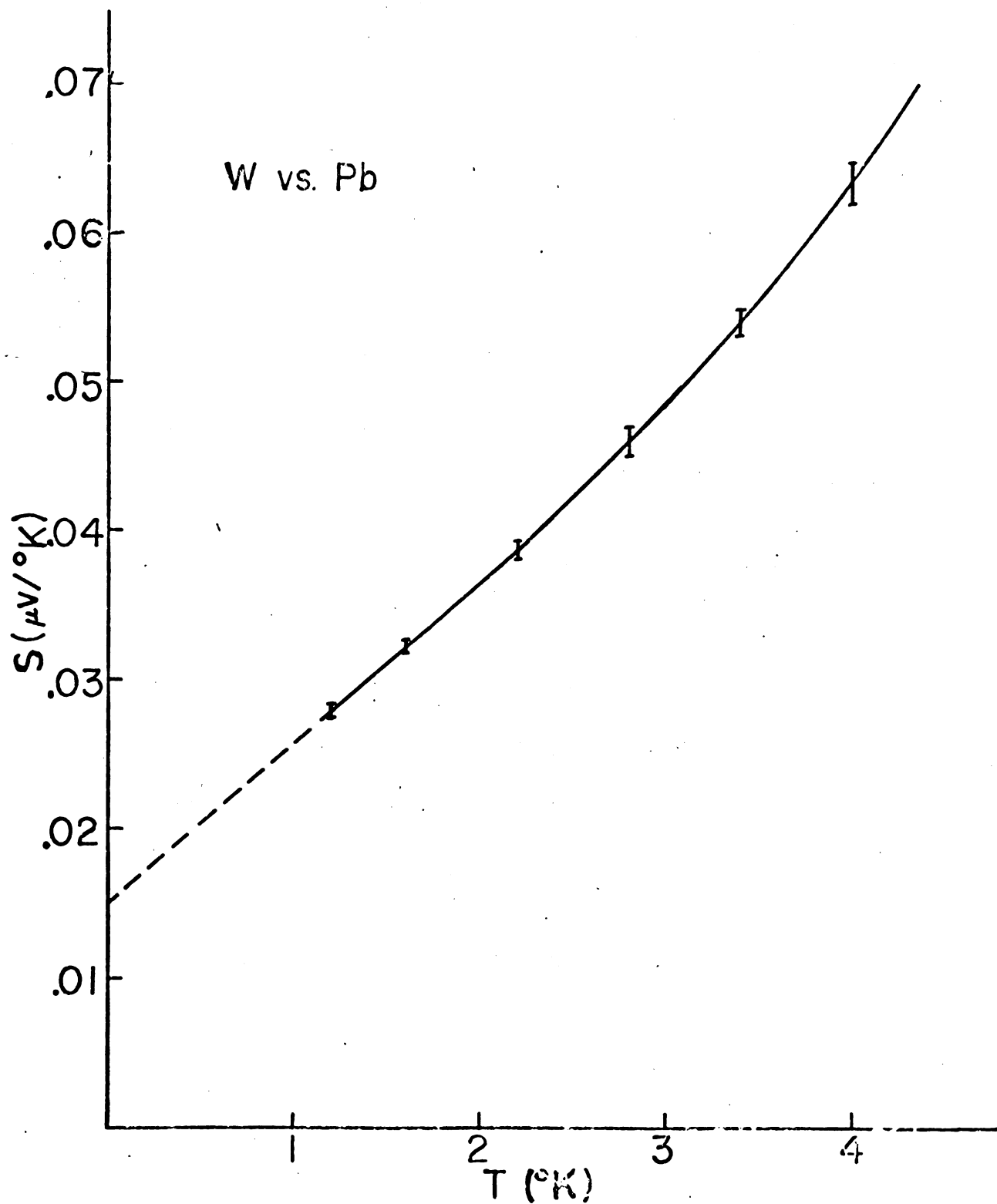


Figure 54. Seebeck coefficient of W, low temperature

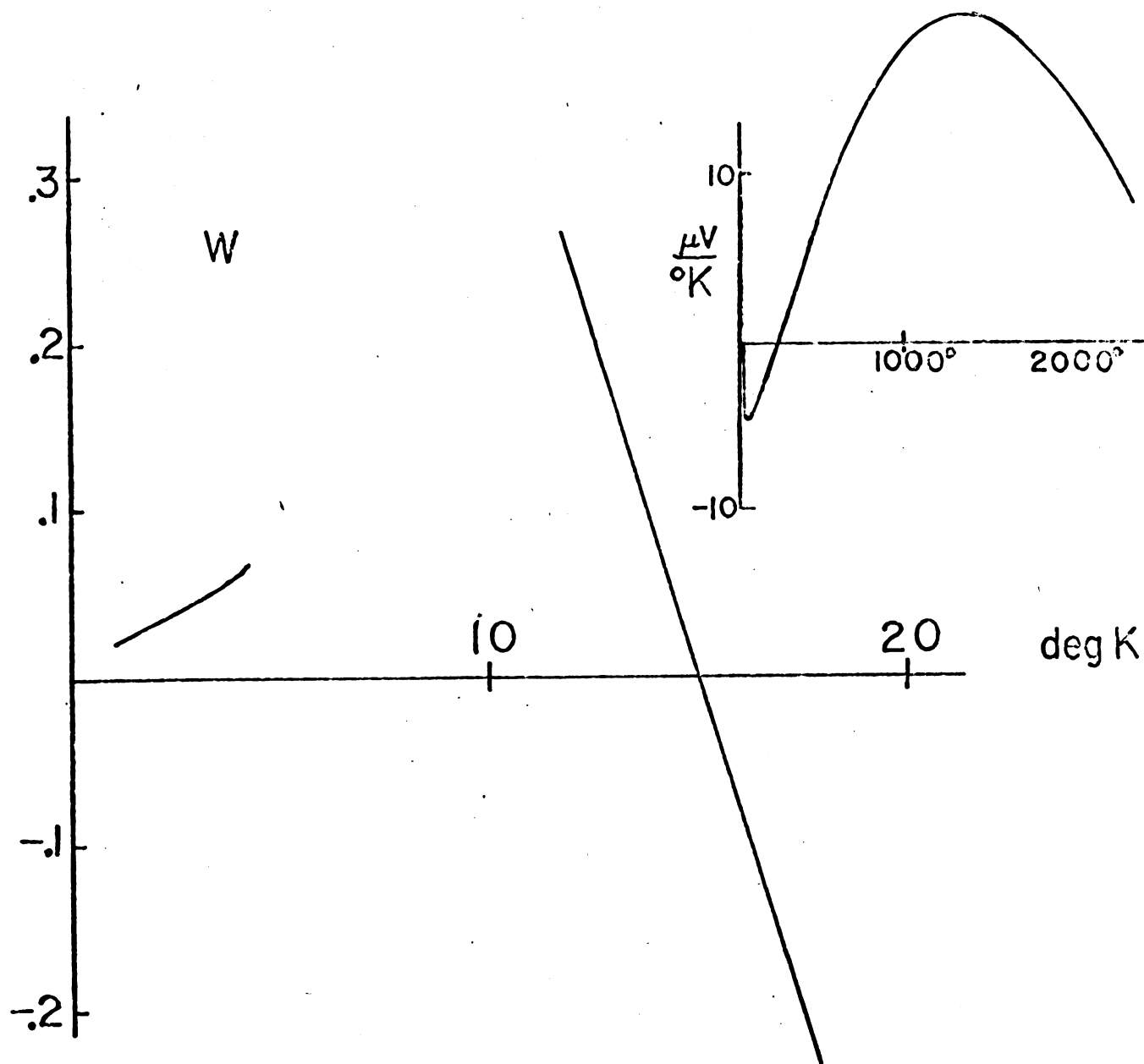


Figure 55. Seebeck coefficient
of W, intermediate temperature

The Pb data were taken in a field of one kilogauss against a variety of reference materials. These data agree with results published by Steele.⁵²

The Peltier coefficient was measured in two samples of nickel. The results for both samples can be fit by a sum of two terms,

$$-S = (.0075 \text{ } \mu\text{V/K}^0)T + \alpha T^3 \quad . \quad (\text{A-3})$$

This is just the form one might expect if diffusion and phonon drag contribute. The fact that the more strongly annealed sample shows a larger T^3 term is consistent with this interpretation. Greig and Harrison⁵³ have reported measurements which fall between the two curves in figure 51.

One set of measurements was made in a magnetic field; the results are shown in figure 52. We find a relatively large change in the thermoelectric power at the highest fields.

Figure 53 shows the results in iron. The cold worked sample displays a Seebeck coefficient which is strictly proportional to the temperature as would be predicted by equation A-2, while the annealed sample shows significant deviations at the higher temperatures. It has been suggested that this type of behavior may be related to magnon drag.⁵¹

The tungsten data show two interesting features, the linear temperature behavior which does not extrapolate to zero at zero degrees Kelvin and the positive curvature at higher temperatures. The former is difficult to understand; the Seebeck effect must eventually go to zero.

Schroeder and Davidson⁵⁴ have measured the Seebeck coefficient of tungsten down to 13°K and these results are shown in figure 55. It would appear that there is a peak near 10°K . Although this may be interpreted as a phonon drag effect it has been suggested by Colquitt and Fankhauser⁵⁵ that such behavior in the transition metals may be due to electron-electron scattering.

Appendix III

Thompson Heat Correction

Consider the situation shown in figure 56. We wish to calculate the effect that the Thompson heat has on the junction temperature T_1 . This requires a knowledge of the temperature distribution along the samples.

We define the quantity

$$k(x, T) = K_1(T)A(x) \quad (A-4)$$

where K is the thermal conductivity and A the cross sectional area of the samples. In the absence of any thermal conduction other than that along the samples, it is easily shown that

$$k_1 \frac{d^2 T}{dx^2} + \left(\frac{dT}{dx} \right) \left(\frac{dk_1}{dx} \right) = - \frac{dq}{dx} \quad (A-5)$$

The heat input per unit length dq/dx includes terms due to Joule, Thompson, and Peltier effects;

$$\begin{aligned} f(x, T) = & \frac{\rho_1(T)}{A_1(x)} I^2 + \left[\frac{d\pi}{dT} - \frac{\pi}{T} \right] \frac{dT}{dx} I \\ & + \delta(x) (\pi_1(T_1) - \pi_2(T_1)) I \\ & + \delta(x) R_0 I^2 \end{aligned} \quad (A-6)$$

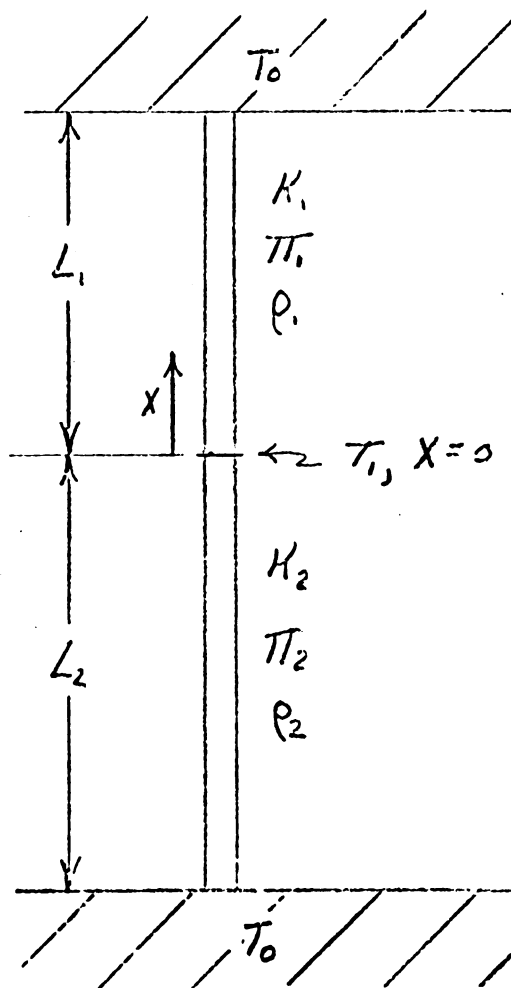


Figure 56. Thompson heat correction

where R_0 is the junction resistance. In order to represent the true situation somewhat more accurately we might make provision for a heat loss $-k_0(T_1)\delta(x)$ and a heater input $ri^2\delta(x)$ at the junction.

We now need only solve these equations to obtain a Thompson heat correction to T_1 . Under the assumptions that material 2 is a superconductor and that material 1 is in the residual resistivity region and that the cross sectional area of 1 is uniform it can be shown that the correction to T_1 due to the Thompson effect is approximately given by

$$(\delta T_1)_{th} = \frac{1}{2} \int_{T_0}^{T_1} \frac{1}{[TP''(T)]^2} \left\{ \int_{T_0}^T g(T) P'''(T) T dT \right\} dT \quad (A-7)$$

where

$$P'' = \frac{dT}{dx} \quad (A-8)$$

$$g = - \frac{I}{k_0} \left[\frac{d\pi_1}{dT} - \frac{\pi_1}{T} \right] \quad (A-9)$$

$$k_0 = k_1/T = \text{const.} \quad (A-10)$$

The complete solution of this equation is extremely tedious and cannot be given here. One must solve for P through equation A-6 and the boundary conditions

$$T(L_1) = T_0 = T(-L_2) \quad (A-12)$$

(129)

$$\begin{aligned} (k_1 \frac{dT}{dx})_{x \rightarrow 0^+} - (k_2 \frac{dT}{dx})_{x \rightarrow 0^-} = \Pi I(T_1) + R_o I^2 \\ + r i^2 - \kappa(T_1) \end{aligned} \quad (A-13)$$

$$\lim_{x \rightarrow 0^+} T = \lim_{x \rightarrow 0^-} T \quad (A-14)$$

The exact form of P'' is strongly dependent upon such unknown factors as the junction resistance and exchange gas conduction, and an exact solution is of doubtful value. In the case that both of these effects are negligible, we can approximate P'' by the easily integrable form

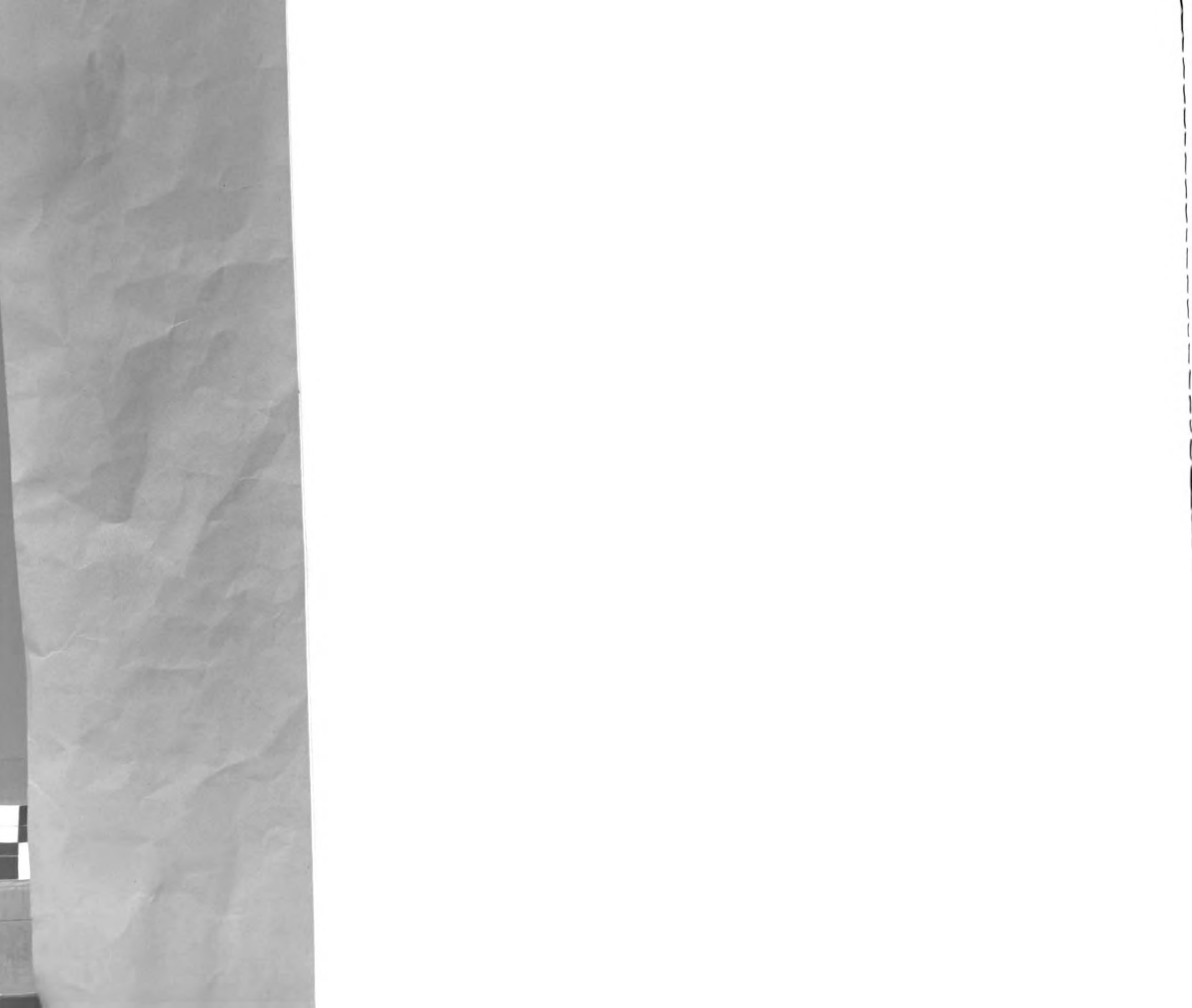
$$P'' = \text{const} \times \frac{(T - T_1)^{1/2}}{T} \quad (A-15)$$

If we further approximate $\Pi(T)$ by a straight line between T_o and T_1 , we find that the apparent reversible heat at the junction corresponds to the Peltier coefficient at a temperature given by

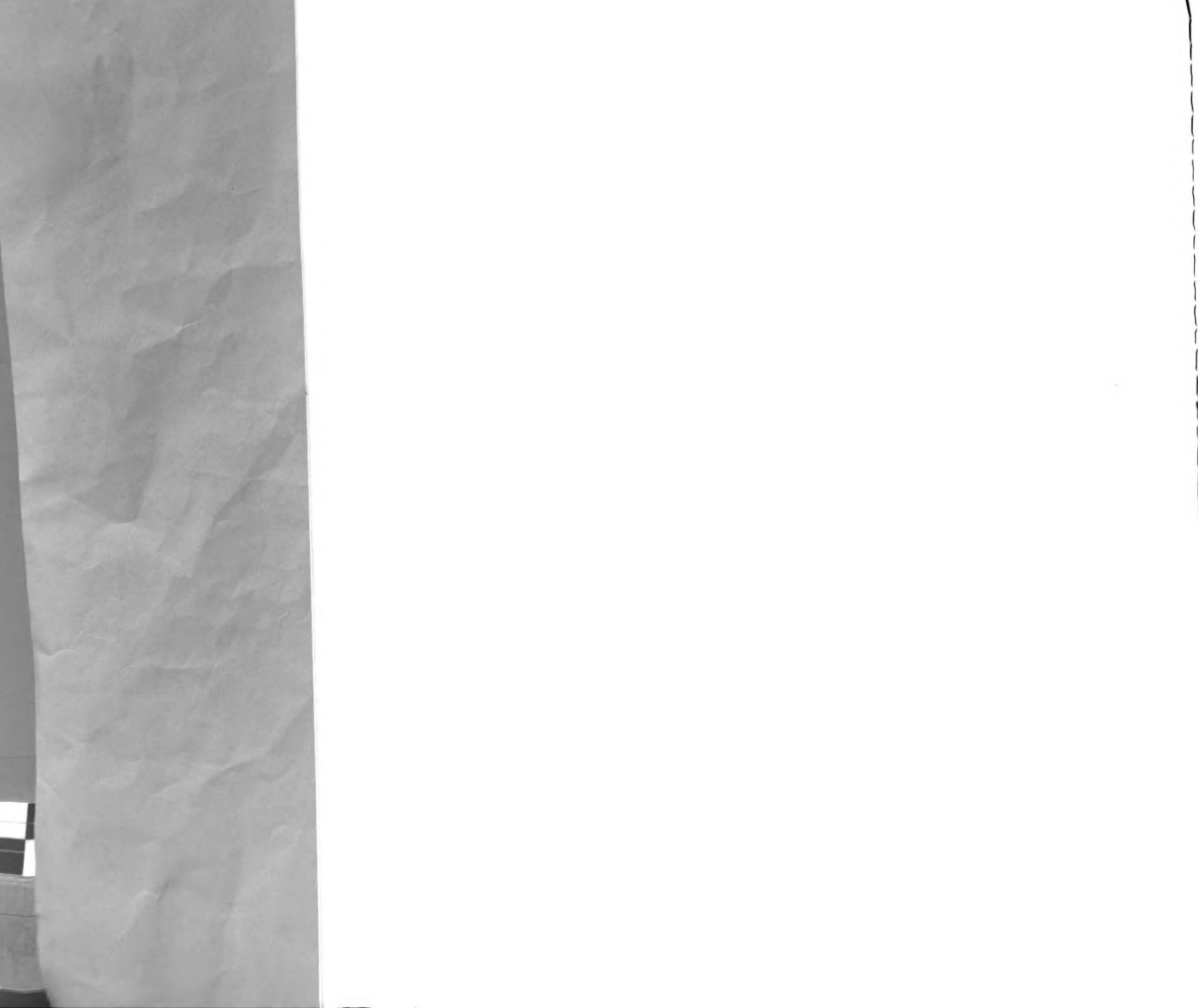
$$T_\Pi = T_1 - (T_1 - T_o) \left(1 - \frac{2}{3} \frac{T_o}{T_1}\right) \quad (A-16)$$

$$\text{if} \quad (T_1 - T_o) \ll T \quad (A-17)$$

Equation A-16 defines a temperature intermediate between T_1 and T_o . One can pick forms for P which include junction resistance and junction to bath heat exchange but it is



generally found that, if inequality A-17 is followed, the Peltier coefficient measured corresponds to a temperature between T_0 and T_1 .



Appendix IV

Thermometer Linearity

The linearity of the thermometer system depends upon the linearity of the bridge as well as that of the thermometer itself. The output from a Wheatstone bridge (see figure 57) is

$$v = \frac{VR_3}{(R_3 + R_4)} \frac{\delta}{R_3 + R_4} \quad (A-18)$$

if R_1 to R_4 are such that the bridge is in balance when $\delta=0$.

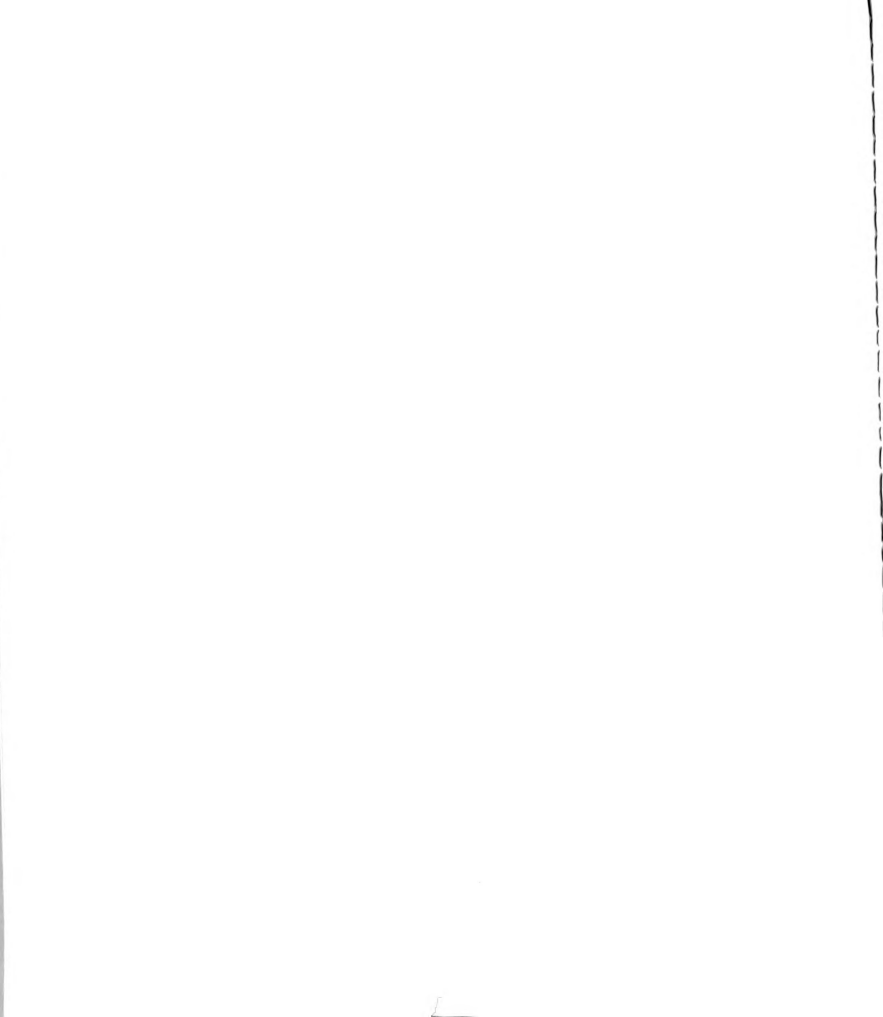
A typical plot of R vs. T for carbon resistors is shown in figure 58. This can be fit rather well by

$$R = R_0 e^{-\alpha/T} \quad (A-19)$$

Typically, α is a few degrees Kelvin in the Ohmite 1/8 ω , 33 Ω resistors used in this work. A change in temperature from T to $T + \delta T$ results in a resistance change of

$$\delta R = R_0 e^{-\alpha/T} \left\{ \frac{\alpha \delta T}{T^2} \left[1 + \delta T \left(\frac{\alpha}{T^2} - \frac{1}{T} \right) + \dots \right] \right\} \quad (A-20)$$

From equation A-20 we see that for bridge linearity we must require that



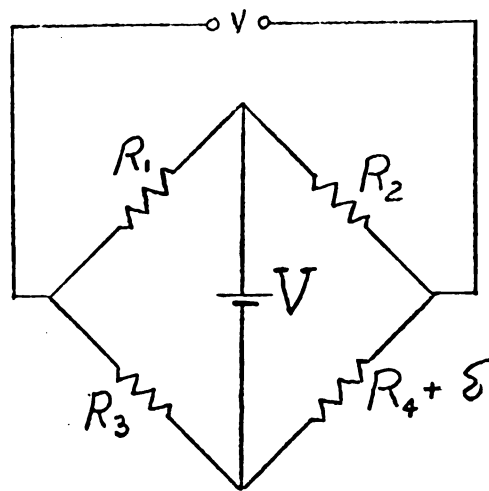


Figure 57. Wheatstone bridge



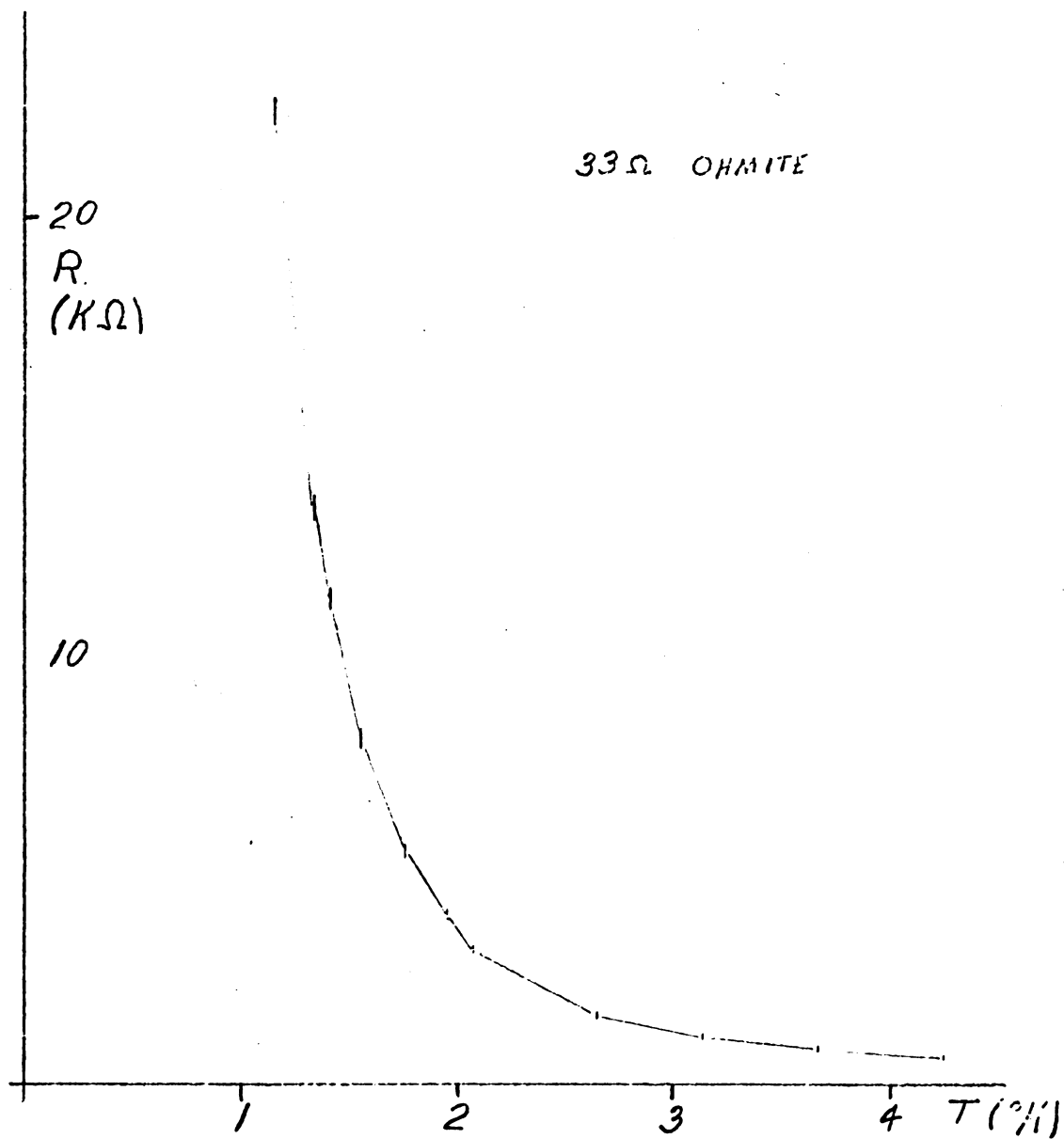
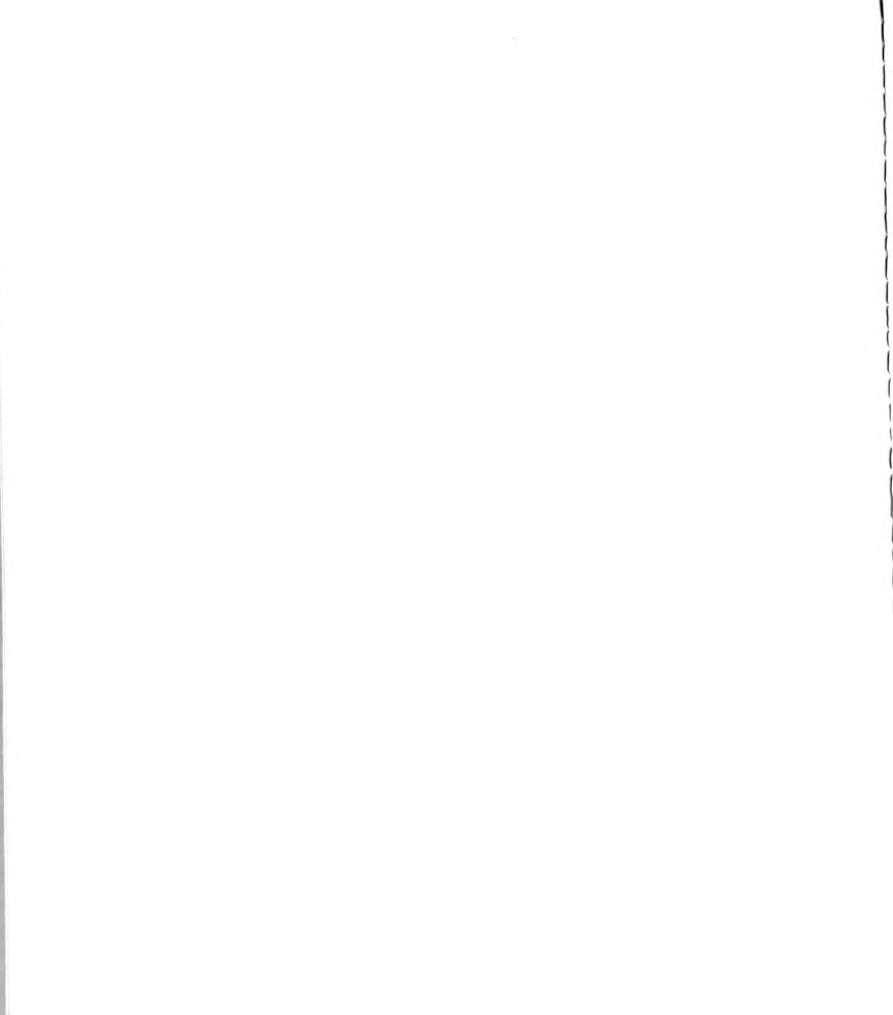


Figure 58. Low temperature resistance of a carbon resistor



(134)

$$\delta T \left(\frac{\alpha}{T^2} - \frac{1}{T} \right) \ll 1, \quad (\text{A-21})$$

or in the liquid helium range, where α/T is of order unity,

$$\frac{\delta T}{T} \ll 1. \quad (\text{A-22})$$

Assuming that inequality A-21 is obeyed we can substitute δR from the first term of equation A-20 into A18,

$$v = \frac{VR_3}{R_3 + R_4} \sum_n \left(\frac{\alpha \delta T}{2T^2} \right)^n \quad (\text{A-23})$$

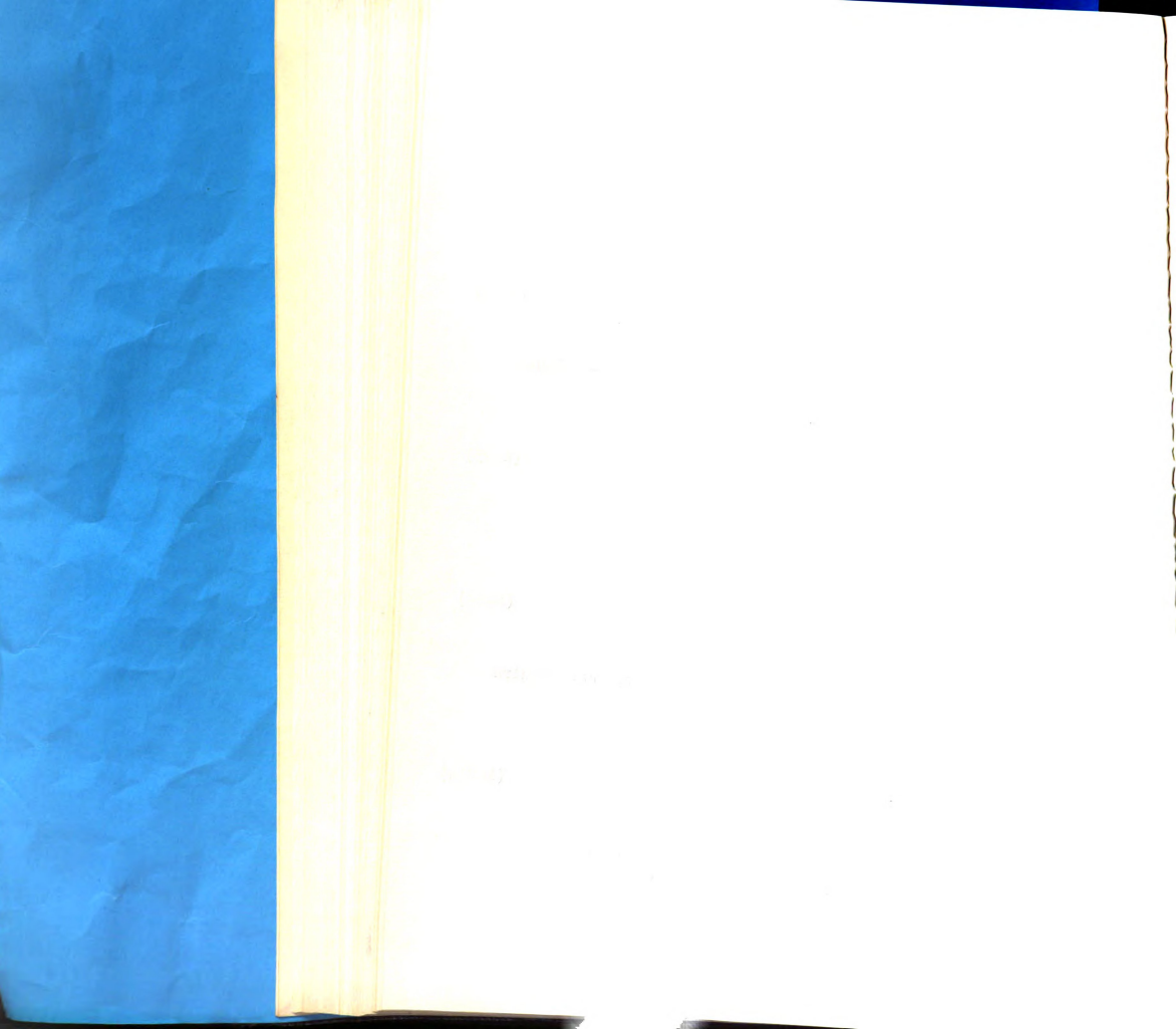
in which we have assumed that

$$R_3 \approx R_4 = R_0 e^{-\alpha/T}. \quad (\text{A-24})$$

For linearity of v vs. δT in equation A-23 we must require that

$$\frac{\alpha \delta T}{2T^2} \ll 1. \quad (\text{A-24a})$$

We must take the more restrictive of the two conditions, inequality A-22, as the basic restriction.

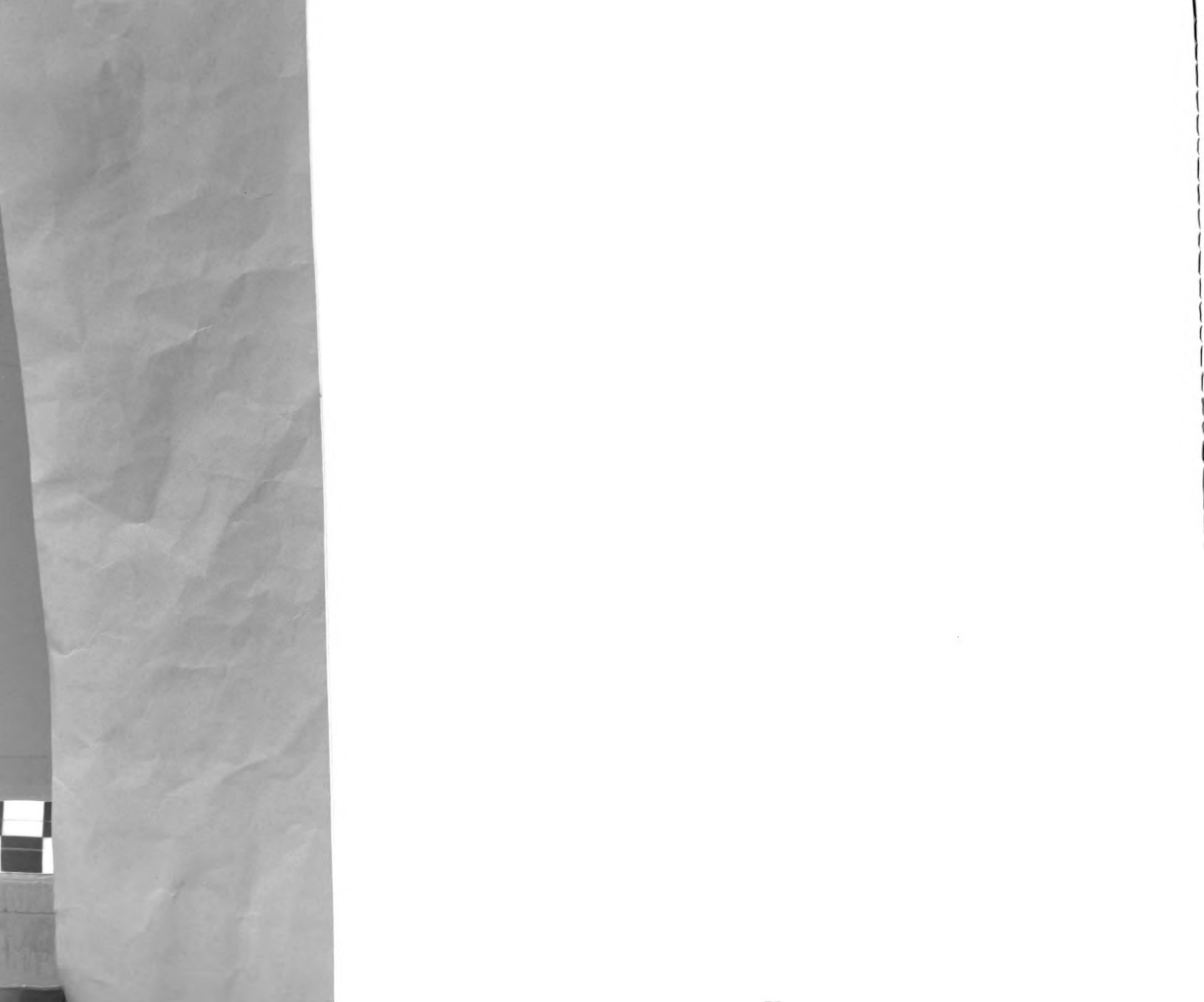


Appendix V

Manganin Resistance

The resistance of a 56 Ω coil of manganin was measured at two temperatures and in fields to 20 kilogauss. The results are presented in figure 59 in which the vertical axis has been normalized by dividing the measured resistance by the room temperature resistance. For all temperatures and fields in this range,

$$\frac{R(T,H)}{R(300^{\circ},0)} = .877 \pm .5 \text{ per cent.} \quad (\text{A-25})$$



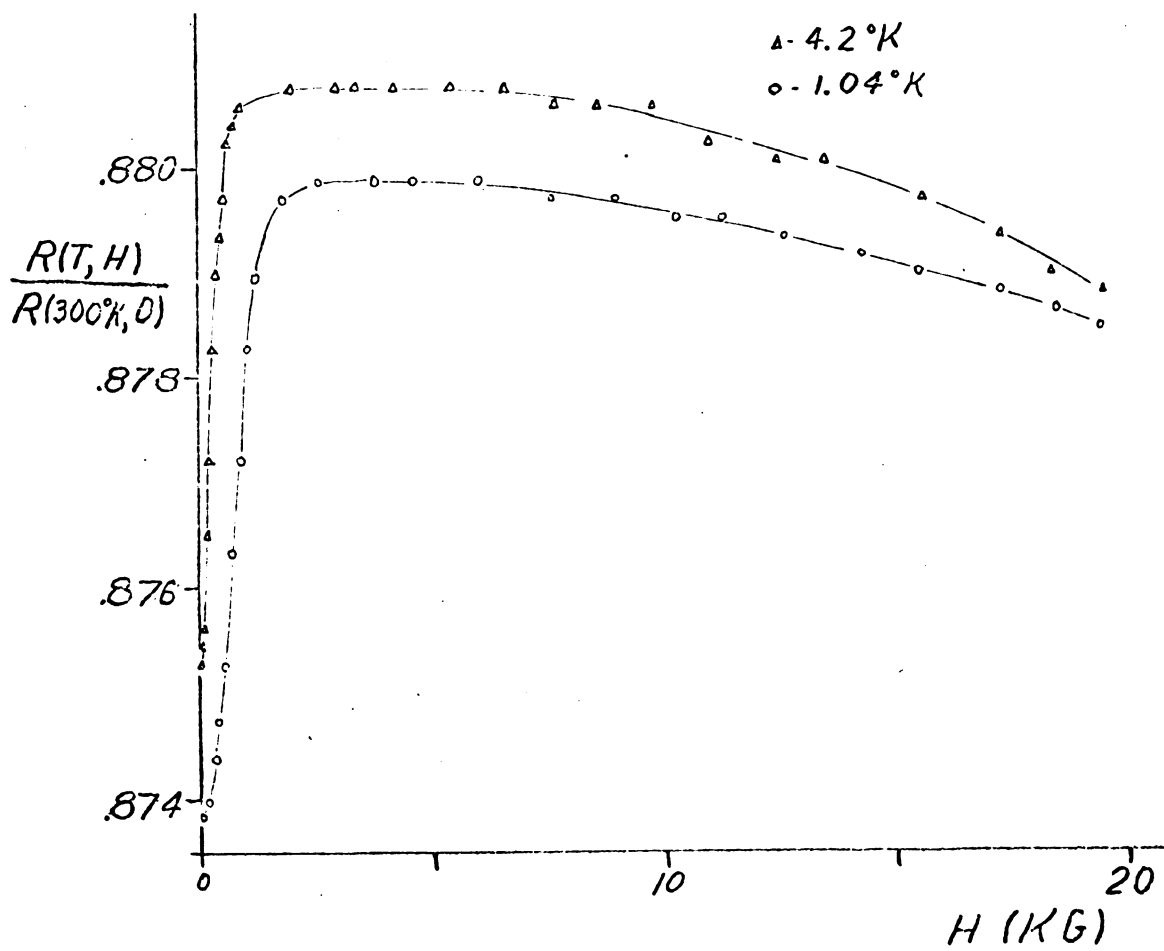


Figure 59. Magnetoresistance of Manganin



Appendix VI

Kelvin-Onsager Relations in a Magnetic Field

In the presence of a magnetic field the application of the Onsager reciprocal relations results in

$$\Pi(H) = TS(-H) \quad . \quad (A-26)$$



Appendix VII

Effects of Sample Misalignment

The theoretical discussion of section IV assumed that the sample current was transverse to the magnetic field direction. In the measurements this was true within only 5° and we must establish that misalignment of this magnitude does not significantly change the theoretical treatment. The misalignment affects the theory through changes in the magnetoresistance, the Hall coefficient and the factors L_{15} and L_{25} . Upon a rotation of the current direction to an angle θ from the plane perpendicular to H (see figure 60) the magnetoresistance changes by the factor $\cos^2 \theta$ while the Hall coefficient changes by the factor $\cos \theta$. For a 5° misalignment both of these factors are less than 1 per cent, a negligible effect. The effect of the misalignment on the factors L_{15} and L_{25} is rather difficult to assess. Although it appears doubtful that these would be significantly affected, we must consider this as a basic uncertainty in the interpretation of the results. This type of misalignment may have caused the lack of symmetry mentioned in connection with figure 32.

The possible misalignment of the crystal axes with respect to the magnet field direction is a more serious problem. The ability to rotate the magnet allows field alignment to within about 0.5° in the X-Y plane (see figure 60). However, the misalignment perpendicular to this plane may be as large as 5° .

If the amplitude of the oscillations is found to be insensitive to a rotation of the magnetic field it is reasonable to assume that a further rotation by a small angle ϕ (figure 60) to the desired crystallographic direction would

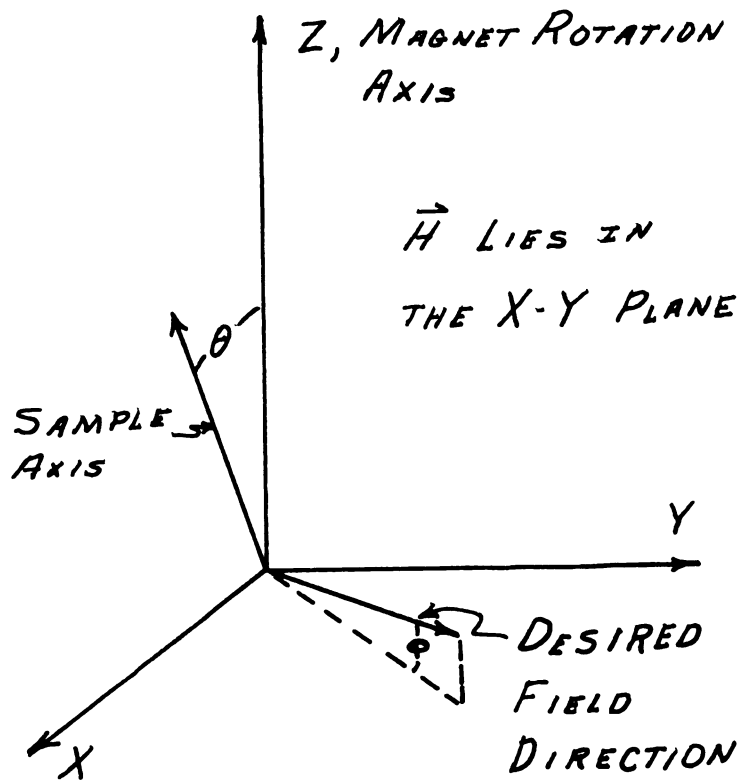
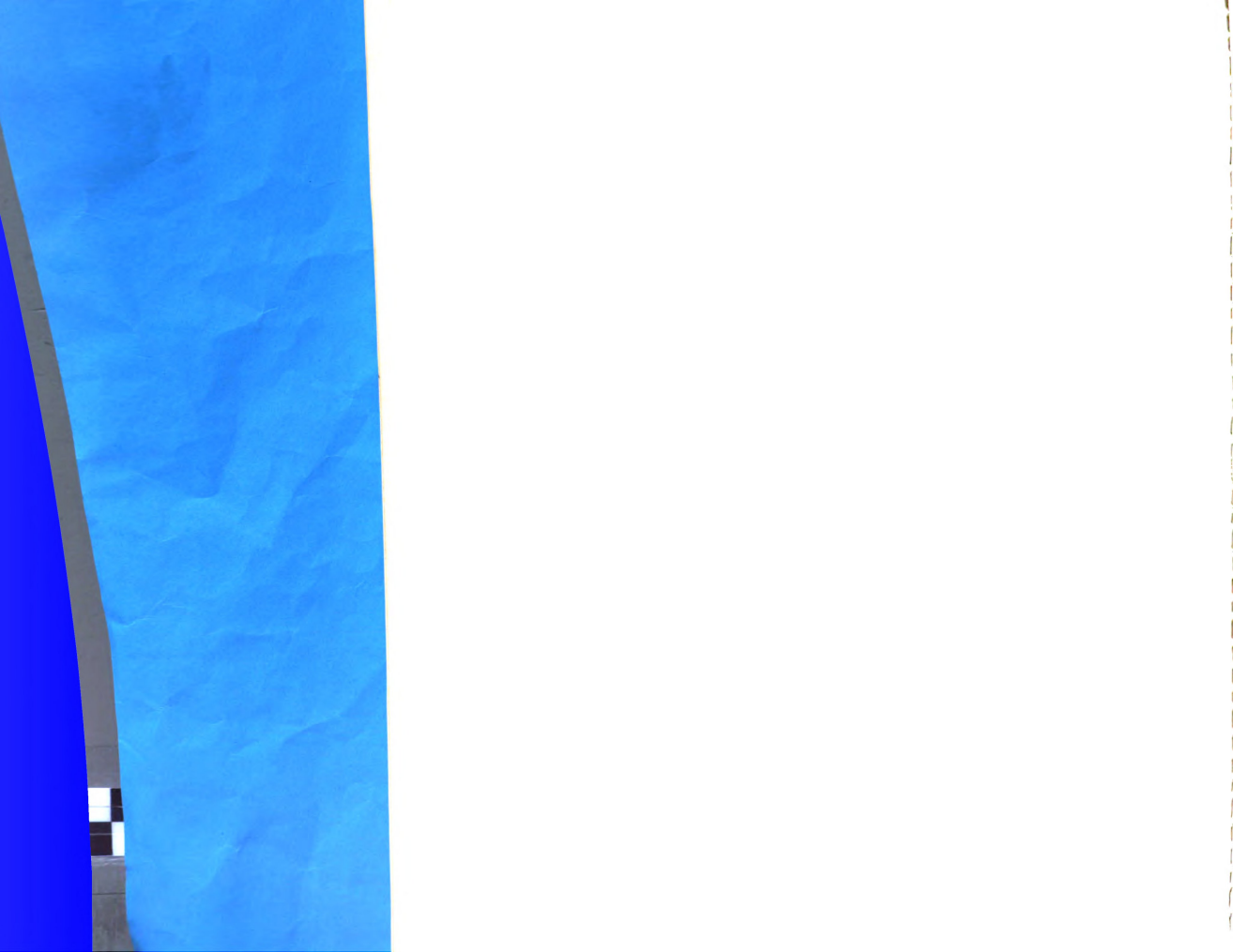
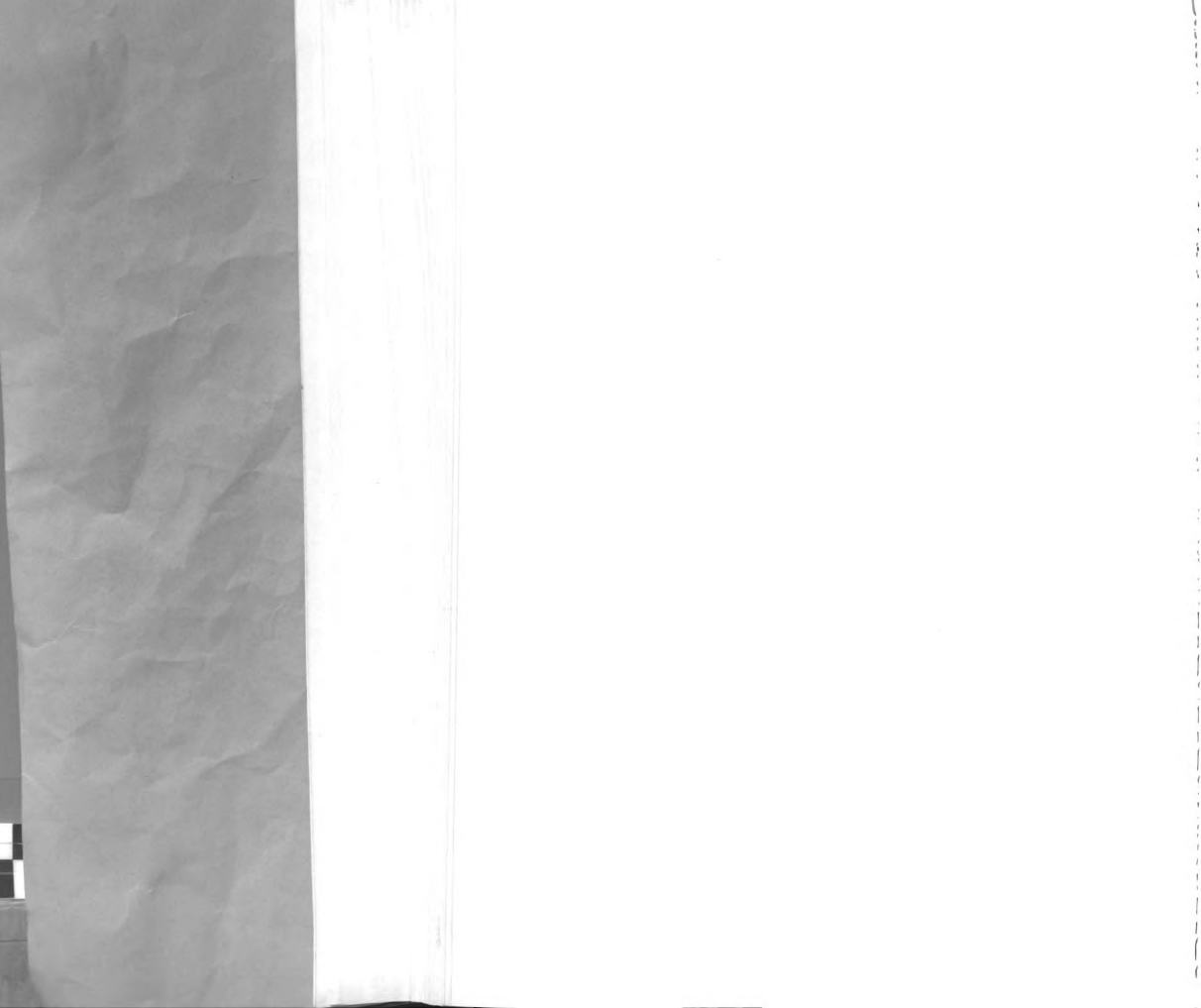
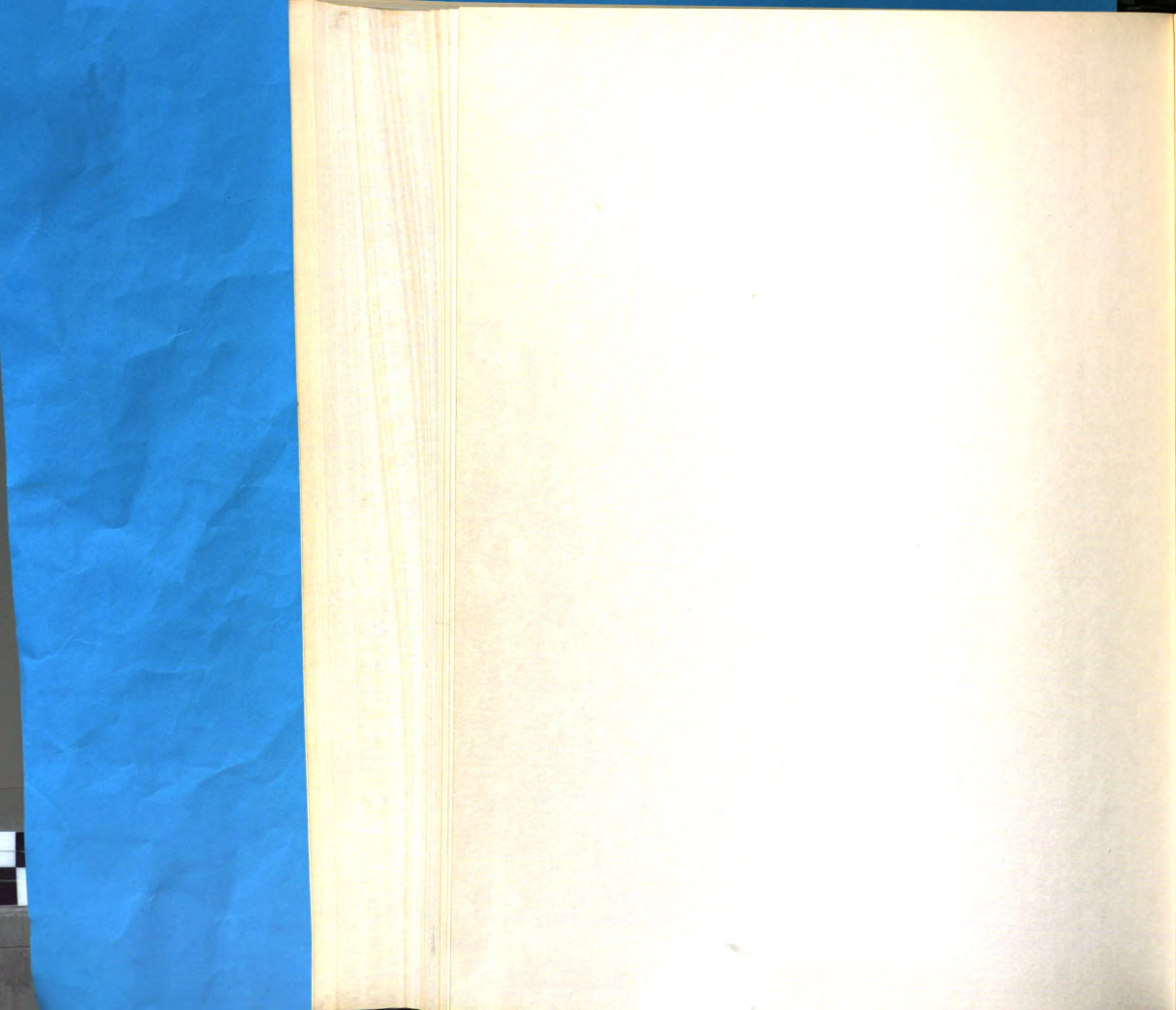


Figure 60. Sample alignment



not significantly affect the measurements. This argument cannot be used on the α oscillations in zinc, which are strongly angle dependent, and is of doubtful validity in the case of the γ oscillations which show a relatively strong angle dependence. Possible misalignment of this type introduces an uncertainty (less than a factor of 2) into the absolute amplitude measurements while the temperature and field dependences are essentially unaffected.







MICHIGAN STATE UNIVERSITY LIBRARIES



3 1293 03178 1176